2016

Excitonic Processes, Energy Transport, and Excited States in Organic Materials

Vincent Sean Zoutenbier
Lehigh University

Recommended Citation

Zoutenbier, Vincent Sean, "Excitonic Processes, Energy Transport, and Excited States in Organic Materials" (2016). *Theses and Dissertations*. 2916.
http://preserve.lehigh.edu/etd/2916

Excitonic Processes, Energy Transport, and Excited States in Organic Materials

by

Vincent Zoutenbier

A Dissertation
Presented to the Graduate Committee
of Lehigh University
in Candidacy for the Degree of
Doctor of Philosophy
in
Department of Physics

Lehigh University
September 2016

Approved and recommended for acceptance as a dissertation in partial fulfillment of the requirements for the degree of Doctor of Philosophy.

Vincent Zoutenbier

Excitonic Processes, Energy Transport, and Excited States in Organic Materials

Date

Ivan Biaggio, Dissertation Director, Chair

Accepted Date

Committee Members

Volkmar Dierolf

John Huennekens

Michael Stavola

Nicholas Strandwitz

Never mistake experience for intuition.

Contents

List of Figures

Abstract

This dissertation has roots in the distinctly human endeavor to harness energy. We study singlet exciton fission, which has the remarkable ability to double the number of energy carriers (excitons) through singlet fission, and its reverse process triplet fusion, which can combine triplet excitons. Understanding the fundamental mechanisms that enable singlet fission may allow for it to be engineered for use with other materials for solar cell applications.

We experimentally investigate the creation of singlet and triplet excitons in rubrene single crystals, how one species can convert into the other by excitonic fission and fusion processes, and how triplet excitons can travel comparatively long distances.

Using steady-state excitation, we determine that the efficiency of singlet exciton fission and triplet fusion are both large, likely exceeding 90%, and are only weakly magnetic field dependent in pristine rubrene single crystals. We find a decrease in fission efficiency by 20% when applying a magnetic field of 1 T, which is visible as an increase of 20% of the photoluminescence quantum yield in the limit of low excitation density; Further, we also report an increase in quantum yield of only about 5% in the limit of high excitation densities, where triplet fusion dominates the emitted PL. These observations are consistent with a magnetic field-induced reduction of both singlet fission efficiency and triplet fusion efficiency.

We also investigate the PL quantum yield as a function of temperature and find an increase in PL quantum yield by about a factor of almost an order of magnitude between $295\,\mathrm{K}$ and temperatures of the order of $120-150\,\mathrm{K}$; which is likely due to a temperature dependence of the fission processes through an activation energy

barrier. We find no changes to the PL spectrum's intensity distribution in pristine rubrene crystals when changing either the applied magnetic field strength, or the sample's temperature.

A high fission and fusion efficiency in rubrene single crystals means that it is possible to determine the triplet exciton diffusion length by directly imaging the photoluminescence emitted by a diffusing triplet population. We study how exciton diffusion depends on temperature and magnetic field and find that the diffusion length remains large at all investigated temperatures, keeping a value of $4.0 \pm 0.5\,\mu$m with no observable temperature variation down to a temperature on the order of 225 K. For the magnetic field dependence of diffusion, we find that an applied magnetic field of 1 T increases the diffusion length from 4.0 microns at 0 T field to $5.4 \pm 0.4\,\mu$m.

Finally, we investigate the singlet fission process by an extensive study of PL dynamics after pulsed excitation. We determine the PL time dynamics as a function of excitation density and observe the appearance of a component of the photoluminescence that follows an exponential decay with a decay time constant of 4.3 ± 0.5 ns. By studying how this component varies with excitation power and the level of impurities in rubrene crystals, we show that this decay is likely related to the presence of a quantum superposition of singlet state and triplet-pair state which acts as the intermediate state of singlet fission. We then tentatively assign the 4.3 ns decay to the lifetime of this intermediate state, which is essentially given by the triplet component's dissociation time into two independent triplet excitons. We also show that the feature associated with this intermediate state is the only feature of the photoluminescence decay between 0.1 and 100 ns that shows any dependence on an applied magnetic field. This supports the interpretation that the 4 ns transient is related to a quantum superposition of singlet and triplet-pair states.

Chapter 1

Introduction

The physics of energy collection is a uniquely human endeavor. In fact, early humans began cooking their food as a way to increase their food's energy density, which is believed to have been a driving force for the development of a larger brain [1]. Since then, humans have come to understand how energy can be converted and used to do useful work; the collection, conversion, and transport of energy are fundamental to powering modern day society. This dissertation has its roots in fundamental energy science and contributes to an understanding of how energy is converted between molecular excited states in organic molecular crystals.

Current silicon-based solar cells rely on the electronic band gap structure of semiconductor materials to convert and harvest electrical energy. Substantial research is being put into reengineering photovoltaics cells to use organic molecules for possible improvements in fabrication techniques, flexibility, and cost-effective implementation compared to inorganic semiconductors.

Some organic molecules can be arranged in a very ordered way, creating a molecular crystal; held together by weakly attractive van der Waals forces between neighboring molecules. While the constituent molecules of molecular crystals retain many of their individual properties, such as those related to the absorption and emission of light, molecular crystals can also exhibit signatures of intermolecular interactions from their crystal structure, which can facilitate new phenomena.

One such intermolecular phenomenon, singlet exciton fission, splits the energy of a singlet exciton over two triplet excitons, a process which is under active theoretical and experimental research [2–4]. This dissertation is a case-study on rubrene single crystals, where the triplet exciton has a long lifetime that allows for diffusion through the crystal to dissociation sites which collect the exciton's electron and hole to produce a voltage. Harvesting triplet excitons in this system would double the number of carriers per excitation photon, and halve the energy of each carrier. Using this process for UV light in a tandem solar cell could allow for the extraction of energy from light that would otherwise be wasted as heat [5], thereby introducing a mechanism that could be used to overcome the Shockley-Queisser limit of photovoltaic cell efficiency [6, 7]

The processes that facilitate singlet fission and triplet fusion are not well understood, with conflicting data and interpretations in the literature. We present new research that helps to reconcile some literature sources and clarify the physics at work in rubrene.

Before we present this dissertation's contributions, we provide background material on excitons, their transitions, and rubrene in chapter two. We then investigate excitons using many different types of experiments that are either steady-state or time-dynamics measurements.

In chapter three, we describe experiments in which we collect photoluminescence (PL) from rubrene single crystals using a continuous-wave laser while changing sample temperature, excitation power, and applying a magnetic field. These measurements are either spatially resolved, spectrally-resolved, or spectrally-integrated to study exciton diffusion, excitation and relaxation, or exciton fission (respectively).

In contrast to the steady-state measurements, the experiments described in chapter four use a pulsed laser to study time dynamics of photoluminescence from rubrene. Measurements of the time dynamics of PL while changing excitation power, an applied magnetic field, and spectral filters provide information about the relative populations of excitons which can help complete our model of singlet fission and triplet fusion. In addition to experimental work, we also simulate the time dynamics of PL from rubrene using a 3-state model of exciton fission.

Appendix A contains a derivation of an equation discussed in the main text, and appendix B is an extension of our model presented in chapter four to the spatial diffusion of excitons.

Chapter 2

Background Information

This chapter introduces the physics needed for the fundamental-science research presented later in this dissertation. We first present general topics in excitons, singlet fission, and triplet fusion, then move on to a description of the archetype material used for this dissertation, rubrene, with a brief literature review presenting the state of the art.

2.1 Excitons

The Pauli exclusion principle requires that the ground state of a molecule can have no more than two electrons in the highest occupied molecular orbital. When a ground state molecule with two electrons in the highest occupied molecular orbital absorbs a photon, an electron is promoted to an excited state. This transition leaves a positively-charged ‘hole’ in the highest occupied molecular orbital for the electron to interact by the Coulomb force. In molecular crystals consisting of ordered assemblies of such molecules, the wavefunctions of the electron and hole together as the excited state of the molecule can be considered a quasiparticle called an exciton [8].

The electron band structure of most inorganic semiconductors hosts delocalized excitons that are loosely bound and can be broken by thermal energy at room temperature [9]. However, in molecular crystals there is little overlap of electron orbital wavefunctions between molecules, which is indicative of low charge mobilities and excitons with large binding energies. This large binding energy leads to excitons that are stable at room temperature with high electron-hole dissociation energies. [10].

2.1.1 Types of Excitons

In inorganic crystals, excitons can be of Frenkel or Wannier-Mott type, where the electron and hole exist on either a single lattice site, or over many sites [8]. The size of an exciton depends on the electronic and geometric properties of the lattice, its composition, and bonding structure [8]. A third type of exciton found in some molecular materials, the charge-transfer exciton, has separated charge centers where the electron and hole's wavefunctions are spatially separated from each other [11].

In an individual molecule in an excited state with two valence electrons, the two highest energy electrons each have two possible spin orientations. There then are four configurations for the two electrons allowed by the Pauli exclusion principle. From these four configurations, the single antisymmetric arrangement of electrons, with no net spin, is called the singlet exciton state (S). In contrast, the three symmetric configurations, with net spin of 1, are called the triplet exciton state (T). When considering the excited states of two molecules simultaneously, it's possible to build states with net spin greater than 1 such as the quintet state with spin 2 [3, 12, 13]; however, this dissertation focuses on singlet and triplet excitons.

Photoexcitation of an electron to an electronic excited state through the dipole interaction does not change the spin of the electrons; therefore the two higher energy electrons of a freshly photoexcited molecule must be in a singlet state (since they started in the singlet ground state). The corresponding two-electron wavefunction will therefore need to be spatially symmetric with a larger probability of the two electrons being closer together, which involves a larger Coulomb interaction energy.

When the two higher energy electrons of an excited molecule are in a triplet state, they have a spatially antisymmetric two-electron wavefunction. The probability of the two electrons being close together is therefore reduced, which in turn reduces the Coulomb interaction energy and makes the binding energy of triplet excitons larger [14].

Since dipole interactions do not change the spin wavefunction of the molecule, and since triplet states have a spin of 1, the triplet state cannot radiatively decay to the ground state in the dipole approximation, or be created by photoexcitation from the ground state. The triplet state is a 'dark state', and does not couple to the singlet ground state via interaction with a photon (apart from going beyond the dipole approximation, which then leads to phosphorescence).

However, it is possible for an excited state molecule to convert between singlet and triplet states. The first possibility is that a photoexcited singlet state molecule spontaneously transforms into a triplet state via spin-orbit coupling. This is generally allowed energetically, but is a low probability event because of the weakness of the spin-orbit interaction [15]. The second possibility is what we are studying; if the triplet state energy is near half the singlet state energy, then an excited singlet-state molecule can interact with a neighboring molecule in the ground state to create a pair of triplet states which have a combined spin of zero. This is the first step in a fission process that ultimately results in two independent triplet states. Similarly, the reverse process is also possible; in materials where the energy of the triplet excitons is such that pooling of the energy of two triplet excitons can reach the energy of the singlet state, two triplets can undergo a fusion process to create a spin-zero pair of excited singlet and ground state singlet molecules.

2.1.2 Singlet Exciton Fission

Singlet excitons in some molecular crystals can divide their energy into two triplet excitons in a process called singlet fission [3, 16]. In the following section, we define the terminology we use in this dissertation to describe the states and processes of singlet fission; it is largely paralleled by the literature, but is presented for clarity. Singlet fission begins when the excited singlet state of a molecule (S_1) mixes its possible electron configurations with those available to the zero-spin ground state of a neighboring molecule (S_0). This first step is called *state mixing* and creates the intermediate exciton state. The intermediate state, M, is a quantum superposition of a singlet character state ($S_1 \oplus S_0$) and a triplet character state (${}^1(TT)$); this can be represented as $M = (S_0 \oplus S_1) \oplus {}^1(TT)$ where the two $\oplus$s represents a quantum superposition of the two states. The final step in singlet fission disentangles the triplet character state to leave two independent triplet excitons (T_1) that can independently move to other molecules. This step is well described as *intermediate state dissociation* or *triplet-pair dissociation*. The entire singlet fission process, from excited singlet state to independent triplet states, is seen in Eq. 2.1:

$$S_0 \oplus S_1 \overset{k_{-2}}{\rightharpoonup} M \overset{k_{-1}}{\rightharpoonup} T_1 + T_1. \tag{2.1}$$

where the values of k_{-2} and k_{-1} describe the rate at which the state mixing and triplet-pair dissociation steps occur. These transition rates will be used in time dynamic studies later, but will be expressed in terms of the reactant state lifetime, τ_x, to compare directly with experimental results. The two reaction rates k_{-2} and k_{-1} together determine the total singlet fission rate, which we define as the entire process from one excited singlet to two independent triplets (conventionally described using the rate constant γ'.)

Each step of singlet fission must conserve the total energy and net spin of the two-molecule system. Energy conservation requires that the initial energy of a singlet exciton (E_S) be at least twice as large as the energy of each final triplet exciton (E_T) (so that $E_S \geq 2E_T$), although this requirement loses some precision because thermal energy and phonons can assist with exciton fission [3]. Spin conservation through singlet fission requires that the two independent triplet excitons inherit spins so that their total spin remains zero. The physics of energy and spin conservation in this process can be understood with a more detailed look at the intermediate state.

The Intermediate State

The intermediate state is a superposition state of a singlet character state and triplet character state that exists over two molecular sites simultaneously. The excited molecule with a singlet exciton and a neighboring ground state molecule are together considered the singlet character of the intermediate state. At the same time,

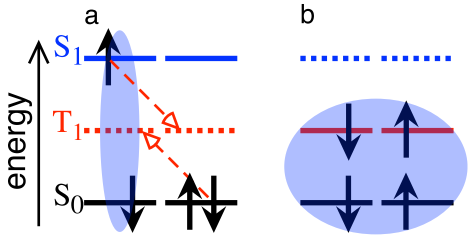

Figure 2.1: Direct mechanism for singlet fission. A photoexcited singlet state and neighboring ground-state molecule a) each have an electron simultaneously change energy levels (red dashed arrows) to create the intermediate exciton state b).

in such a way that their total spin is 0, the same two molecules each host a triplet exciton which are coherently entangled; the two triplets do not choose a spin configuration [3]. This duality of having both singlet character and a correlated triplet pair corresponds to the quantum superposition of the intermediate state. In some systems, this superposition state can acquire a coherent phase between the singlet and triplet states [2, 17–22], which leads to constructive and destructive interference which can be observed as quantum beats [2, 23, 24]. The physical mechanism responsible for the state-mixing step, which creates the intermediate state, is an area of active research [11, 24]. Physical descriptions of the state mixing process utilize either a direct or a mediated process. The direct mechanism uses internal electron rearrangement to create an intermediate state, while the mediated mechanism separates a singlet exciton's electron and hole onto neighboring molecules, creating a charge transfer exciton, before creating an intermediate state.

The direct mechanism for creating the intermediate state (also called the 'four electron model' [11] or 'direct coupling' [3]) is shown in Fig. 2.1. In this mechanism, the excited electron and the opposite-spin ground state electron of the neighboring molecule simultaneously change energy levels, (red-dashed arrows in Fig. 2.1a) directly creating the intermediate state exciton in Fig. 2.1b. A detailed review of the direct mechanism with a Hamiltonian description can be found in Ref. [3]. Because of its direct and simultaneous exchange of two electrons there is no net charge created between the two molecules involved; in contrast with the mediated mechanism.

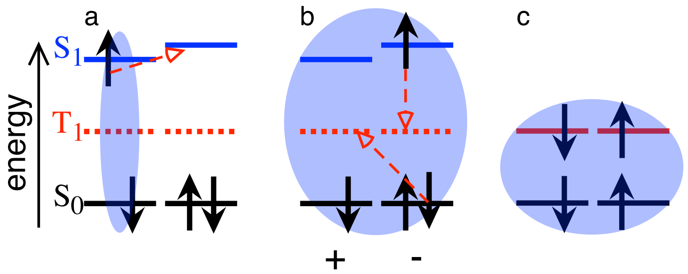

Figure 2.2: Mediated mechanism for singlet fission. A photoexcited singlet state a) moves its excited electron to the charge transfer excitonic state b) (shown with red dashed arrow on a). A two-electron transition from the CT state is seen by red arrows on b) to the intermediate state (seen in c).

The mediated mechanism for creating the intermediate state (sometimes called ‘CT’ for ‘charge transfer’ mechanism [3, 11, 17]) is shown in Fig. 2.2. The charge transfer exciton consists of a positively ionized molecule close to a negatively ionized molecule. Moving the excited singlet state’s electron from one molecule to the next requires energy because of the need to overcome Coulomb attraction. The additional electron in the negatively ionized molecule must be in a state with higher energy than that of an excited state electron in a neutral molecule. Consequently, the CT exciton must have a higher energy than the singlet exciton. From this charge transfer exciton, the intermediate state is created by a thermal redistribution of electrons to the two molecules in a process called back-electron transfer [4, 25]. This process demotes the charge-transfer electron to the triplet state and promotes the opposite-spin orientation electron to the triplet energy state of the neighboring molecule; creating the intermediate state exciton. More details on the mediated state, including its applicability to specific materials, may be found in Ref. [3].

Both the direct and mediated mechanisms describe the state mixing process. They both begin with an excited singlet state and a neighboring ground-state molecule, and end with the intermediate state superposition of singlet and triplet excitons. The most notable difference between the two is that the direct mechanism can be isoenergetic, while the charge transfer exciton of the mediated mechanism requires energy additional to the initial excitation. These mechanisms are presented here as background for the creation of the intermediate state, which we later propose to have observed in our experiments. Our research does not attempt to prove one mechanism over the other because our results do not rely on which mechanism facilitates singlet fission in rubrene single crystals.

The intermediate state is destroyed when the entangled triplet pair, which is also in a superposition with the excited state singlet molecule and ground state molecule, thermalizes with the environment's thermal bath [3]. This is called triplet-pair dissociation, which breaks the superposition state and leaves two independent triplet excitons. These triplet excitons are able to diffuse away through the material and decay separately. This final step of fission, triplet-pair dissociation, uses two molecular pictures in its description that we identify for future discussions.

We can describe fission's states using either the dimer picture or the crystal picture. The dimer picture considers the bare minimum required for fission to occur, two neighboring molecules (note: we are not referring to dimer polymer molecules here, only the interaction of two molecules.) This is different from the crystal picture, which considers many molecules simultaneously. The dimer picture was used above for the description of two molecules simultaneously in the triplet character of the intermediate state. Considering only two molecules is mentally and computationally accessible, although direct applications of the dimer model are limited to very specific experimental systems. Most systems with singlet fission require interactions from multiple neighboring molecules, which are accounted for using a crystal picture [19]. The crystal picture was used after triplet-pair dissociation to describe independent triplet excitons diffusing over many lattice sites. Compared to the dimer picture, the crystal picture is more complicated, though it helps build a more complete model of the processes occurring during the experiments on molecular crystals. Both of these pictures are used again to describe the reverse process of singlet fission: triplet fusion.

Fusion

When two independent triplets meet in a molecular crystal, the reverse of singlet fission may occur which is called triplet fusion or triplet-triplet annihilation. The term triplet fusion is used to describe the process from two independent triplets to one intermediate state exciton, as seen by:

$$M \underset{k_2}{\leftharpoondown} T_1 + T_1. \tag{2.2}$$

where all terms are the same as singlet fission in Eq. 2.1, except the arrows reverse and the rate k_2 describes the processes of *triplet fusion*.

Just as singlet fission conserves net spin and total energy, so too must triplet fusion. The two independent triplet excitons must be of opposite (or zero) spin components to conserve spin while recreating the intermediate state exciton; if they have the same spin component, they can not undergo triplet fusion. Energy conservation through triplet fusion requires that the triplet state energy be at least half of the singlet state energy (so that $E_S \leq 2E_T$); similar to fission, this process is also known to be assisted by thermal energy and phonons in some crystals [3]. Taking the fusion energy consideration in context with that of singlet fission ($E_S \geq 2E_T$) it is seen that singlet fission and triplet fusion can only occur simultaneously in a material if the singlet state energy is close to twice the triplet state energy; a rare criterion in materials.

As part of the intermediate state's superposition state, the singlet character of the intermediate state determines its energy and total spin. Using this singlet character, the intermediate state is able to emit light that is identical to that of the pure singlet state because they have the same energy. Because the excited singlet and intermediate state excitons have the same energy, an exciton in the intermediate state is functionally equivalent to an exciton in the singlet state, which is why the intermediate state does not return to the excited singlet state in Eq. 2.2 or in the summary below.

To wrap up the last few sections on fission and fusion, a summary of the terminology used in this dissertation for the excitonic processes is shown in Fig. 2.3.

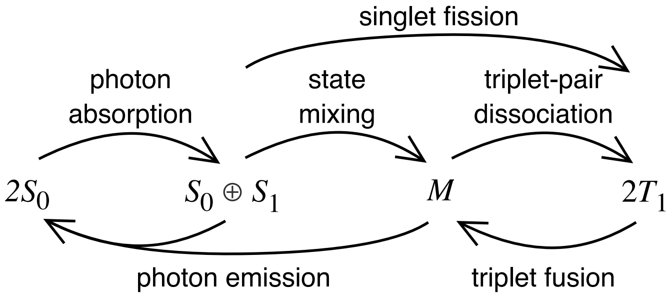

Figure 2.3: Terminology summary for fission/fusion processes. S_0 is the ground state molecule, S_1 is a excited singlet state, M is the intermediate state, and $2T_1$ represents the two independent triplet excitons.

Clarity in terminology used to describe the processes involved in fission and fusion is important to ensure that research is correctly compared between literature sources. For this dissertation, the process of singlet fission is defined as the entire process from a singlet exciton to the final two independent triplet states, which parallels the standard definition of fission (a similar process outside of molecular crystals is called multi-exciton generation [17].) In contrast to our definition of fission, some literature references use fission to describe the transformation of the singlet exciton state to the intermediate state, while others use fission to describe the dissociation of excitons into free carriers [26]. Another term with variation between sources is the intermediate state; some references refer to the intermediate state as a triplet-triplet correlated pair or the multi-exciton state. The term 'multi exciton state' is particularly confusing because other references use it to describe the final two independent triplets.

2.1.3 The Polyacene group

Acene compounds (also known as the polyacenes) are a subset of a larger group of polycyclic aromatic hydrocarbons categorized by their repeated benzene rings, complex electron-sharing scheme, and simple composition (made of only carbon and hydrogen). The acene group is extensively studied for its geometrically regular shape and natural abundance as a component of hydrocarbon materials [27, 28].

The members of this group are named for the number of benzene rings fused together: naphthalene is comprised of two fused benzene rings, anthracene has three rings, tetracene has four, and pentacene has five, etc. (naming continues with greek prefixes). Because of the similarities in the acene group's properties and molecular structures, acenes are used as a progression of molecular length to study aromatic hydrocarbons.

In a very simplified physical model, the acene family of compounds can be identically described as quantum wells with varying dimensions. The excited states of the molecules can be understood in a 'particle in a box' model, where the size of the box changes from one acene molecule to the next. Shorter acene molecules have higher absorption and emission photon energies, similar to the excited states of the 2D particle in a box having higher state energies for smaller length dimensions. Altering the molecular length does not effect the singlet and triplet state energy levels equally; increasing the number of fused benzene rings between acene molecules decreases the singlet state to triplet state energy ratio, $\frac{E_S}{E_T}$. In short acene molecules, $\frac{E_S}{E_T}$ is less than two, so singlet fission requires some input energy (which is usually provided by thermal energy or phonons) while triplet fusion releases energy. However, longer acene molecules have a $\frac{E_S}{E_T}$ ratio greater than 2, which means fission releases energy and triplet fusion requires energy. This trend is quantified by comparing singlet fission in anthracene (which absorbs 0.5 eV of energy), to tetracene (which absorbs 0.18 eV), and to pentacene (which releases 0.11eV) [4]. As discussed in the section on triplet fusion, there is a very special case among the acene molecules when the ratio $\frac{E_S}{E_T}$ is very nearly two. The energy ratio in tetracene is small enough that tetracene fits into this category, thanks to assistance from thermal energy, and shows signs of both fission and fusion. However, fission in the tetracene derivative rubrene is very close to isoenergetic, within 0.1 eV [29, 30], so rubrene shows efficient exciton fission and fusion simultaneously which leads to an interesting enhancement in photoluminescence yield.

Rubrene, with efficient singlet fission and triplet fusion, exhibits a factor of 12 enhancement of the photoluminescence quantum yield at higher excitation powers due to a recovery of triplet excitons from triplet fusion [31]. This effect is also seen in tetracene, but only shows a factor of 3 enhancement [32]. For these experiments, we learn that the triplet exciton density can be used to control the number of fusion interactions between independent triplet excitons. In a regime of low triplet density, the amount of photoluminescence emitted by the sample is linearly proportional to the excitation rate. In this regime, the probability of two independent triplet excitons colliding with the correct spin and undergoing triplet fusion is low. This means that energy from singlet excitons that undergo singlet fission is lost as a triplet exciton to non-radiative processes. However, a high-density triplet population with active triplet fusion is able to recreate the intermediate exciton state from independent triplets. The intermediate states recreated by the triplets are able to emit photoluminescence additional to emissions made immediately after excitation by radiative singlet exciton decay. It is the additional photoluminescence recovered through fusion from the triplet excitons that increases the total quantum yield of system. Excitonic energy can be reused many times through fission/fusion processes, increasing the likelihood that this energy will eventually contribute to the total emitted photoluminescence. It is important to recognize that rubrene, with both fission and fusion, exhibits a regime of high excitation density with triplet fusion recreating singlet excitons and a regime of low excitation density with few triplet fusion events. These two regimes allude to two different excitonic environments which should be controlled and reported in publications to ensure comparable results between experiments.

2.2 Rubrene

This dissertation focuses on excitonic processes in rubrene (tetraphenylnatpthacene, $C_{42}H_{28}$) as a model system for studying excitonic processes because of its high excitonic fission/fusion probabilities, long triplet exciton lifetime, and extended triplet exciton diffusion length. Although not of use in the present work, rubrene is also studied because it has one of the largest hole mobilities measured in any organic molecular crystal [33, 34] and shows a large delayed photocurrent due to triplet-pair dissociation [35, 36]. It would be interesting to understand how rubrene facilitates these properties to be able to engineer other materials to exhibit similar characteristics. The physics involved in rubrene's fission and fusion processes is vital to knowing how to create photovoltaic devices that rely on fission to double their quantum efficiency.

The research field dedicated to rubrene is still developing. Research groups are working to reconcile conflicting results, which helps to explain some finer details. Recently, an understanding of the anisotropic structure of rubrene has led to a better model of triplet exciton diffusion and an explanation of variations in the photoluminescence and absorption spectra [37, 38]. Additionally, a strong photoluminescence enhancement from the recovery of triplet excitons, as mentioned in the acene section, has been observed in rubrene which stresses the need for excitation control during experiments [31]. This dissertation builds on these results by carefully measuring photoluminescence under various environmental conditions with spectral, spatial, and time-resolved measurement techniques.

2.2.1 Fundamentals

Rubrene is a polycyclic aromatic hydrocarbon composed of a tetracene backbone (four fused benzene rings) with two substituted phenyl groups attached to each of its two internal rings. It has a two-fold axis of rotation (along the M molecular axis as as shown in Figure 2.4 a)). Rubrene single crystals grown using vapor transport are orthorhombic, with four molecules per unit cell [40]. The crystallographic axes used in this dissertation (shown in Fig. 2.4 b)) are defined in the *Acam* space group, with lattice constants $a = 14.4\,\text{Å}$, $b = 7.18\,\text{Å}$, and $c = 26.9\,\text{Å}$. The *Acam* definition is used to remain consistent with research in charge transport, though some publications use the *Cmca* point group. In the *Cmca* group, the a and c axes are switched when compared to the *Acam* group.

There are two types of rubrene single crystals: stubby crystals and extended-facet platelets. Stubby crystals, pictured in Fig. 2.4 c and d, exhibit many $\{ijk\}$ surfaces, usually including ab and bc surfaces. The most common type of crystal is a platelet

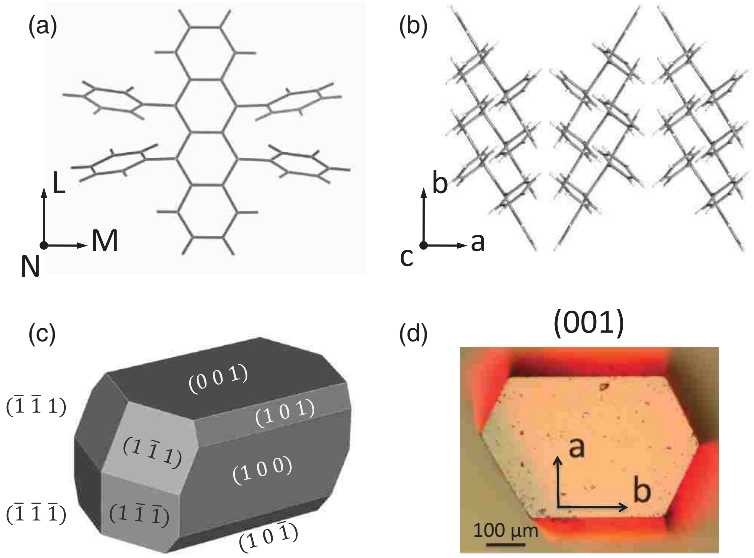

Figure 2.4: (a) Rubrene molecule. (b) Herringbone pattern of rubrene molecular stacking in *ab* plane. (c) Simulated geometries of rubrene crystal [39]. (d) Image of a micrometer-sized stubby rubrene crystal. Figure ref: [38], using *Acam* point group.

crystal with an extended *ab* surface of a few mm^2 in area and a few tens of μm extension along *c*. Though very rare, platelet crystals with an extended *bc* surface are experimentally easier to work with because of relatively stronger absorption and photoluminescence compared to *ab* surfaces. Considering the *ab* and *bc* platelets, we are able to access directly each of the three crystallographic axes as needed without worrying about mixed axial angles.

2.2.2 Absorption & Photoluminescence Properties

Rubrene molecules, like those in the polyacene group [3], have their first dipole transition moment along the molecular short axis (M). Following the long molecular backbone in Fig. 2.4a into Fig. 2.4b, it can be seen that all the transition dipole moments of rubrene molecules in rubrene single crystals are oriented exactly parallel to each other, along the *c* crystal axis (out of the page in Fig. 2.4b.) This alignment of the transition dipole moments corresponds to very strong absorption

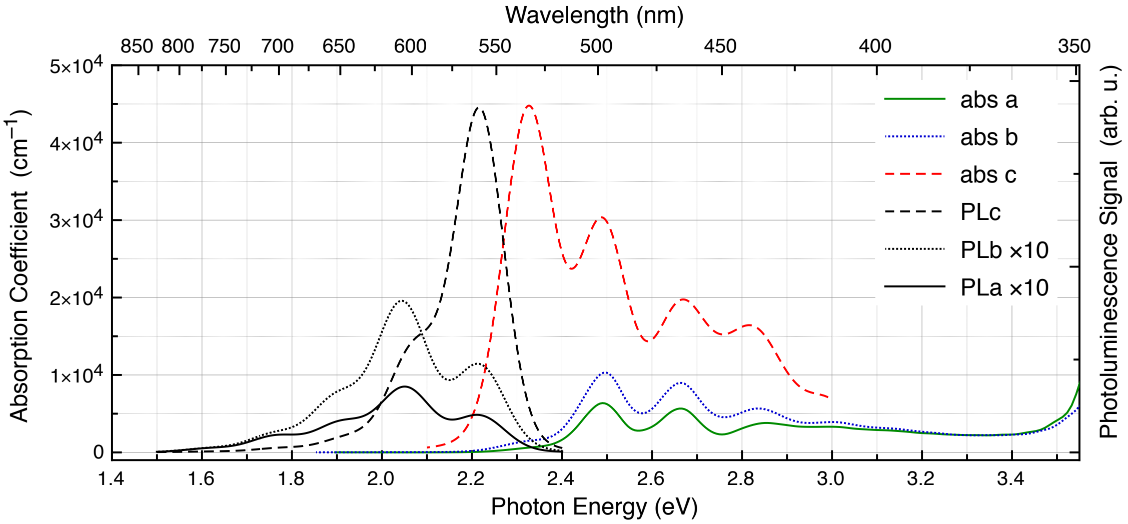

Figure 2.5: Rubrene absorption and photoluminescence spectra. Figure Ref: [38]

and emission of light with polarization parallel to the c axis. The first electronic transition for c polarized light in rubrene is at 2.3 eV, which is absent from the absorption spectra for the a and b polarizations (this trend is seen in Fig. 2.5.) Lower-energy absorption peaks, present in all three polarizations, are spaced evenly 0.17 eV apart and stem from a vibronic progression with the stretching frequency consistent with Raman measurements of carbon-carbon stretching vibrations [38]. Photoluminescence bands follow the same polarization dependent pattern as seen for absorption, with the c-polarized emission band at 2.2 eV largely absent from the a and b polarizations. We note that there is some PL 'leakage' from the c polarizations into the a and b polarization spectra, which deforms the shape of measured spectra slightly. A vibronic progression is also present in the photoluminescence spectrum, but spaced slightly closer at 0.147 eV. The energy difference between the largest absorption peak and smallest emission peak, a Stokes shift of up to 0.1eV, is attributed to lower frequency molecular deformations [38].

Because of the strong anisotropy of optical properties, measurements of photoluminescence from rubrene single crystals are very sensitive to collection geometry and material irregularities. Changing the excitation polarization or collection angle of photoluminescence affects the molecular axes from which PL is collected, which changes the relative intensity distribution of PL. This is especially clear when using microscope objectives with different numerical apertures to capture light coming from various emission angles because the *c* polarized emission band ‘leaks’ into measurements with larger collection angles. Furthermore, the edges of crystals act as reflecting surfaces by which light propagating in the crystal can ‘leak’ into other axes (usually seen in *ab* surface measurements.) Defects, cracks, dirt, and scratches on the surface of the crystal have the same effect as edges when it comes to the mixing of photoluminescence from other facets. Photoluminescence that radiates in the crystal for a substantial distance, whether in the plane of the crystal or from emission deep within the crystal, will exhibit reabsorption effects on the higher-energy end of emitted spectrum. Many of these experimental observations were first collected in rubrene by Irkhin et al. [38], who published a comprehensive analysis of absorption and emission of rubrene single crystals which highlights the anisotropic nature of its photoluminescence and absorption. These authors also show experimental artifacts to avoid during experiments in order to collect data in a well-controlled and reproducible way.

‘Altered’ vs ‘Pristine’ Rubrene

Within the past several years, most of the groups that synthesize rubrene single crystals have reported a pronounced 1.9 eV (650 nm) emission band in rubrene single crystals. We refer to rubrene crystals with this noticeable extra band as ‘altered’ rubrene in accordance with previous work [38]. Studies on the appearance of this band suggest it is due to defect sites [41] or an oxidation of rubrene molecules [42, 43]. Synthesis of ‘pristine’ rubrene, which has the intrinsic photoluminescence described above and does not have the pronounced 1.9 eV band, has proven to be very difficult to synthesize reproducibly. The 1.9 eV emission band can be the prominent emission band [30, 44], or, more commonly, it can be only a mild deformation of the vibrionic progression of the intrinsic rubrene photoluminescence. The variation in the strength of this band may be indicative of a different crystal structure [41], with possibly different physical phenomena than ‘pristine’ rubrene. This dissertation tests some properties of ‘altered’ rubrene single crystals to compare with ‘pristine’ rubrene measurements, though we do not conclusively identify the band’s origin.

2.2.3 Excitons in Rubrene

As discussed in section 2.1.2, excitons in organic molecular crystals can undergo fission by which one singlet exciton is divided into two triplet excitons on neighboring molecules. The reverse of the fission process, where two triplet excitons on neighboring molecules combine to recreate an exciton of singlet character, is known as triplet fusion and is studied much more rarely among materials, but is nevertheless found to occur in rubrene and is attributed to a singlet : triplet energy ratio very close to 2 [11].

Singlet excitons in rubrene have a radiative lifetime of around 16 ns according to experiments using rubrene dissolved in non-polar solutions [45, 46]. Measurements of the time-dynamics of the photoluminescence of rubrene show that, at high excitation powers, less than 5% of photoluminescence from rubrene single crystals comes from singlet excitons radiatively decaying within the 16 ns decay lifetime. The remaining photoluminescence is emitted long after the singlet lifetime and thus must originate from molecules that have gone through both the fission and fusion energy recycling processes [31, 45, 47]. The large probability for a singlet exciton to undergo fission, which stems from efficient singlet fission, makes rubrene a great system for investigating excitonic fission and fusion.

It is known that triplet excitons are present in rubrene samples within 10 ps after photoexcitation [30, 48]. Triplet excitons have a relatively long lifetime of 100 μs [47] due to the spin-forbidden transition from the triplet state to the ground state. This means that triplet excitons have time for spatial diffusion, enabling them to find other triplets and undergo exciton fusion. Beginning at the ~10 ns time scale, triplet fusion to the intermediate exciton state leaves a distinctive power law slope of 2 in the photoluminescence time dynamics [47].

Trying to pinpoint the state mixing lifetime has proven to be much more difficult.

The fission timescale must be shorter than the singlet decay time, made evident by the possibility of singlet fission. A measurement of transient absorption kinetics for near infrared wavelengths is interpreted by Furube et al., and presents a singlet to triplet fission time constant of 10 ps [49]. Ma et al. find a $\sim$ 20 ps singlet fission time from the lowest vibration state using experiments which study photo-induced absorption bands in the visible spectral region [30, 48]. In a third measurement, Tao et al. measured the decay of a photo-induced infrared absorption band and concludes there to be a $\sim$ 100 ps decay time for the dissociation of singlet excitons [50]. Tao et al. do not claim to be measuring the singlet fission time, but instead the charge carrier dissociation time. Their conclusion is treated as a possible component or energetic pathway. The total fission rate, where independent triplets are made, is different than measurements of state mixing and triplet-pair dissociation. Considering the sources collected here, we find a literature value for the fission time on the order of $\sim$ 10 ps.

Triplet excitons, with their long lifetime, have the possibility to diffuse long distances in rubrene. Comparing the spatial distribution of photoluminescence emitted by the crystal with the input excitation distribution provides a measurement of triplet exciton movement in rubrene single crystals. The triplet lifetime of 100 μs, which is 10^7 times longer than the singlet lifetime, provides triplet excitons with enough time to diffuse $\sim 4\,\mu$m along the b crystallographic axis. Diffusion of triplet excitons along the a or c axes is immeasurable with this method, though it is expected to be small because large molecular spacing and weak pi-orbital overlap do not facilitate triplet diffusion [51]. The diffusion effect was first reported in Ref.[37], and can be used to measure triplet mobility and lifetime by introducing defects using proton irradiation [51]. Crystals previously irradiated with a high dosage proton beam do not show exciton diffusion because of a broken crystalline structure and defect interactions between proton beam damage and triplet excitons [51]. In contrast, the same effect is not seen at lower proton-beam dosages because of the decreased likelihood that a triplet exciton will encounter a defect site. The effect of proton beam irradiation has been shown to reduce the efficiency of triplet diffusion; experiment confirms the absence of any photoluminescence enhancement between high and low triplet density regimes (as described in the acenes section) for triplet exciton recombination in highly irradiated rubrene single crystals [51].

2.2.4 Rubrene Samples Used in This Work

Almost all experimental work presented in this dissertation uses rubrene samples. We use mostly *ab* facet platelet crystals because they were widely available, have an extended facet size, and are largely free of defects. Most single crystals used in this work were grown by the Podzorov group at Rutgers using vapor transport deposition techniques. Both the Sassella research group at the University of Milan Bicocca and the Batlogg research group at ETH Zürich sent rubrene single crystals for spectral absorption and photoluminescence investigation. The Podzorov and Batlogg groups source their rubrene powder from Sigma-Aldrich [52], while the Sassella group uses ACROS Organics rubrene powder [53]. We created the amorphous, solution, and molten samples used in this work with rubrene powder from ACROS Organics.

'Pristine' rubrene single-crystals used for this work were chosen to minimize effects of an enhanced 1.9 eV band (discussed in section 2.2.2), whereas for 'altered' crystals we looked for crystals that maximized this peak.

When performing experiments on rubrene single crystals under a microscope, we transferred the rubrene to a clean, glass microscope slide. Measurement sites in all rubrene samples were chosen as far as possible from crystal defects and edges to avoid the PL spectra artifacts described in Sec. 2.2.2. The geometry of the setup to measure time dynamics required us to vertically mount our rubrene samples, which was done by securing the rubrene to an aluminum washer with Scotch tape.

We created amorphous rubrene samples using molecular beam deposition of rubrene powder onto glass coverslides [54]. Our process will be well-documented later in Sec. 4.3.

Solutions of rubrene were made in ethanol, chloroform, and hexanes by saturating the solvent with rubrene powder. We allowed excess, undissolved rubrene to settle in the cuvette before starting measurements.

A sample of molten rubrene was created by inserting rubrene powder between a microscope slide and a coverslip. The microscope slide was heated on a hotplate to 340° C until the rubrene melted. It was then allowed to slowly cool to room temperature. The sample appears to have a few nucleation sites from which molecules have approximately arranged themselves radially. This is made evident by placing the sample over a light source between crossed polarizers to see the radial orientation of rubrene molecules around the nucleation sites.

Chapter 3

Photoluminescence From Rubrene Single Crystals: Temperature and Magnetic Field Effects

Studying the light emitted by a material is one of the best ways to obtain information about the electronic states it can host. For example, the emission and absorption spectra of rubrene depends on its exciton energy levels and the crystal orientation. Furthermore, changes in measured quantum yield are indicative of changes in the rates of singlet fission and triplet fusion [31]. This chapter presents experiments measuring steady-state photoluminescence by investigating some of these complicated exciton processes in rubrene. In particular, our analysis focuses on environmental conditions that effect the singlet fission and triplet fusion rates, including temperature and magnetic field.

In our experiments, we change the temperature of our sample between 300 K and ∼150 K. Experiments which change the sample temperature modify the amount of available thermal energy to complete endothermic reactions with energy deficits on the order of $E_T = k_B T$. For rubrene, the singlet exciton energy is very nearly twice the triplet exciton energy, differing by only a tenth of an eV [29, 30]. If fission in rubrene requires more energy than the thermal energy at 150 K, the rate of singlet fission should decrease when cooling. We observe this change in singlet fission as an increase in amount of PL emitted by the system because the singlet excitons will radiatively decay instead of undergoing singlet fission.

In other experiments, we apply a magnetic field to our rubrene single crystals. The presence of a magnetic field in an excitonic system causes slight modifications to the energy levels of triplet excitons through the Zeeman effect. In a first-order approximation, the change in energy levels from a 1 T magnetic field is on the order of $\mu_B B \sim 0.06\,\mathrm{eV}$. Changes to the energy levels of the triplet excitons would alter how much energy the singlet fission process requires, which would change the singlet fission rate. We observe this change in singlet fission rate as an increase in amount of PL emitted by the system because the singlet excitons will radiatively decay instead of being lost to triplets.

These changes in PL seem as if they are unrelated macroscopic effects, but when we look more closely, we are testing very specific excitonic processes. By testing the temperature dependence of PL emitted from rubrene we are measuring changes to the singlet fission rate and learning about the relative energy difference of singlet and triplet excitons. Furthermore, measuring the magnetic field dependence of PL emitted from rubrene tests for changes in the fission rate that are indicative of slight changes in the triplet state's energy.

Our steady-state experiments detect these changes in PL using three experimental techniques: spectrally-integrated, spectrally-resolved, and spatially-resolved. Spectrally-integrated experiments utilize photon counting methods to measure the total emission and are useful for applications with low-PL signal. Spectrally-resolved measurements give us more information by telling us the specific radiative transitions used by excitons in our sample, although it requires higher PL signals than the integrated PL measurements technique. The third technique measures the position at which PL is emitted relative to where we excited excitons so we can deduce how excitons move through the sample. Using these three techniques to measure changes in PL from a magnetic field or reduced sample temperature create powerful tools to gather information about the excitonic states, their transitions, and movements in rubrene single crystals.

3.1 Experimental Details

This section details the experimental setups we use for the work described in this chapter. We describe the excitation sources, the optical components, the PL measurement modules, and the Cryostation which we used to change the sample temperature and apply a magnetic field.

In a material like rubrene, where singlet exciton fission is the dominant decay mechanism, the amount of photoluminescence measured from a rubrene sample depends on how much energy is radiated away before singlet excitons undergo singlet fission. We use the term ‘photoluminescence yield’ to describe the number of PL photons divided by the number of excitation photons; we do not analyze these two values directly, but instead measure their relative variation. For example, we will see that applying a magnetic field to rubrene will slightly increase the PL yield; which enables us to extrapolate that less energy in the crystal was lost to non-radiative processes. For rubrene, this can mean that singlet fission was reduced. This discussion makes it clear that we need experiments that can collect PL from rubrene while changing the sample temperature or applying a magnetic field in order to extract information about their effects on singlet fission and excitons.

Confocal microscopy is a widely-used tool that can be adapted for spatial and spectral measurements of photoluminescence. Figure 3.1 shows the configuration employed in this work, but also describes the general implementation of confocal microscopy using a diode laser. We use a confocal setup because of its flexibility in geometry, input sources, signal filtering, and detection methods. Another advantage of using confocal microscopy in our experiments is its ability to block light that is not in-focus at the sample by using an aperture. An aperture in our setup removes light coming from above or below the sample and limits collection to only the depth of field of the objective so we know exactly where on our sample the measured PL is collected.

For steady-state experiments in rubrene, we excited our sample with one of two ThorLabs Collimated Laser Diodes centered at 450 nm (2.76 eV) or 532 nm (2.33 eV) with maximum outputs of 4.5 mW. We chose to use the 2.76 eV laser for its larger

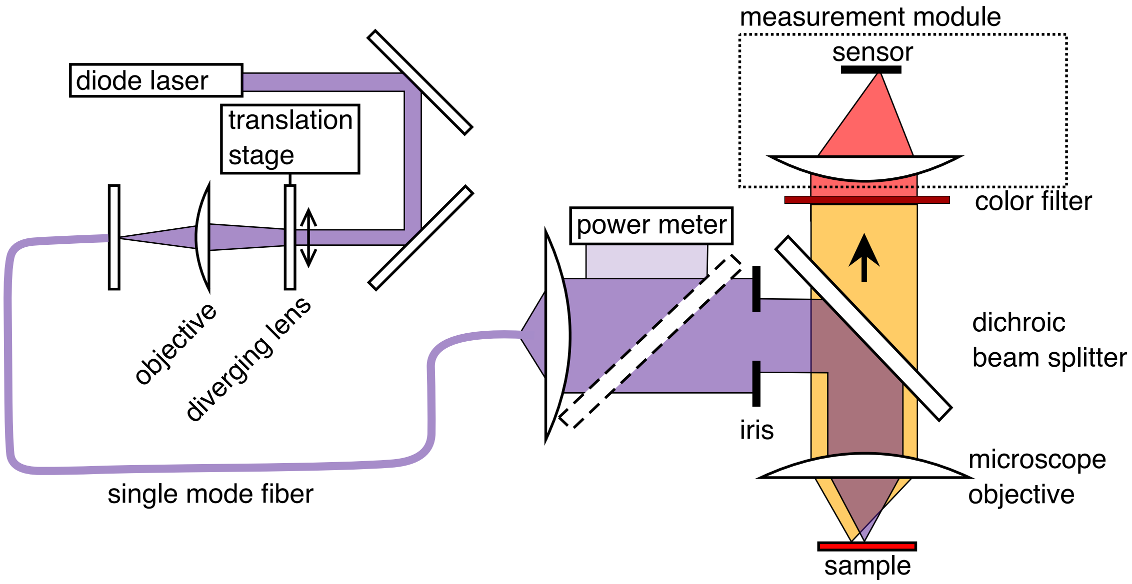

Figure 3.1: Experimental configuration used for most measurements discussed. The dotted box region 'measurement module' surrounds the region of the configuration subject to change between photon-counting, spectroscopy, and diffusion experiments.

energy difference from the PL emission of rubrene (which starts at 2.21 eV) so it's easier to block the excitation beam. This laser was coupled into a single mode fiber, then collimated into the confocal microscope. The laser beam in the microscope was split to create a secondary beam, which is used to measure excitation power by means of a Newport 1830-C Optical Power Meter. The primary beam continues into the microscope, passes through a rotatable linear polarizing plate, and then reflects off a dichroic mirror into the objective which focuses the excitation light on the sample. The objective we used varied by experiment and was chosen based on the excitation density and magnification needed (described in 'imaging module' section on page 30).

To detect PL while changing temperature and applying a magnetic field, we built a confocal microscope compatible with the Cryostation system available to us that could perform these environmental changes. Further, we designed this microscope to have three interchangeable detection modules that perform the three experiment types previously described: one for spectroscopy, one for ultra-sensitive photon counting, and one for direct imaging.

Spectroscopy Module

We used the spectroscopy module for work described in sections 3.2.2, 3.2.1, and 4.3 to spectrally-resolve the photoluminescence emitted by rubrene single crystals. In addition, it was used to determine whether a sample is 'pristine' or 'altered' and to help identify rubrene's crystallographic axes. This module was designed to use a 75 mm lens as the microscope objective, which creates a Gaussian beam profile with full width at half the maximum (FWHM) of $\sim 40 \mu$m at the sample's surface that can excite and measure PL from a sample inside the cryostat.

Photoluminescence passed through a 490 nm longpass dichroic mirror and a 500 nm longpass dichroic filter to attenuate the excitation beam as much as possible. The remaining signal was focused by a 50 mm lens into a multimode fiber with a core diameter 100 μm. PL captured by this multimode fiber was detected by an Ocean Optics 4000 USB spectrometer which provides us with a measurement of the PL spectrum.

Integration times for the spectrometer were set in relation to the signal intensity; generally about 50 ms for high-intensity signals and 5000 ms for low-intensity signals. To remove any background effects, we collected a dark spectrum for each measurement by covering the excitation beam in the microscope, then manually subtracted it from our PL spectrum.

Photon-Counting Module

We used the photon-counting module for the experiments described in section 3.2.2 that measure integrated PL through a large range of PL powers. This module's strength over the spectroscopy module is that it can detect much weaker signals.

PL passed through the 490 nm longpass dichroic mirror and the 500 nm longpass dichroic filter to attenuate the excitation beam as much as possible; the remaining light was focused into a multimode fiber with a core diameter 100 μm by a 50 mm lens. PL captured by this multimode fiber was decoupled onto the sensor of a Micro Photon Devices PDM Series photon counting detector. When a photon is detected, this detector sends a clear, countable pulse to a Stanford SR400 Two-Channel Gated Photon Counter, which is triggered to count these pulses.

We used neutral density filters before the photon counter to keep the count rate less than 200,000 counts per second. We did this so that the probability that a photon arrives during the dead time of the detector (when it would not be counted) is less than 1%.

We counted photons for 30 seconds in each measurement, covered the laser in the microscope, then collected a background count to subtract from the PL measurement to remove the photon counter's unavoidable 'dark counts' from our data.

Imaging Module

We used the imaging module in all experiments to visually inspect each sample, pick excitation sites free of defects, measure the excitation beam profile for each experiment, and measure the spatial distribution of PL from rubrene single crystals. We used ImageJ to extract cross-sections of detected light to extract the excitation beam's FWHM and PL cross-sections, as described in section 3.3.

Imaging our sample used the basic microscope core with an objective we chose to determine the magnification of the system. We had the flexibility of choosing between a 75 mm lens, 10× objective, 50× objective, and a 100× objective to suit excitation spot size and spatial resolution needs. We used a 75 mm lens or the 10× objective for sample analysis and general imaging for their wide field of view that could image the sample. This allowed us to characterize macroscopic crystal properties and identify edges, cracks, and defects. To image and focus the excitation on the μm-scale, as we do in section 3.3, we used either a 50× or a 100× objective. Imaging with the Olympus UPlanAPO 100×S objective is very clear, with 19.7 pixels/μm resolution, but has a 200μm working distance that is incapable of imaging our samples in the cryostat. In contrast, our 50× Mitutoyo Plan Apo Infinity Corrected

Objective could image samples in the cryostat and magneto-optical chamber because of its 1.2 cm working distance, but has a spatial resolution of 3.6 pixels/μm. We preferred to use the 100× objective for micrometer-scale PL experiments outside the cryostat for its increased resolution. PL from the objective passed through the 490 nm longpass dichroic mirror, then went through a yellow-glass 500 nm longpass filter to remove the excitation light.

The filtered light is then focused by a Canon 135mm camera lens set to its 'infinity' setting to focus PL light onto a Point Grey Firefly 16-bit 1.3 MP Color USB 2.0 camera (this Canon lens was chosen because it does not show chromatic aberration). The Firefly camera allows for manual manipulation of exposure time, frame rate, gain, gamma, and white balance so that our PL detection has a linear response, and shows no background offset. We chose a 1 s exposure time for a good signal to noise ratio, turned off gain, left gamma at its default (linear response), and left white balance constant between all experiments so that our spectral sensitivity was constant through all measurements.

The Cryostation Module: Changing Magnetic Field and Temperature

We use the Montana Instruments Cryostation's magneto-optical module as described in sections 3.3 and 3.2.2 to apply an external magnetic field of up to 1 T to our rubrene samples with 1 mT resolution. First, we inserted a hall sensor so the Cryostation can calibrate its magnetic field strength, then we removed the sensor and replaced it with our sample; directly between the two electromagnet poles. We were able to adjust the magnetic field with the computer interface and changed nothing in our optical system.

Adjusting the temperature of our sample also used the Montana Instruments Cryostation's magneto-optical module, although we do not necessarily apply a magnetic field. In sections 3.2.1 – 3.3.1 we characterize how the sample temperature can be controlled in this Cryostation.

This Cryostation system uses a closed-loop helium cycle to hold the sample platform at a desired temperature with $\sim$ 25 mK degree stability. Upon cooling, the chamber displays a measurement of the chamber's pressure until it reaches 'high vacuum' at 10^{-4} Torr (it is meant to be used only to gauge whether the system is in high vacuum). In the automatic cooling and heating modes, the system controls all vacuum pumps, chamber pressures, and temperature. The rubrene sample was placed on a flat, horizontal brass sample mount, which was screwed into the sample platform; which should enable sample cooling by the system. However, the sample was not secured to the mount by a thermo-coupling medium because of the extreme fragility of rubrene single crystals. We tried using vacuum and cryogenic temperature-safe adhesives and greases to ensure thermal contact, but the samples cracked due to thermal expansion. Further complicating our temperature-dependent measurements, a thermocouple in the platform is the closest temperature measurement to the sample. Montana Instruments estimates less than 1 K variation between the platform temperature and the sample mount [55]. In presenting spectra and data collected using the Cryostation, we report the platform temperature as a 'nominal temperature' because we show that the temperature of our sample will be different.

Temperature-dependent experiments were performed through an uncoated fused silica window in the chamber lid; this was no problem for spectral measurements, although it made imaging inside the chamber considerably harder (this is described in detail in section 3.3). While the Cryostation is changing its temperature, the vacuum chamber and sample mount change their height slightly because of vacuum and thermal expansions. For this reason, it is necessary to optimize the PL collection optics before each measurement by ensuring that the microscope is focused on the surface of the sample.

We have performed PL experiments that test two methods of measuring the temperature dependence of our sample; stabilizing at a single temperature for a long time before measuring PL, and measuring PL while changing the sample temperature. Our experiments that stopped at a target temperature for up to an hour found no changes in measured PL yield after the target temperature was reached. We found that the target temperature was not reliable as a measurement of the sample temperature, and that the sample was more efficiently cooled with an atmospheric pressure of a few Torr in the sample chamber. In addition, to be careful of accumulated crystal heating at high power laser intensities (a few μW), we covered the excitation beam between measurements and collected data immediately after uncovering the laser.

The experiments described in this chapter are divided into two groups based on the type of measurement: spectral measurements of photoluminescence and spatial measurements of photoluminescence. Each type is described in its own section, and each of these two sections is further separated into two subsections describing the environmental conditions that are changed; either temperature-dependence or an applied magnetic field.

3.2 Measurements of Photoluminescence Spectra

3.2.1 Photoluminescence Variations While Cooling and Heating

Rubrene single crystals efficiently enable excitonic fission and fusion; which is a property that makes rubrene valuable for applications where an increase in the number of carriers is beneficial. As discussed in the background chapter, energy conservation through the fission and fusion processes of rubrene introduces the constraint that the energy ratio of singlet state energy to triplet state energy, $\frac{E_S}{E_T}$, is approximately 2. An energy ratio greater than two means that singlet fission would release energy, while fusion would absorb energy. However, a ratio less than two means fission would absorb energy while fusion would release energy. In rubrene single crystals, the ratio between singlet and triplet state energies is thought to be so close to 2 that thermal energy may provide the small amount of energy to enable both singlet fission and triplet fusion. This is exactly what we attempt to probe in the work described in this section by changing the temperature of rubrene single crystals; we experimentally alter the thermal energy available to the fission/fusion processes to learn about the mechanisms that allow for them to occur.

Our work is also motivated by the need to confirm results found in current literature; with some work showing a change in spectral intensity distribution, while others show a uniform enhancement of PL yield. Two literature sources that investigate the temperature dependence of the photoluminescence spectrum of rubrene use ‘altered’ rubrene crystals [30, 44], which are identified by a strong 1.9 eV peak emission (described in section 2.2.2 on page 20). The current work completes this data by presenting a measurement of the photoluminescence from a ‘pristine’ rubrene crystal.

As we will see in this experiment’s description, details about how the Montana Instruments Cryostation is operated will be useful to understand our results. We used the cryostat mostly to change the nominal temperature reported by the Cryostation between 295K and 10K. How it changes temperature is largely automated, though we are able to toggle pumps and heaters to slightly change how heating and cooling occur. For example, setting a target temperature of 150 K from 10 K will turn on heaters in the chamber and reduce cryo-pumping to increase the temperature of the sample while remaining in high vacuum condition. In contrast, using the automated ‘heat up’ function will turn on all heaters in the chamber and slowly return the system to standard room conditions by completely switching off all pumping. This ‘heat up’ function is accompanied by an increase in the nominal reported temperature, although we show that the introduction of cold air cools the sample initially before heating up to room temperature with the Cryostation platform and chamber.

A *bc* facet rubrene single crystal was illuminated with c-polarized light for most measurements we describe here due to its large relative PL emission yield and the ability to see the full PL spectrum, including the mostly c-polarized highest energy peak at 2.2 eV.

While changing temperature, the Cryostation chamber and platform translate their height slightly due to changes in pressure and thermal expansion. Because of this, the PL collection optics require constant readjustment to maintain a constant collection efficiency from the crystal surface while changing temperature. Excitation powers for these experiments were kept relatively high, at $\sim 10^{22}$ excitations/cm^3 s, because it is too difficult to optimize the PL signal to maintain a constant collection efficiency using low excitations rates. Spectral measurements of photoluminescence

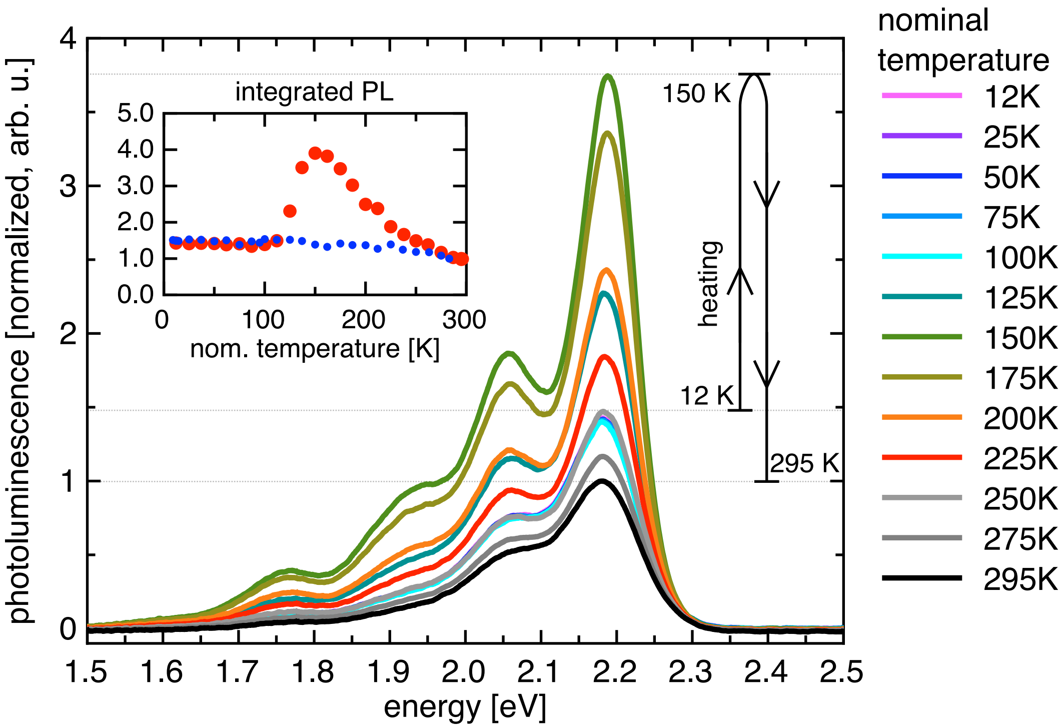

Figure 3.2: Spectral measurements on a *bc* facet of rubrene, heating through a range of nominal temperatures. Cooling measurement (not shown) can be visualized using 295 K-225 K spectra shown here, where all nominal temperatures lower than 225K coincide with each other. Normalized to peak at 295 K. *Inset:* integrated PL vs. temperature for cooling (blue circles) and heating (red squares).

were collected with the Ocean Optics USB4000 spectrometer.

Figure 3.2 shows the nominal temperature dependence of photoluminescence spectra, normalized to the spectrum peak at room temperature, from a *bc* crystal facet while it is being heated. The heating trajectory was determined by the 'heat up' button on the Cryostation which changed both the reported nominal temperature and pressure by turning on all heaters and disabling pumping. At a nominal temperature of 12 K, there is almost 1.5× the amount of photoluminescence compared to PL at room temperature. However, at 100 K, a dramatic increase in the PL appears which peaks at ~ 150 K, then decreases in intensity approaching room temperature. We show below that this PL enhancement is associated with changes in atmospheric pressure inside the cryostat chamber that actually further reduced the temperature of the sample. This atmospheric PL enhancement is only present when using the 'heat up' button on the Cryostation, which allows the system to come out of high vacuum. The red squares of the inset show the spectrally integrated PL has peak enhancement of ~ 4. However, when first cooling the sample in high vacuum there is only the factor of ~ 1.5 increase in PL between 295 K and nominally 12 K; the figure inset describes this, where the blue circles show measurements of spectrally integrated PL while the sample is cooling. Aside from a slight narrowing of vibrational bands at lower temperatures which is seen by the appearance of 'dips' between the spectral bands (a point we return to later), there are no changes to the shape of the spectrum; all peaks retain their relative amplitudes and no peaks appear or disappear from the *bc* facet emission spectrum. This shows that the energy levels involved in radiative transitions are not changed as a function of temperature, and the atmospheric PL enhancement must be from changes in the excitonic dynamics of rubrene. While we see a constant spectral shape for the *bc* facet crystal, the same is not true for 'altered' rubrene samples, which are explored next.

Figure 3.3 shows a similar measurement of PL emission as a function of temperature performed using an 'altered' rubrene crystal, which has a strong PL emission band at 1.9 eV. Similar to the intrinsic rubrene crystal, 'altered' rubrene shows an enhancement factor of about 2 between 295 K and the measurement at a nominal temperature of 12 K. Additionally, this crystal shows a similar atmospheric PL enhancement as for the 'pristine' *bc* crystal described above during the 'warm up' cycle. Further, the atmospheric PL enhancement is about twice as large as that of the *bc* crystal used for data shown in Fig. 3.2. However, we note that the atmospheric PL peak is not consistent between crystals, or even measurements with the same crystal. An extra emission band appears at 2.1 eV during the atmospheric PL enhancement, although there are no radiative emission bands at 2.1 eV in rubrene single crystals. This 2.1 eV emission falls between the first-dipole transition at 2.2 eV and the first vibrionic emission band at 2.0 eV [38]. As mentioned in the background

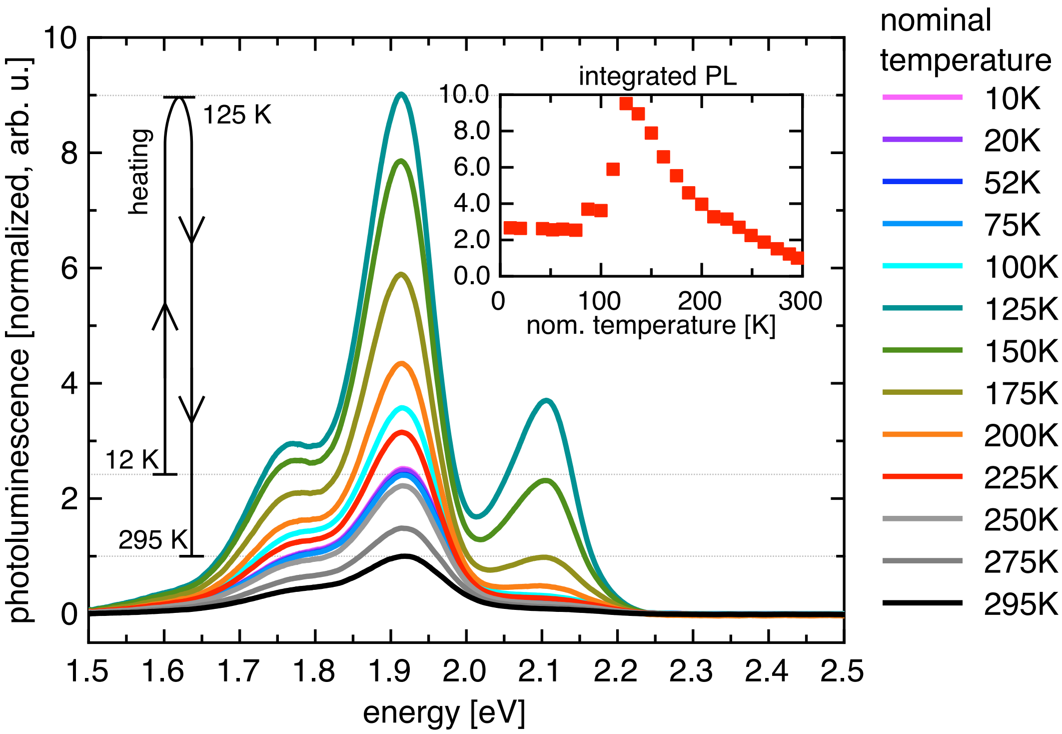

Figure 3.3: Measurements of spectra in an altered rubrene sample heating through a range of temperatures. Normalized to peak at 295 K. *Inset:* integrated PL vs. temperature (heating).

chapter, some literature sources assign the origin of extra PL emission band in 'altered' rubrene to the oxidation of rubrene molecules [42, 43], while another source assigns it to defects in the crystal lattice of rubrene [41].

What is consistent between data runs is the increase in PL yield as the temperature is lowered. This observation shows that the number of singlet excitons that undergo radiative emission must increase as the temperature drops. This can be due to a decrease in the singlet fission rate, or to a decrease in any other non radiative process. Experiments in tetracene that test the temperature dependence of fission see a factor of 100 decrease in the fission rate when cooling to 80 K [56]. This removes the energy required for tetracene to complete singlet fission, so more excitons undergo radiative emission. If singlet fission is changed in our rubrene samples, the increase in PL we report here is indicative of a small activation energy, on the order of 0.05 eV, as was reported by Ref. [30].

Two other research groups have published data on the temperature dependence of rubrene, although both use altered rubrene crystals, with the 1.9 eV band dominating their spectra. In one of the studies, Ma et al. [30] show an increase in PL of about a factor of 20 from room temperature to 125 K. The other literature source, Wen et al. [44], shows a temperature dependence with a factor of about 6 increase of PL at 77 K when compared to room temperature. The temperature dependence of Wen et al.'s spectral plots are more evenly-spaced than those published by Ma et al. through a similar temperature interval.

As for the spectral intensity distribution of measurements described in the literature, both sources show a strongly 'altered' rubrene emission spectrum. However, Ma et al.'s figure contains several extra spectral bands between 2.07 eV and 2.25 eV. Some bands they show are known rubrene emissions, but their spectra at 2.25 eV quickly approach zero which means they likely used a filter that blocks higher energy photons, complicating a detailed analysis of relative peak heights in that energy region. However, we can still extract that their data shows the appearance of an emission band at ~ 2.1 eV in the two largest PL curves (at 100 K and 80 K), which may be the same band that we observe in Fig. 3.3 during the atmospheric PL transit. We will show below that the atmospheric PL transient actually corresponds to a further reduction of the sample temperature, which increases the PL yield in a way that roughly matches the results of Ma et al. [30] Our cryostat system is designed to go down to liquid helium temperatures with pressures below 10^{-4} Torr, whereas Ma et al. use a cryostat designed for liquid nitrogen temperatures at pressures up to 5 Torr (though they may have used a pressure anywhere lower than that) which removes any possibility of an atmospheric effect similar to that reported here. To fully characterize how the Cryostation leads to an atmospheric transient, we measure the PL yield as a function of both pressure and temperature as described in the next subsection. We then use variability of PL yield with the observed spectral narrowing to prove that the temperature of the sample is reduced during the atmospheric enhancement.

Characterizing the PL Atmospheric Enhancement

The PL transient as a function of temperature and pressure is measured using the 'warm up' function of the Cryostation in the three trajectory cases shown in Fig. 3.4. Nominal temperature and chamber pressure trajectories are mapped out to show the PL transit in the same *bc* facet crystal. For each of these cases, a black arrow shows the direction of the path taken.

Trajectory case 1, shown in Fig. 3.4 a), shows that an increase in temperature up to 200 K while maintaining a high vacuum does not exhibit the PL enhancement; this is consistent with our earlier measurements while cooling the sample. We then cooled the cryostat back down to 100 K, then initiated the 'warm up' sequence. Following the path shown by the arrow, the cryostat increased both nominal temperature and pressure of the cryostat. This time, the photoluminescence transient appears when the pressure goes above 10^{-1} Torr. The PL enhancement from room temperature to the highest PL measurement is about a factor of 8. Case 1 is a very important measurement for later establishing the sample temperature. The data collected while heating under high vacuum does not show any enhancement up to 200 K, which is consistent with the reproducible PL temperature changes.

Trajectory case 2, shown in Fig. 3.4 b), shows that keeping the sample above 220 K still exhibits the transient, although the amplitude is not as dramatic with an increase of less than a factor of 2.

Trajectory case 3, shown in Fig. 3.4 c), shows that the transient is reproducible by toggling the cooling pump during a 'warm up' cycle. We started the experiment at nominally 12 K, initiated the 'warm up' process, then waited for the transient to begin. When we saw the transient, we turned the cryo-pumping system back on until the system reached high vacuum again; we saw the transient disappear as it approached high vacuum. Once in high vacuum again we initiated another 'warm up' cycle, which exhibited the transient again, although the second pass shows slightly lower PL intensity. This shows that whatever is causing this increase can be reset by returning the system to high vacuum.

Figure 3.4 d) summarizes the perceived pressure-dependence of PL by excluding

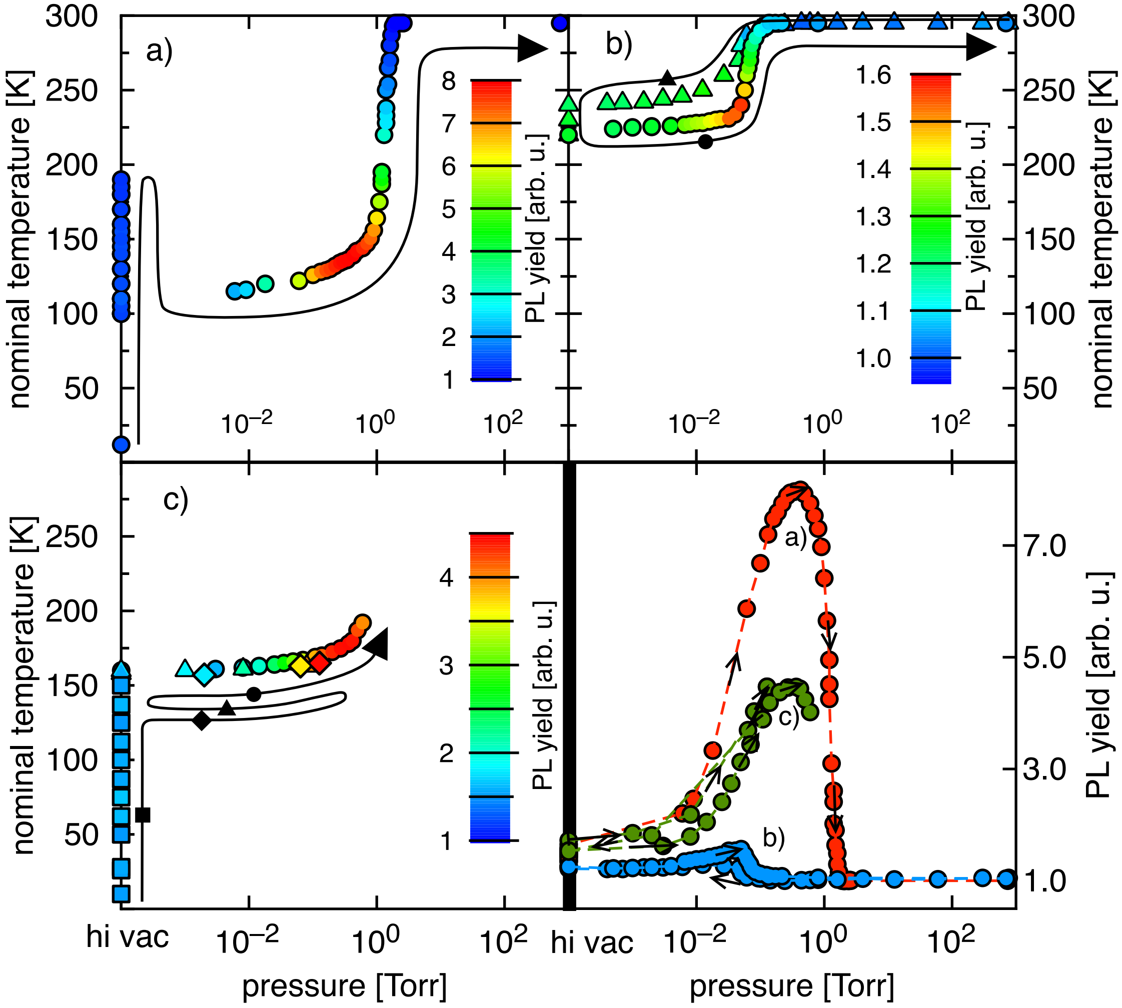

Figure 3.4: Three pressure-temperature trajectories (follow arrows and data point shapes) traced out to show photoluminescence enhancement when pressure increases. a) shows PL increase only occurs with increase in pressure because data first goes through 200 K in high vacuum. b) shows the presence of this enhancement is not tied uniquely to ∼130 K, although the effect is weaker at higher temperatures. c) shows reproducibility of enhancement when approaching from high vacuum (less than 0.1 mTorr). Lower right plot shows PL yield vs. pressure for a), b), and c) with directional arrows in the lines. (color online)

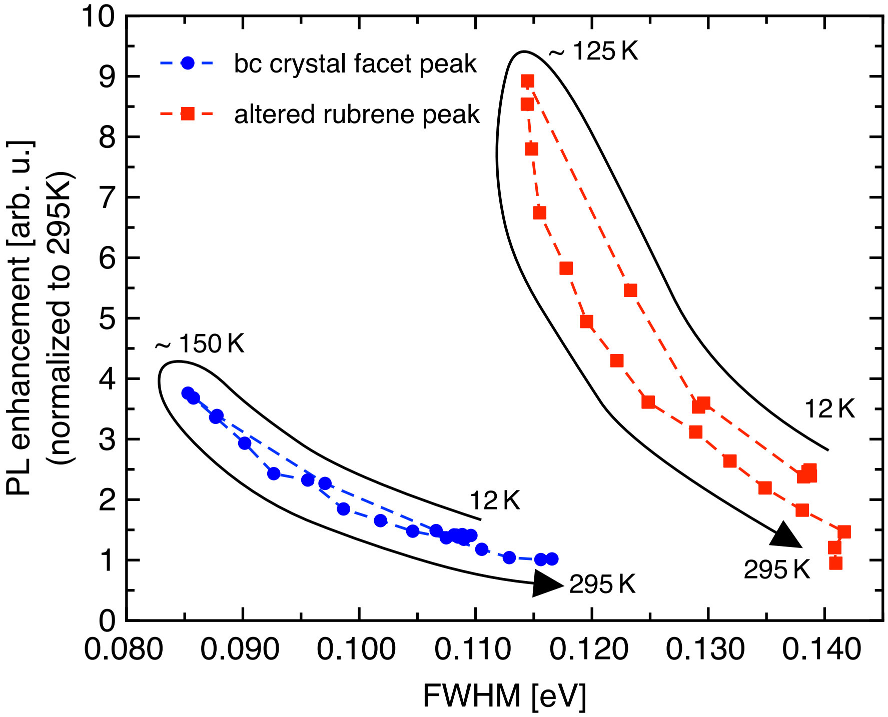

Figure 3.5: Peak PL enhancement vs. emission band FWHM for *bc* facet rubrene crystal and 'altered' rubrene crystal. Nominal temperatures displayed.

the temperature considerations. In this way, it becomes more evident that the atmospheric PL transit begins just after 10^{-2} Torr in all three cases.

Temperature Dependence of the Rubrene Photoluminescence

While it might be tempting to seek a chemical cause for the PL variations when changing the atmospheric pressure that we observed in the previous section, this cannot be easily reconciled with the approximate consistency of the intrinsic PL spectral intensity distribution and with the fact that surface modifications should not easily alter emission processes that happens several micrometers below the surface of the crystal. Instead, a closer evaluation of how the increase in PL is accompanied by an increasing sharpness of the individual emission peaks in the PL spectra leads to another, simpler, conclusion.

Figure 3.5 shows the PL enhancement as a function of full width at half maximum of the primary peak in a pristine crystal, and of the 1.9 eV band in an 'altered' crystal. It is clear from this figure that peak-width is strongly correlated with PL yield in both types of crystals. It is also well-known that the width of the spectral peaks in rubrene is expected to be strongly temperature dependent [57]. From this we conclude that the increase in PL yield caused by an increase in the atmospheric pressure inside the sample chamber must be caused by a further reduction of the sample temperature.

Combining the information in the previous section and the result in Fig. 3.5 we arrive at the following interpretation: When first cooling the Cryostation chamber to a nominal temperature of 12 K, the pressure in the sample chamber reached 10^{-4} Torr when the sample temperature was above 220 K. The sample never reached the temperature reported by the temperature sensor on the platform of the cryostat because of the high vacuum, bad thermal contact between the sample and sample mount. This led to only a small change in PL yield, on the order of only a factor of 2. When using the Cryostation's 'heat up' function, the increase in the atmospheric pressure in the chamber allowed for faster and better cooling of the sample compared to in high vacuum because the cold gas molecules efficiently removed heat from the sample. It then follows that the sample temperature initially decreased strongly before returning to a higher temperature as the heat up function progressed. After the atmospheric enhancement of the PL yield quickly reached its maximum (within a few minutes), the enhancement's disappearance correlated well with the increasing platform temperature through the automatic heat up function of the Cryostation (over some tens of minutes). Because of the slow disappearance, and because of the presence of an atmospheric pressure in the sample chamber, we can then assume that the reported nominal temperature at which the peak PL enhancement was observed at a pressure of $\sim$0.1 Torr is close to the actual temperature of the sample. When cooling in high vacuum, the sample temperature was always significantly higher than the nominal temperature reported by the platform sensor.

This interpretation is supported by the clear correlation of peak widths and PL yield shown in Figure 3.5, as well as by the correspondence between our observations and the temperature dependence of the PL spectra reported by Ref.[30]. Ma et al. [30] report an increase in PL by a factor of ∼20 when cooling an 'altered' rubrene crystal to 80 K. They show in increase of ∼9 at temperatures near 140 K (compared to 295 K), which we can use to roughly calibrate our data in 'altered rubrene'. This means that our nominal temperature was off by about 15°K when the sample is out of the Cryostation's high vacuum state. The appearance of the extra band at 2.1 eV during this crystal cooling is also found in Ma et al.'s data below 150 K, which is another confirmation of the temperature reached by the sample during atmospheric cooling.

Our *bc* facet pristine rubrene sample, used in the three cases of Fig. 3.4, does not have a thermally-calibrated reference to compare with because this is the first measurement of PL spectra vs temperature without a strongly 'altered' rubrene sample. This measurement, when calibrated to the temperatures described above, are consistent with the activation energy of 0.05 eV reported by Ma et al.. From the measurements we show here, we find a uniform change of the PL spectra across all temperatures accessed. This means that all increases to the total PL must come from decreases in the singlet fission rate due to the removal of its thermal activation energy. Ma et al. [30] found a ∼0.05 eV activation energy in the intrinsic rubrene spectral bands (with their altered rubrene crystal). Our experiments here correlate well with their conclusions.

3.2.2 Magnetic Field Changes of Photoluminescence

In the late 1960's, it was discovered that applying a magnetic field to anthracene and tetracene, with excitonic fission, decreases the photoluminescence yield of the system [58–60]. Rumyantesev et al. tested the magnetic field dependence of PL from rubrene single crystals and found that the singlet fission rate is affected by the presence of a magnetic field [61]. Their experiments show first a decrease, and then a larger increase in the PL yield with increasing magnetic field strength, which they attribute to an increase and subsequent larger decrease in the singlet fission rate of the crystal. Further, Ref. [61] reports that changing excitation power has no effect on the magnitude of the magnetic effect.

The amount of active triplet fusion occurring in a crystal with fission and fusion can be modified using the excitation power (as detailed in the polyacenes section of chapter 2). This enables us to probe the physics of our excitonic system without active triplet fusion, at low intensity, or with active triplet fusion, at high intensity [31, 32]. Rumyantesev et al. collected data between 10^{18} - 10^{20} excitations $\mathrm{cm}^{-3}\,\mathrm{s}^{-1}$ and describe it as showing no change in the magnetic field effect on PL; however, that range of excitation densities falls almost completely within the regime of low excitation power in rubrene as presented by Biaggio and Irkhin [31]. This means that all of Rumyantesev et al.'s data actually tests the low fusion rate regime in rubrene, and does not necessarily apply to data with a high triplet fusion rates; our work here completes their data set to test whether their conclusions are still valid at high fusion rates.

The current work studies an applied magnetic field's effect on photoluminescence yield through both high and low excitation powers to understand how singlet fission and triplet fusion are altered by a magnetic field. We excited singlet excitons in rubrene using a 450 nm continuous wave diode laser, which we coupled into a confocal microscope to give a FWHM spatial profile of 40 μm to minimize diffusion effects. With the FWHM of the excitation beam and the excitation powers at the sample of 50 nW for low powers and 50 μW for high power, we used Eq. A.9 to calculate the excitation density at the surface of the sample to be $3 \times 10^{19} - 3 \times 10^{22}\,\mathrm{cm}^{-3}\,\mathrm{s}^{-1}$. Excitation beams were polarized along the a and c axes for the ab and bc crystallographic facets, respectively. The b axis of the rubrene crystals was aligned parallel to the applied magnetic field. We applied a magnetic field to our rubrene samples using a Montana Instruments Cryostation magneto-optical module which was calibrated using a Hall sensor to apply up to 1 Tesla along a single axis with mT precision.

Photoluminescence from the sample passed through a 490 nm longpass dichroic mirror and a 500 nm longpass filter, which was focused into a multimode fiber for measurement. Spectrally-integrated photoluminescence measurements utilized the single-photon counting module, while spectral measurements of photoluminescence were taken at higher powers using an Ocean Optics 4000 USB spectrometer coupled to the signal collection fiber.

The top graph of Fig. 3.6 plots our spectrally-integrated measurements of photoluminescence power from a *bc* facet crystal as a function of excitation density with and without an applied magnetic field. Comparing the data from these two magnetic field strengths, we see that high excitation density measurements (greater than $\sim 10^{20}\,\mathrm{cm}^{-3}\mathrm{s}^{-1}$) shows little change in PL power upon application of a 1 T magnetic field, whereas measurements at lower excitation densities show a significantly larger PL power enhancement. This is made more clear in the bottom graph of Fig. 3.6 which plots the increase in PL yield by dividing PL power by the excitation density.

This result contains a lot of information. First, the increase in PL power with the application of a magnetic field means that non-radiative energy pathways are less likely to occur with the application of a magnetic field. Each data point in the 1 T data set of Fig. 3.6 has the same singlet fission rate since that is constant through all excitation powers; what changes with excitation density is the triplet exciton density which directly controls the amount of triplet fusion occurring in the sample. At high excitation powers, the PL measured is both from initial singlets radiatively decaying and triplets undergoing fusion, with more than 90% of the detected PL coming from triplet fusion [47]. In contrast, at low excitation rates the PL is only from initial singlets radiatively decaying and triplet excitons are not likely to fuse so their energy is then lost to heat. Because of this, an increase in PL at low excitation densities is a direct measurement of a decrease in the fission rate since there is little extra contribution to PL from triplet recovery to affect the enhancement factor. However, an increase in PL at high excitation densities is a more complicated function of the singlet fission rate because PL is the sum of contributions from the radiative decay of initially excited singlet excitons and from triplets that undergo fusion; this means that PL from recovered singlets makes PL from changes to the initially decaying singlets appear smaller.

To better understand the magnetic field effects on PL, we measured photoluminescence spectra as a function of increasing magnetic field for both high and low excitation densities. We normalized the spectra by dividing by the 0 mT curve peak

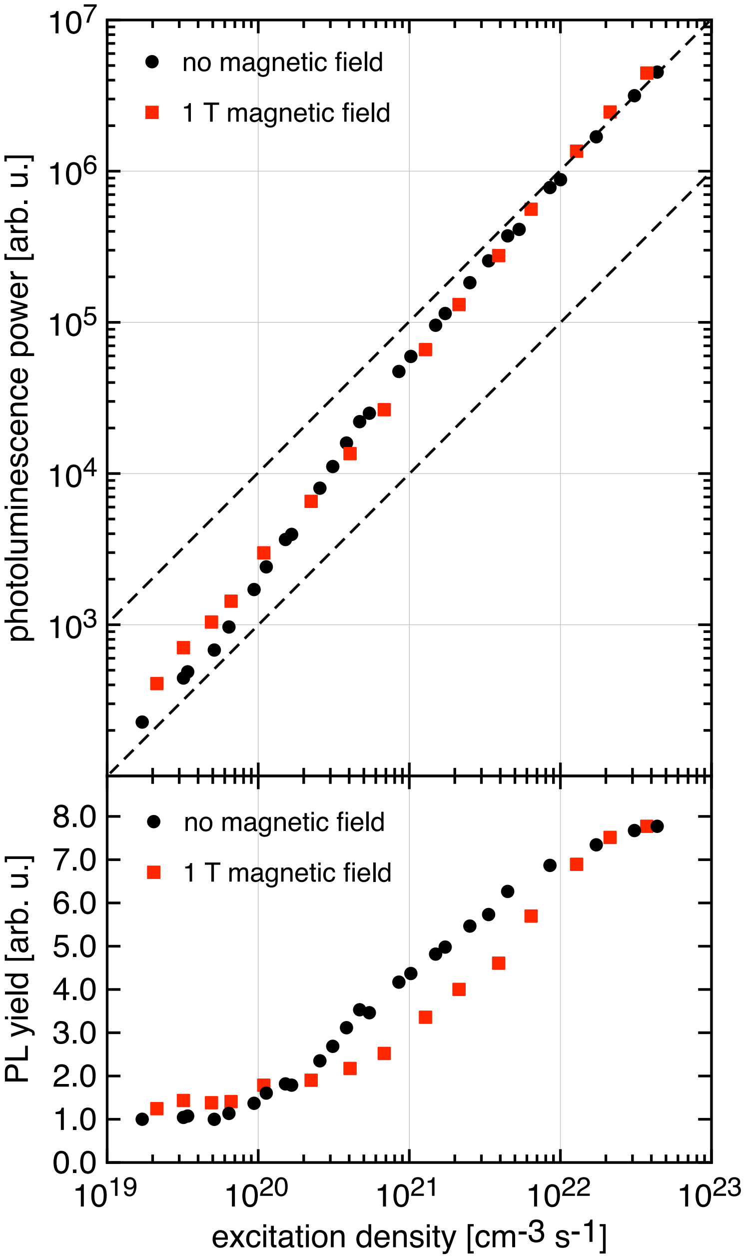

Figure 3.6: Photoluminescence enhancement with and without a 1 Tesla magnetic field applied along the b-axis of the crystal. Measurements conducted in the low triplet density regime, in the presence of a magnetic field, are consistently larger than those without a magnetic field; However, the two sets of measurements overlap well at high excitation densities. Dashed lines show power-law slope of 1.

value so that we present a magnetic field effect enhancement factor, defined as:

$$\text{magnetic field enhancement factor}(B) = \frac{\mathrm{PL}(B)}{\mathrm{PL}(0)}$$

where $\mathrm{PL}(B)$ is the amount of photoluminescence at a magnetic field strength B, and PL(0) is the PL strength with no applied magnetic field.

Figure 3.7 shows a spectrally resolved measurement of rubrene's PL at high excitation power. We find no changes in peak position or width as a function of magnetic field, only changes in the overall amplitude. This result means that the singlet energy levels and spectral broadening processes involved in rubrene's radiative energy pathway are unaffected by the presence of a magnetic field. We note that only triplet excitons can be affected by an applied magnetic field, so changes to the singlet fission or triplet fusion rate must come from the involvement of a state with triplet exciton character. The measurement in Fig. 3.7 shows the magnetic field enhancement factor at low magnetic field strength (up to 60 mT) is slightly less than one (as low as 0.98). This corresponds to a slight increase in fission or decrease in fusion, with magnetic field present, which is supported by observations in Refs. [62, 63]. Conversely, the enhancement factor at high magnetic field strengths (200 mT and higher) is slightly more than one (up to 1.05); we see a slight increase in the PL enhancement factor because stronger magnetic field reduces the singlet fission rate. The experiments of Ref. [61] agree qualitatively with our measurements–a slight decrease in photoluminescence yield upon application of a weak magnetic field and an increase in PL for higher magnetic field strengths. However, our enhancement of 1.05 at high powers is 5× weaker than what is reported in Ref. [61].

To investigate this discrepancy, we collected spectrally-resolved photoluminescence spectra that determine the magnetic field enhancement factor for a variety of excitation powers, excitation facets, and crystal temperatures. Because we found no changes in the spectral intensity distribution with application of a magnetic field in any of these spectra, we extracted the amplitude of each spectrum from a fit of rubrene's known spectrum as a measurement of the $\mathrm{PL}(B)$ to make presentation of the PL enhancement easier to visualize. Again, we normalized the amplitudes with the zero-field photoluminescence measurement (PL(0)) to show a magnetic field

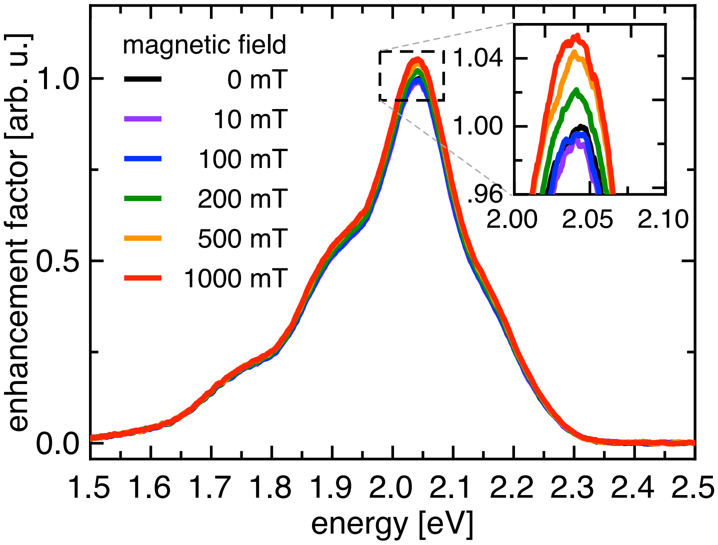

Figure 3.7: Magnetic field effect on photoluminescence spectrum in an *ab* facet of rubrene single crystal at high excitation power. The 0 mT curve peak can be seen between peaks of 10 mT and 100 mT. All curves are normalized to maximum PL emission of the 0 mT peak.

enhancement factor; we present these data in Fig. 3.8. Each point represented in Fig. 3.8 is the average of two measurements over the magnetic field range indicated by the horizontal bars.

Figure 3.8 shows the PL enhancement factor dependence on magnetic field in a variety of crystal and environmental cases. Low excitation powers (left graphs of the figure with blue plotted points, $3 \times 10^{19}\,\mathrm{cm}^{-3}\,\mathrm{s}^{-1}$ excitation density) show an enhancement factor of up to 1.2 for high magnetic fields. In contrast, high excitation powers (right side of the figure with red plotted points, $3 \times 10^{22}\,\mathrm{cm}^{-3}\,\mathrm{s}^{-1}$ excitation density) show an enhancement factor of up to 1.04. The plots of the enhancement factor in Fig. 3.8 agree well with observations in the excitation power dependence experiment (Fig. 3.6), as well as with the older measurements by Ref. [61] that used a low excitation density and found a PL enhancement of 25%. As described in the excitation-power dependence experiment, the apparent change in the PL enhancement factor stems from whether or not triplet fusion recreates singlet excitons that

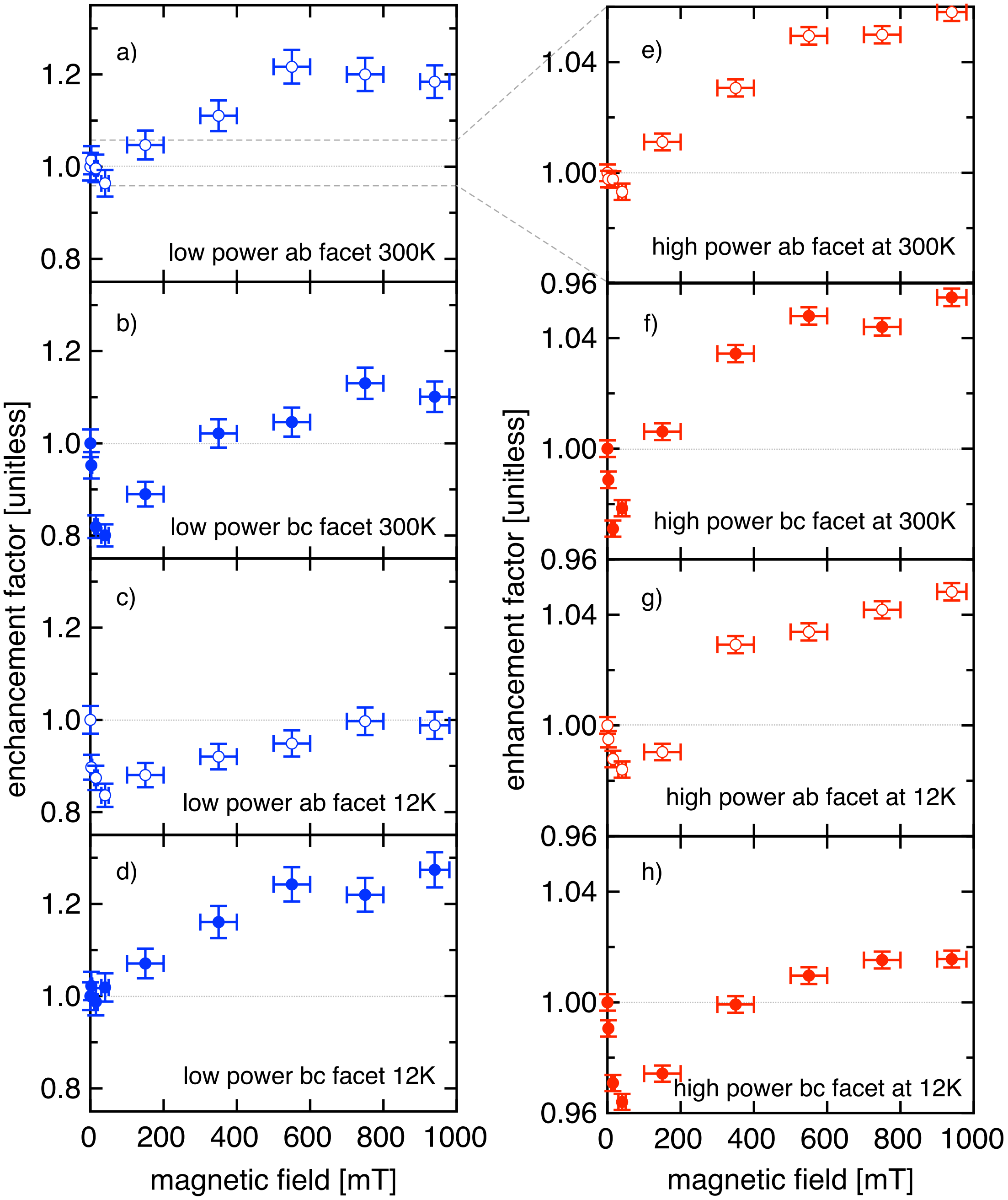

Figure 3.8: Magnetic field effect on photoluminescence yield. High excitation power (left graphs, red data) and low excitation power (right graphs, blue data) have different vertical scales reflecting a larger enhancement for low excitation powers. Nominal temperatures only.

contribute additional PL.

While the amplitude of the magnetic field enhancement factor is determined by the excitation power, the general shape of the PL dependence on magnetic field is qualitatively the same for all excitation powers: an initial decrease in PL for low magnetic field values (below 60 mT) then an increase of photoluminescence for high-magnetic field values (100 mT and above). The small-field decrease in PL is explained by Refs. [62, 63] as a slight increase in singlet fission, whereas the high-field's larger enhancement of PL is described by Ref. [61] as a larger decrease in singlet fission. The PL vs magnetic field relationship we show is similar in shape to what has been published by Rumyantesev et al. [61] for rubrene single crystals. Connecting the constant spectral intensity distribution of the PL enhancement while changing magnetic field with our description of PL changes at high and low excitation powers we see that the magnetic field's effect on singlet fission is independent of excitation density, and thus, triplet population of the sample.

The plots with open data points in Fig. 3.8 show the enhancement factor measurement is unaffected by changing the excitation polarization between the a and c axes. The main difference between the a and c axes is that there is much greater absorption and emission along the c axis than along the a axis because the c axis is parallel to the first dipole transition of the rubrene molecules. We note that resonances in the enhancement factor have been found in single crystal tetracene when varying the crystallographic orientation [64, 65], with a 30% enhancement in PL on-resonance compared to a 10% enhancement in PL off-resonance. In our setup, it was not possible to continuously change the relative orientation of the crystal and magnetic field. In the absence of such a study for rubrene, we held a consistent magnetic field orientation, parallel to the crystal's b axis, between experiments to ensure comparability between our data sets.

Finally, we tested the temperature dependence of the magnetic field enhancement. Data in the top four graphs of Fig. 3.8 were all collected at room temperature, while data in the bottom four graphs were collected at a nominal temperature of 12 K, which corresponds to a sample temperature around 225 K. We find no consistent difference or pattern in the magnitude of the PL enhancement between high and low temperatures. The complexity of these measurements has made it challenging to obtain data that are consistent between measurements that test both temperature and magnetic field effects simultaneously. Reference [61] does report a temperature dependence of the magnetic field induced PL enhancement, below the resolution of our experiment, which they attribute to a change in the singlet fission rate. They find a larger magnetic field effect at lower temperatures, which they use to determine the activation energy of rubrene.

In conclusion, we show the importance of measuring through a range of excitation powers to see the smaller magnetic PL enhancement due to a change in the fission efficiency. We report that the slight decrease in the number of excitons that undergo fission from an applied magnetic field is independent of excitation power, excitation polarization, and sample temperature.

3.3 Triplet Exciton Diffusion Measurements

Exciton diffusion in rubrene single crystals is an important part of the story of triplet excitons in the fission/fusion processes. The story begins with the initially excited singlet exciton, which undergoes singlet fission within 10 ps; this lifetime is far too short for the singlet exciton to diffuse very far. The products of singlet fission, two independent triplet excitons, each have a lifetime of $100\,\mu s$; this is 7 orders of magnitude larger than the singlet exciton lifetime providing ample time for the triplet excitons to diffuse through the crystal. One reason why the triplet exciton lifetime is so long is that the triplet exciton cannot radiatively decay; the main two decay mechanisms available to the triplet exciton are nonradiative decay (the $100\,\mu$s lifetime) and triplet fusion (whose rate is determined by triplet population density). Direct imaging experiments of the triplet exciton diffusion length are possible in rubrene because triplet excitons can diffuse through the crystal, undergo triplet fusion, and then emit a photon outside the excitation spot.

Organic molecular crystals allow for long-range diffusion of excitons. Initial estimates put diffusion lengths in molecular crystals in the range of a few micrometers

[66]. This was first directly measured in images obtained by Irkhin et al. for excitons in rubrene single crystals with the observation of a 4 μm triplet exciton diffusion length [37, 51]. Similar results were obtained more recently by Akselrod et al. and Wan et al. in tetracene [67, 68].

Triplet exciton diffusion in rubrene single crystals is anisotropic; it is only known to occur along the b crystallographic axis [37]. This is likely linked to the closely-packed arrangement of molecules, with its pi-orbital overlap, along the b crystallographic axis [40, 69]. The strong anisotropy sets up an approximately one-dimensional diffusion system where the probability of collisions between triplets is greater compared to the 3-D random walker. The singlet and triplet populations of the excitonic system were modeled by Irkhin et al. [37] using two equations that describe singlet fission and triplet fusion. The solution of these equations outside the excitation beam is an exponentially-decaying spatial distribution of triplet excitons, similar to the 1-D random walker model [37]. The random walker model is parameterized by a diffusion constant D_b and the triplet lifetime τ_T which can describe the diffusion length by $L = \sqrt{D_b \tau_T}$. It is not known what material factors are important in determining D_b and τ_T for rubrene. Recent work using proton-beam irradiation proves that defect sites can play a role in determining exciton diffusion lengths in rubrene single crystals [51], though it is not clear whether that is what determines the 4 μm length. In this section we test temperature and magnetic field effects on the triplet exciton diffusion length in rubrene single crystals to help identify the origin of the 4 μm diffusion length seen in rubrene single crystals.

We used the confocal microscope described in section 3.1 on page 30 with the imaging module to image PL with 3.6 pixels/ μm resolution. We excited singlet excitons in rubrene using a 450 nm continuous wave diode laser and used the Mitutoyo 50 × objective to create excitation spots with $1 \pm 0.1\,\mu$m FWHM. The Montana Instruments Cryostation magneto-optical module allowed us to change our sample's temperature down to a nominal temperature of 12 K and apply a magnetic field up to 1 T. We aligned the b axis of the rubrene crystals with the applied magnetic field for all experiments to enable comparison of between our experiments.

As a reference, we first present the diffusion pattern from a room temperature

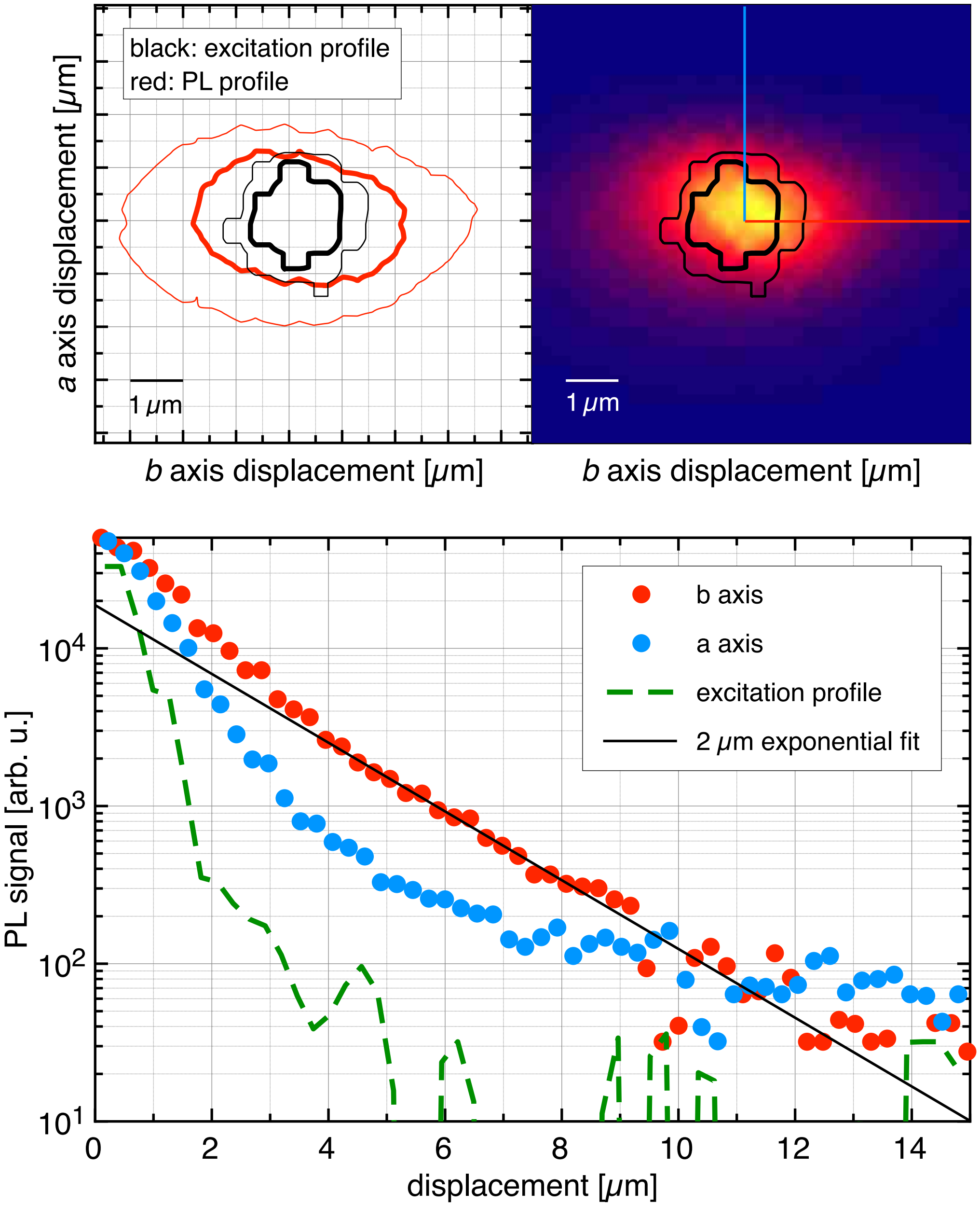

Figure 3.9: Spatially-resolved photoluminescence from rubrene single crystals at room temperature showing triplet exciton diffusion. (Top left) Black contours show the excitation beam, while red contours represent the photoluminescence profile; the thick contours represent $\frac{1}{e}$ of relative maximum value, thinner contours represent $\frac{1}{e^2}$. (Top right) plot shows PL intensity map (yellow is high intensity, blue is low intensity.) (bottom) Diffusion profiles shown by red and blue lines on intensity map.

rubrene single crystal in the top graphs of Fig. 3.9. The contours shown in the top graphs represent the $\frac{1}{e}$ (thick) and $\frac{1}{e^2}$ (thin) contours for both the excitation beam (black) and the photoluminescence (red). With these contours, it is obvious that PL is being emitted outside the excitation spot, preferentially along the b crystal axis. The top right graph plots the full PL emission distribution as an intensity map from high intensity (yellow) to low intensity (blue). The red and blue lines on the intensity map show the lines used to extract the b and a PL intensity profiles (respectively) for the bottom graph. In that plot, we see an exponential decay of photoluminescence along the b axis, as expected by the random walker model. We add that there is no exponential decay along the a axis, although it doesn't mimic the excitation profile exactly.

For small displacements from the excitation center ($< 4\,\mu$m in Fig. 3.9) there is an increasing deviation of the b axis PL profile to PL higher than the exponential decay. This deviation could be an effect of triplet fusion, but is still an area of active research (see Appx B after reading about our model of the time dynamics of rubrene in section 4.2.2). At small displacements from the excitation beam's center, there's a high triplet exciton population, so triplets are more likely to interact with each other and fuse than what is expected from the diffusion model alone. This effect scales with excitation intensity, so higher powers have larger deviations from the exponential decay [37]. Our experiments used excitation powers of 20 nW to minimize this enhancement, while still retaining a good signal to noise ratio, so that we can measure the exponential decay of photoluminescence as accurately as possible.

3.3.1 Temperature Dependence of Triplet Diffusion

Our first diffusion experiment used spatially resolved PL imaging to investigate how triplet exciton diffusion is affected by the crystal temperature. Unfortunately, we could only collect data that were strongly affected by reflections from the glass window of the cryostat, which we tried to account for during the analysis of these data. PL images collected through this window have a faint halo that is 2% of the peak PL starting at about 4 μm. This can be seen in the upper plot of Fig. 3.10 by noticing how the a axis PL signal of the upper graph levels off at 2% of the maximum PL. We worked around this halo in two ways. The first is that we used low excitation powers so that we reached the exponential decay portion of the PL profile as quickly as possible, where there is no halo. The second way we worked around the halo is by approximating this halo as angularly symmetric, so that it is equal in amplitude and position for PL measurements along the a and b axes. Using this approximation, we attempted to remove the reflection's effects and extract diffusion information by taking the ratio of the b to a PL profiles.

The top graph of Fig. 3.10 shows our b axis diffusion measurement at three different temperatures, whereas the lower graph shows the b axis/a axis ratio for three temperatures with the cryostat window, and b axis/a axis ratio at room temperature without the glass window for reference. We note that these graphs use a differently-scaled displacement-axis than other diffusion plots in this dissertation.

The direct profile measurements plotted in the top graph show a definite difference between the b and a crystal axes for all three temperatures; this shows that the experiment is sensitive to the effects of diffusion. The PL deviation at small displacements seems weaker in this experiment than in other experiments with the same power. For larger displacements, we see the region of exponential diffusion along the b axis between $2-4\,\mu$m, although the halo introduces an offset that curves our profile upwards and makes it difficult to extract the portion of the PL data that is affected by diffusion. We show an exponential decay of $2\,\mu$m, corresponding to a 4 micron diffusion length, only as a guide to the eyes. Based on the PL-spot profiles, we see no discernible change in the decay constant for these three temperatures. Again, these temperatures are the nominal temperatures given by the Cryostation, where the nominal 10 K and 150 K measurements are closer to an actual temperature around 225 K. The temperature independence in this experiment is echoed by the bottom plot, where the b/a profiles ratio is essentially identical for each temperature measured. Although these data cannot conclusively rule out any changes in diffusion length as a function of temperature, the data in Fig. 3.10 show that any possible temperature-induced change in diffusion length variation between 295 and

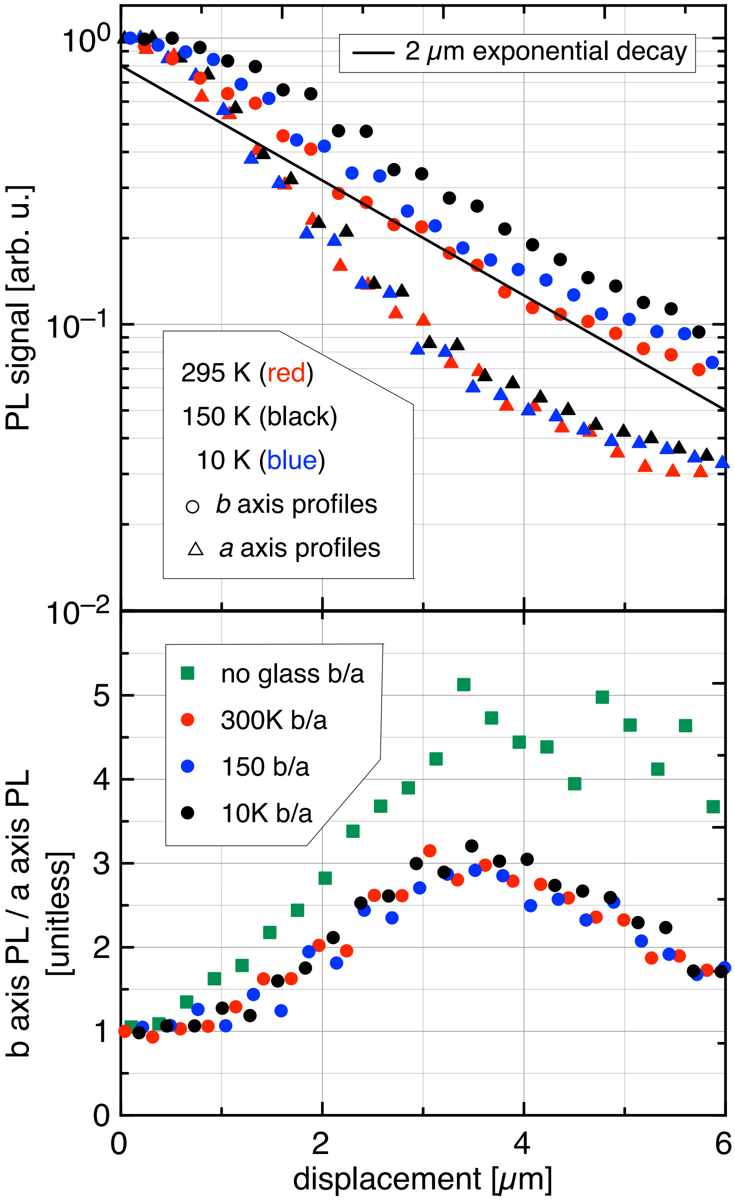

Figure 3.10: Temperature independence of exciton diffusion. Top: the circle and triangle data points respectively represent the *b* and *a* axis PL signal profiles of photoluminescence with the glass cover in place (normalized). Bottom: ratio of b-axis PL to a-axis PL plotted as a function of displacement from the excitation center. The effect of the glass is visualized by comparing the no glass measurement (squares) to the temperature-dependent plots under glass (circles). Temperatures shown are nominal temperatures given by Cryostation's platform thermometer; discussed in text.

225 K is less than 25%.

3.3.2 Magnetic Field Dependence of Triplet Diffusion

Our next experiment used spatially-resolved PL imaging to investigate how an applied magnetic field influences triplet exciton creation and diffusion. Figure 3.11 shows the effect of a magnetic field on the spatial distribution of PL. The magnetic field has two distinct effects: first, at small displacements we find a uniform increase of the PL intensity that approximately scales with the relative applied magnetic field, resulting in an increase by a factor of 1.25 between 0 mT and 1000 mT. This can be seen by the consistent order and relative spacing of the four magnetic field strengths at each displacement up to 5 μm. This uniform increase of PL with an applied magnetic field may be present through the entire profile, but is hard to see far from the excitation beam because of the low PL signal. This enhancement is made clearer by the bottom graph of Fig. 3.10, which presents the PL profile at 1000 mT divided by the PL profile at 0 mT and shows an enhancement factor of at least 1.25 through the entire profile.

In addition to the uniform enhancement of PL at short displacements, we find a slight increase in the exponential decay lifetime at larger displacements for higher magnetic field strengths. This can be seen after the initial deviation from the exponential decay, between 6 – 13 μm as a change in the slope on the log-linear plot. The grey and black exponential lines in Fig. 3.10 help show the change in exponential decay constant; the grey line is an exponential fit to the black 0 mT data with a decay constant of $2.1 \pm 0.2\,\mu$m, while the black line is an exponential fit to the red 1000 mT data with an exponential decay constant of $2.7 \pm 0.2\,\mu$m. Intermediate field strengths fill in the decay constants between those of the two magnetic field limits. The PL intensity we measure from the decay of singlet excitons is proportional to the square of the triplet density since two triplets are required for fusion [10]. From this, we calculate triplet exciton diffusion lengths of $4.0 \pm 0.4\,\mu$m without a magnetic field and $5.4 \pm 0.4\,\mu$m at 1000 mT. The bottom graph of Fig. 3.10 also shows this change in the decay constant, as an increase in the magnetic field

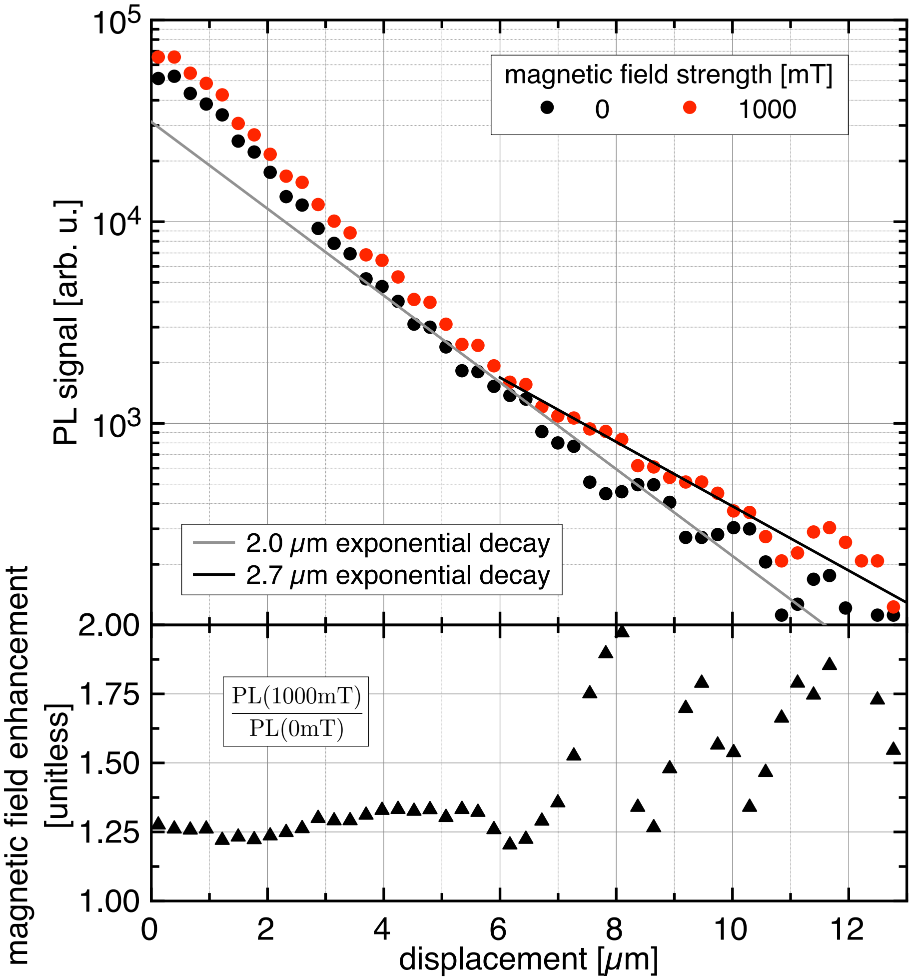

Figure 3.11: Magnetic field dependence of exciton diffusion. Top: PL signal profiles along the b axis at various applied magnetic field strengths. Exponential lines for reference. Bottom: magnetic field enhancement at each position, calculated from red 1000 mT curve and black 0 mT curve in top plot.

enhancement factor starting at 5 μm. We recognize that these data are very noisy when the exponential decay begins, which stems from the low PL signal far from the excitation center, but we see an increasing PL yield at large displacements from the excitation center with application of a magnetic field.

We attribute the increase by 25% in peak PL intensity at the center of the illumination and the modification of the diffusion length along the b-axis of the crystal to different origins.

The PL enhancement by a factor of 1.25 in the center of the illumination comes from a decreased rate of singlet fission, matching the observations presented earlier, in section 3.2.2, which show such a PL enhancement at low excitation densities. In the PL measurements described in section 3.2.2, singlet fission into independent triplets resulted in a net loss to the PL yield because the triplets would not have much chance to fuse because of the low excitation density. Similarly, singlet fission into independent triplets in the present experiment is also a net loss, despite the fact that the excitation density is larger. This loss is due to the fact that diffusion causes a net flow of independent triplets, generated via fission, away from the center of the excitation. The triplet exciton diffusion length of 4 micrometers is almost an order of magnitude larger than the beam waist of the illumination, which means that triplet excitons created in the center of the illumination have a large probability of leaving the illumination spot before they can undergo fusion. It is important to remember that we use singlet fission to mean the completed process from one singlet into two independent triplets. Only the generation of independent triplets that have low probability of interacting with each other can result in a decrease in PL quantum yield.

The second change we see in the PL profiles of Fig. 3.11 is the modification of the spatial exponential decay observed along the b-axis of the crystal with application of a magnetic field which corresponds to a change in the diffusion length. The change in the triplet exciton diffusion lengths from $4.0 \pm 0.4\,\mu$m without a magnetic field to $5.4 \pm 0.4\,\mu$m at 1000 mT can be interpreted with our diffusion model. Continuing with our 1-D diffusion model, the typical solution for any diffusion process of particles with a limited lifetime describes the diffusion length as $L_b = \sqrt{D_b \tau_T}$ where L_b is the triplet diffusion length, D_b is the diffusivity of triplet excitons, and τ_T is the triplet lifetime. This means that the applied magnetic field increases either the diffusivity, or the triplet exciton lifetime. An increase in the diffusivity means that the exciton transport mechanism of rubrene is changing with the application of a magnetic field to make diffusion more efficient; this is different from an increase in the triplet exciton lifetime, which could be a change to the triplet exciton state or its lifetime. We are unable to disentangle these two possibilities with this experiment.

The observed changes in the diffusion length have another significance. Irkhin et al. [51] contemplate the possibility that the triplet lifetime in nominally pristine rubrene could be determined by an intrinsic defect density. This would be consistent with the 4 μm diffusion length being found in numerous rubrene single crystals and observations of a decreased diffusion rate when introducing defect sites [51]. Our observation of a changing diffusion length complicates the idea of a defect-limited intrinsic diffusion length because the applied magnetic field would then have to alter the triplet's interaction with these intrinsic defects to show a change in decay length which we do not know to be true.

To reiterate, we confirmed that an applied magnetic field reduces the singlet fission rate in rubrene, and we have shown that a magnetic field increases the triplet diffusion length from $4.0 \pm 0.4\,\mu$m without a magnetic field to $5.4 \pm 0.4\,\mu$m at 1000 mT.

In summary of these two subsections on triplet diffusion, we have shown that an applied magnetic field has two effects: reducing the singlet fission rate, which results in an increase of PL by up to a factor of 1.25, and changing the triplet exciton diffusion length from $4 \pm 0.4\,\mu$m with no magnetic field to $5.7 \pm 0.4\,\mu$m at 1000 mT. In contrast, we found no changes in the PL diffusion pattern as a function of temperature within our setup's temperature capabilities and measurement sensitivity.

3.4 Steady-State Photoluminescence Results

To summarize this chapter, we report a reproducible increase in PL due to the deactivation of singlet fission when cooling rubrene. With the exception of a small 2.1 eV band appearing at low temperatures in 'altered' rubrene crystals, we report no changes in the intensity distribution of the PL spectrum when adjusting the sample temperature or applying a magnetic field. We've found that a magnetic field applied to rubrene enhances the PL yield, and attribute this to a reduction in the singlet fission rate of up to 20% at 1000 mT. We confirmed this observation with both low-excitation density studies, and localized-excitation studies with triplet exciton diffusion. We have determined that this enhancement is present at all excitation densities, although the effect at high excitation densities is smaller due to contributions from triplets that undergo fusion.

In the second part of this chapter we looked at changes to the triplet exciton diffusion length when cooling rubrene single crystals. We saw that changes are limited to less than 25%. However, we report in the triplet exciton diffusion length in the presence of a 1000 mT magnetic field to be 5.4 ± 0.4 μm, an increase of 25% compared to measurements with no field.

Our work fills in several gaps in the literature we have come across. First, we add to the available spectral measurements by documenting temperature and magnetic field changes using 'pristine' rubrene crystals that show no changes in spectral intensity distribution. This is in contrast to measurements that use 'altered' rubrene crystals where there are extra bands in the spectrum. We confirm literature results that show a decrease in singlet fission with the application of a magnetic field at low excitation density, and extend the measurements to higher excitation densities which can be explained by accounting for triplet fusion effects on PL. Finally, the change in triplet exciton diffusion we report with an applied magnetic field challenges the idea that the diffusion length of triplet excitons in rubrene is determined by triplet interactions with an intrinsic density of defects sites.

Chapter 4

Time Dynamics of Rubrene Photoluminescence

One of the easiest ways to learn about energetic pathways in a material is to introduce a lot of energy, then observe how the that energy dissipates in the material. If radiative emission is an allowed energy pathway, measuring the time dynamics of the material's photoluminescence gives insight into how energy is transformed and dissipated over time.

Since singlet fission and triplet fusion directly change the number of excitons that radiatively decay in rubrene, we can obtain information about these physical processes by observing how the amount of energy that is being converted to light changes as a function of time. To do this, we measure the time dynamics of photoluminescence from rubrene single crystals; we also study amorphous rubrene to provide a reference where these excitonic processes play a relatively small role.

We analyze the time dependence of the photoluminescence on a nanosecond and sub-nanosecond time scale using a femtosecond laser pulse to excite excitons in our sample and a time-correlated single photon counting apparatus to measure the PL. This apparatus measures the amount of time between an excitation laser pulse and the detection of a photoluminescence photon from the sample. Counting this time through tens of millions of laser pulses creates a complete data set that describes the

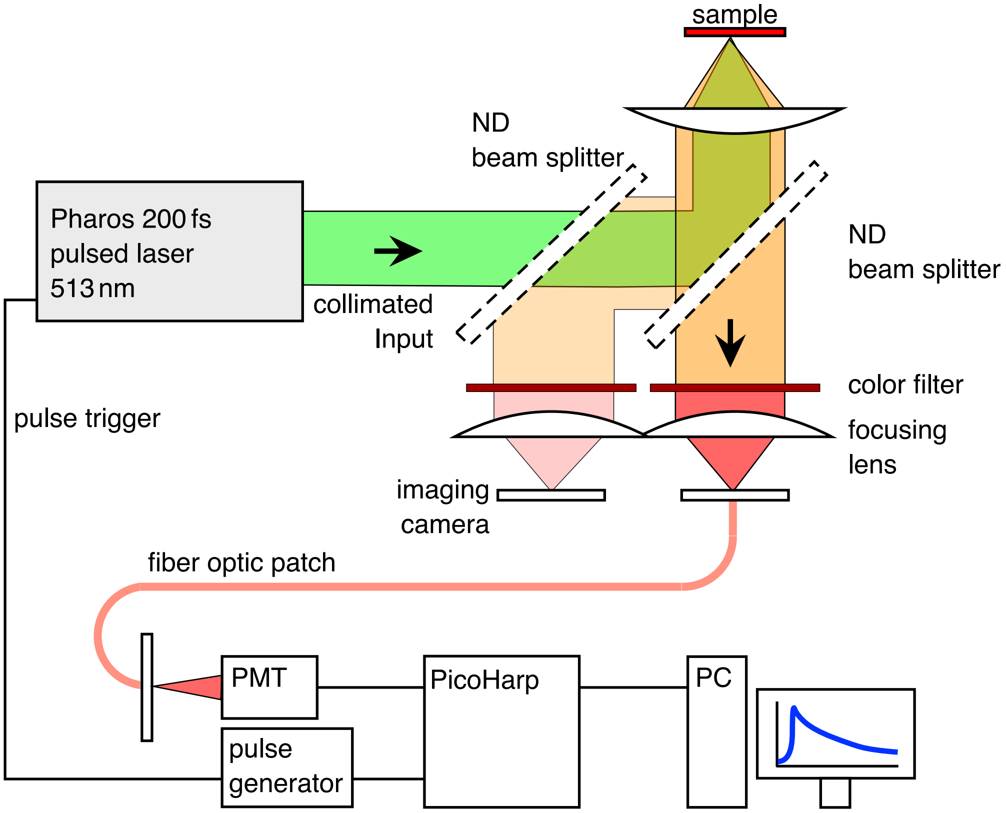

Figure 4.1: Experimental setup used for time-correlated single photon counting measurements.

time evolution of the sample's PL. By analyzing the PL time dynamics, we can use our knowledge of exciton decay lifetimes and species conversions to draw conclusions about the exciton species that emitted the photons we measured.

We analyze this PL time dynamics, using the fact that the time evolution of photoluminescence will correspond to the time evolution of the radiative excitonic species created either by the initial pulsed illumination, or by fusion of triplet excitons that were created by fission of a singlet exciton.

4.1 Experimental Details

Time-correlated single photon counting for this study was done using a Light Conversion Ltd. Pharos laser emitting 190 femtosecond pulses at the frequency-doubled wavelength of 512 nm (2.41 eV) with an adjustable repetition rate up to 200 kHz. These laser pulses were directed into a confocal microscope and focused onto a rubrene sample, as depicted in Fig. 4.1. Photoluminescence emitted by our sample was collected through the microscope where we filtered out the excitation beam using a 550 nm long pass filter. This allowed the collection of only rubrene's photoluminescence, which peaks at 610 nm for an *ab* facet. The photoluminescence was measured using a Micro Photon Devices PDM series photon counting detector with a 50 μm active area diameter and a dark count rate of less than 50 cps. This signal is carried to a PicoQuant PicoHarp 300, which is triggered by the laser sync line via 4 ns square-wave with a 0.5 V-amplitude created by a Stanford Pulse Generator. We obtained time dynamics measurements from $4\,\text{ps} - 5\,\mu\text{s}$ by combining two data acquisitions, one using 4 ps time bins and one using 512 ps time bins; each using up to 2^{16} bins. We then combined these acquisitions into a single data set that can be analyzed with appropriate resolution from the instrument's lower measurement limit of 4 ps to the beginning of the next laser pulse at 5 μs.

If multiple photons arrive at the detector within the same laser pulse, only the first is measured, which will weight the data towards earlier times and skew the time dynamics at later times; this is known as a pileup error [70]. To ensure that we do not introduce errors from the timing electronics of the PicoHarp, we adjusted the strength of PL before our PDM detecter so that only one photon would be counted for each cycle of the laser. This was done by using ND filters before the photodetector to keep the PL count rate at less than 5% of the signal sync rate of 200kHz.

Excitation density at the surface of the sample was calculated from measurements of beam power and beam diameter at the sample. We used a Newport silicon power meter to measure the average power of our free beam, then accounted for power lost through the confocal setup between the free beam and the sample. The average number of singlet excitations at the surface of the crystal created by one laser pulse, S_{1Pulse} was then calculated using the equation

$$S_{1Pulse} = \frac{S_0}{f} = \left(P_L \frac{\lambda}{hc}\frac{1}{f}\right)\left(\frac{4\ln(2)}{\pi \mathrm{FWHM}^2}\right)\left(\frac{1}{d}\right), \tag{4.1}$$

which we derive in appendix A on page 104. P_L is the power of the laser with wavelength λ, f is the repetition rate of the pulsed laser, the factor of $4\ln(2)$ is introduced to relate the Gaussian geometry to the full width at half maximum (FWHM) of the beam intensity, and d is the absorption length of rubrene (which has a value of $4\,\mu$m along the b axis of rubrene at 513 nm [38]). Equation 4.1 is presented as three distinct fractions to highlight that the output of the laser, the spatial geometry of the laser pulse from the microscope's optics, and the crystal's absorption properties (respectively); all influence the total excitation density.

For this study we collect photoluminescence from the *ab* facet of rubrene single crystals (unless otherwise specified). Preliminary experiments showed no significant differences in the time dynamics observed with different excitation axes when accounting for different excitation densities due to anisotropic absorption coefficients. For comparability, all measurements presented in this work were measured with excitation polarization parallel to the *b* axis. We present data on both 'intrinsic' and 'altered' rubrene crystals (the meanings of which are discussed in the background chapter on page 20). A particular aspect of interest is the time evolution of the 1.9 eV emission band in 'altered' rubrene. All samples used were carefully chosen to be free of surface defects in order to avoid encountering PL artifacts, also described in the background information chapter on page 19.

4.2 Rubrene Single Crystal Studies

Exciton fission and fusion processes in rubrene single crystals can be studied with optical experimental methods which up to now have focused on a specific time scale. Short time scale experiments (shorter than 0.1 ns [30, 44, 48, 71]) study the radiative emission and fission of singlet excitons, while long time scales (longer than 1 μs [45, 47]) study triplet exciton lifetimes and the recombination of triplet excitons. We find that literature sources between these two limits, on the nanosecond timescale, draw conclusions about the system without considering the full effect that triplet excitons can have on the PL time dynamics they report.

The nanosecond time scale of PL time dynamics in rubrene has been studied by two research groups [12, 24, 30]. Both groups observed highly non-exponential decay curves, and fit nanosecond-scale exponential time constants by looking at only part of their data sets and their linear tangents in semi-log plots.

The first group fit an exponential decay of photoluminescence with a lifetime of 1.8 ns. They also report that they do not observe this decay in samples measured under vacuum at photon energies between 2 eV and 2.38 eV (which excludes PL from the 1.9 eV emission band [30]). They assign their 1.8 ns decay to fluorescence from an oxidized form of rubrene, based on research which suggests the 1.9 eV band of rubrene is explained by an oxidation effect [42, 43]. Additionally, the photoluminescence spectrum of the crystal used in in Ref. [30] is an extreme example of an 'altered' rubrene crystal and has little resemblance to the spectrum known for intrinsic rubrene [38]. We recognize from the spectrum they present that when they filter the 1.9 eV band from their sample they remove most of the PL emitted by their sample. For this reason, and without data reporting the spectrally resolved time dynamics, we treat their 1.8 ns decay time as a report of the time dynamics of 'altered' rubrene. Additionally, the use of an 80 MHz pulsed laser in Ref. [30] allows time for less than 0.02% of triplet excitons to relax before the next pulse which implies that their experiments must have a very large steady state triplet population. The effect of such a large background triplet population cannot be neglected when triplet excitons contribute to PL.

The second group reporting on PL time dynamics in the literature, with publications by Piland et al. [12] and Burdett et al. [24], also present data on the nanosecond time scale. Piland et al. use an exponential decay of 2.22 ns in describing the fluorescence decay of their amorphous sample at room temperature, although the data they present has a steadily-curving decay through the nanosecond timescale. They find that the 2.2 ns lifetime increases for lower temperatures

[12]. However, Piland et al. use a sample they describe as 'amorphous' even though the time dynamics data they present show evidence that singlet fission may still be occurring which is a sign of the presence of crystalline regions, probably on the nanometer scale (see section 4.3 on page 92 for a discussion of amorphous rubrene).

In this work, we will perform an investigation of the PL dynamics on the 0.1 to 100 ns time scale and for different excitation densities, which account for effects introduced by triplet excitons. In particular, we know from our previous measurements that excitation density must play a very important role in modifying PL kinetics on the nanosecond scale and shorter. We also make sure that the repetition rate of the laser is low enough that we minimize the accumulation of long-lived triplet exciton states between pulses, and take them into account when analyzing the data. In addition, we use single crystals that allow for triplet exciton diffusion in the crystal. Observable effects of triplet excitons depend on the triplet exciton density; we test these effects by varying the excitation power to create more singlet excitons which will undergo singlet fission to create more triplet excitons.

4.2.1 Results & Discussion

The power-dependence of the time dynamics of photoluminescence from a 'pristine' rubrene single crystal is shown in Fig. 4.2. Each color in Fig. 4.2 represents a different excitation power, spaced with factors of ~ 2. The figure presents data through the transition region from low to high triplet population densities. We used a 'pristine' crystal for this measurement which shows very little contribution from the 1.9 eV emission band (see Fig.4.3 and the discussion on types of rubrene in section 2.2.2 on page 20).

PL time dynamic plots in this dissertation can be analyzed by keeping in mind that they represent the decay of states that are able to emit PL. The radiative lifetime of singlet states in rubrene molecules is 16 ns [45, 46], which sets a limit to how long we can observe initially-excited singlets. However, singlet fission occurs on a timescale much shorter than the radiative decay lifetime, with a reported singlet lifetime on the order of 10 ps [30, 48, 49], which means that our measurements only

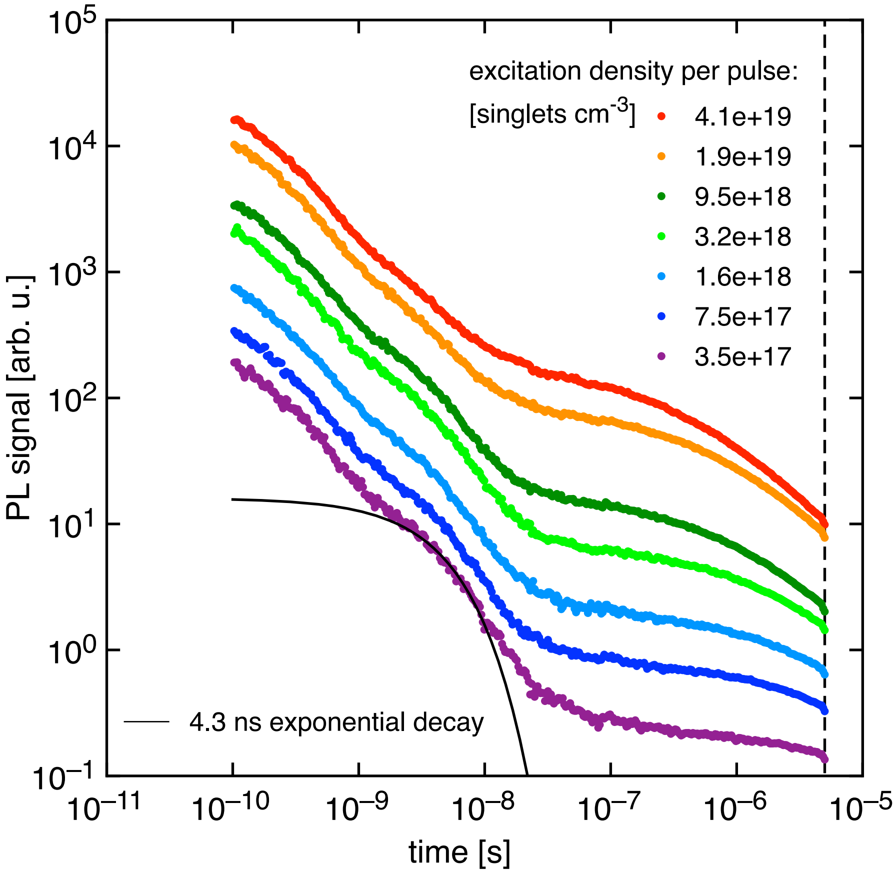

Figure 4.2: Measurement of time-correlated single photon counting of a 'pristine' rubrene single crystal photoluminescence at multiple excitation powers. The dashed line on the right highlights the position of the next pulse in the 200 kHz pulse train. (color online, order preserved)

capture PL from the initially photo excited singlets in a first transient that is limited by the time resolution of the apparatus.

The initial decay of the PL time dynamics, up to $\sim 3 \times 10^{-10}$, contains information about the initial, pure singlet state decay, although timescales shorter than $\sim 500\,\text{ps}$ overlap with our Picoharp's instrument response which alters the shape of the measured time dynamics and complicates a detailed analysis. However, the Picoharp's instrument response does not change as a function of our sample's excitation power, and we can still assign the integral of the detected signal during the

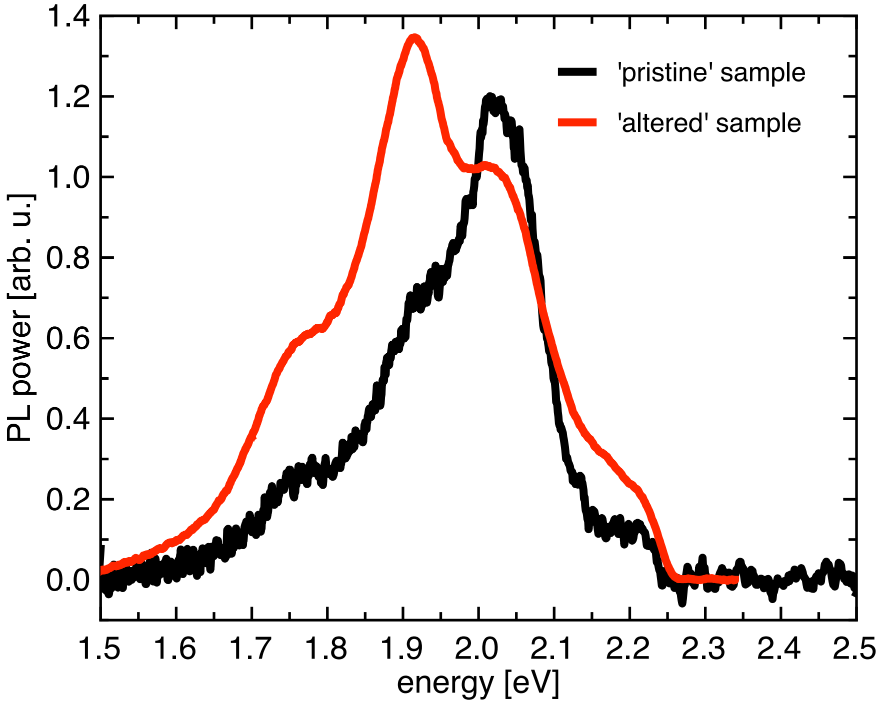

Figure 4.3: Comparison of PL spectra of our 'altered' and 'pristine' rubrene single crystals to published data on emission from b-polarized emission ('intrinsic'). Normalized to 2.03 eV height.

first few 100 ps to the PL arising from the initially excited singlet states before they undergo fission. Our time dynamics measurements show a fast initial decay of PL at times shorter than 1 ns that does not change shape as a function of power.

In Fig. 4.2 we see that PL curves representing measurements performed at high excitation densities begin to bend downwards towards the end of the measured range (at 5 μs), approaching a power-law decay (depicted by a straight line on log-log plot), while the slope of the curves representing measurements at low excitation powers appear to decrease at these times. These observations are both explained well by differences in triplet exciton densities between the curves. The beginning of the power-law decay at high excitation densities appears because the triplet fusion rate is dependent on the square of the triplet density [47]. The less steep region at low excitation densities is then explained by a reduced amount of triplets which are less

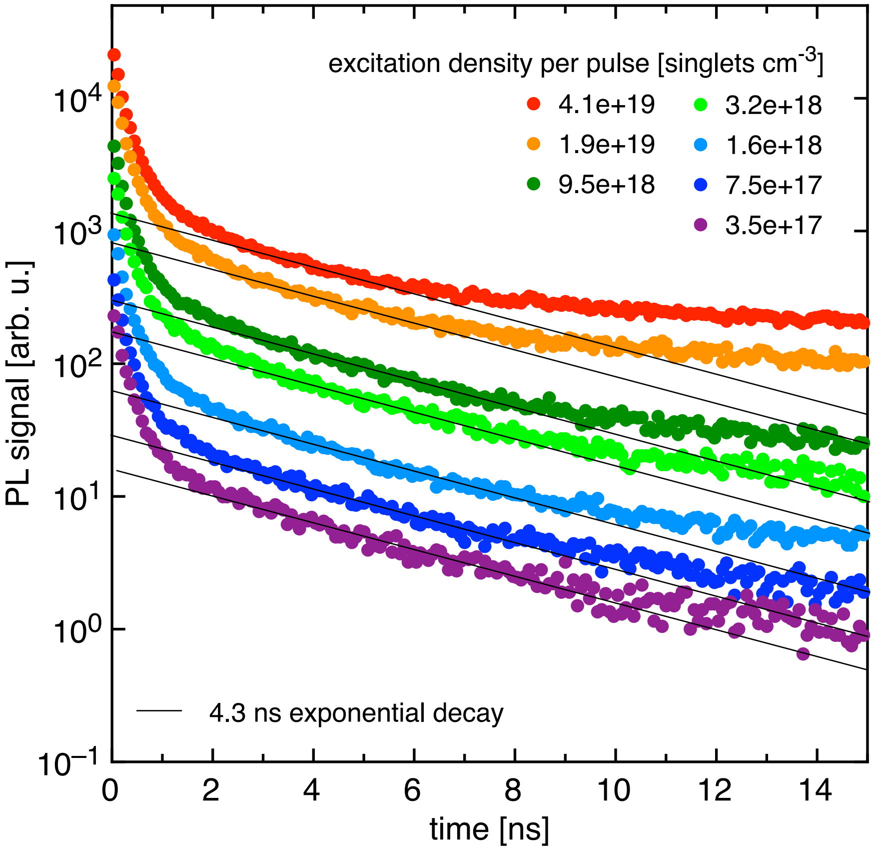

Figure 4.4: Excitation power dependence of the 4.3 ns decay of photoluminescence. The lowest black line is a monoexponential fit of the 3.5e+17 singlets cm^{-3} data between 2 and 10 ns. Other black lines are drawn parallel for reference only (color online).

likely to undergo fusion. For a given laser power, the slope of the line in the PL time dynamics measurement at the end of this plot is an indicator of the triplet exciton density of the system before the next laser pulse arrives.

We find these short and long timescales are well-described by the current understanding of singlet fission and triplet fusion. However, between these times the photoluminescence shows an additional feature that resembles an exponential decay. This exponential decay appears as a bump through the nanosecond decade on the log-log scale in Fig. 4.2 which appears at lower excitation powers. This decay is more easily visualized in Fig. 4.4 on a log-linear scale to showcase the exponential nature of the low power data between 2 and 12 ns and its disappearance when using higher excitation powers. At the lowest excitation density, we find an exponential decay with a decay time constant of 4.3 ± 0.5 ns. We note that the black lines in this figure represent a 4.3 ns decay, and are offset to the other plots as a a visual aid. The 4.3 ns exponential decay was observed in several crystals and with the light polarized along both a and b crystal axes. We dedicate a majority of the remainder of this dissertation to characterizing and identifying the origin of this decay.

We start by comparing our results with those found in existing literature. The general shape of the time dynamics from our time-resolved photoluminescence measurements are similar to those shown by Ma et al. [30], Piland et al. [12], and Burdett et al [24] at specific powers. Our high excitation density data plots are similar in shape to curves published by Ma et al., though we measure an exponential decay time that is longer than their reported value of 1.8 ns. We note that their excitation density of 1-2% of molecules in the crystal corresponds to an excitation density of 1.4×10^{19} excitations/cm^3; this is comparable to the highest excitation densities in our data set. An important experimental detail they report is that they use an 80 MHz laser system for their time-resolved photoluminescence measurements, which affords the excitons only 12.5 ns between pulses and implies a very large triplet accumulation over many pulses in their experiment. This leads to deformations of the nanosecond scale PL response at singlet excitation populations lower than what is expected from the system if it had relaxed completely before excitation.

In contrast to Ma et al.'s high triplet population density, Piland et al.'s use a 40 kHz laser with which they find an exponential decay time of 2.22 ns. They test the excitation power-dependence of PL between 1.8×10^{15} and 19×10^{15} excitations μm^{-3}, but find no changes in the shape of the time dynamics. This is interesting for two reasons: First, they do not see any changes in the visibility of their nanosecond-lifetime exponential decay as we have show above, and second, we find that their data does not show any PL modifications due to effects of triplet fusion in their system. Piland et al. probably do not observe changes in the time dependence of their time dynamics with different excitation densities because of the fragmented nature of their sample. Their sample's molecular arrangement limits triplet diffusion so that all triplets could only recombine with their sibling triplet (created from the same singlet exciton); triplet fusion then becomes independent of triplet density because the triplets are already neighbors. In addition, even if triplet diffusion was normal, their excitation densities remain in the regime with little triplet fusion, which leads to an independence from the excitation density.

A 2008 measurement of PL time dynamics in rubrene single crystals by Mamedov and Becker published in Ref. [45] has a 4 ns exponential decay that matches the results we present here.

We conclude that most of the existing PL dynamics results presented in the literature have been obtained under circumstances that affect the triplet excitons in the system and have mostly been taken in 'altered' rubrene which includes the 4.3 ns exponential decay. We now proceed to discuss the possible origins of this decay.

In the background section 2.1.2 on page 8, we introduced the two processes involved in singlet fission: state mixing (which creates the intermediate state exciton) and triplet-pair dissociation (which creates two independent excitons.) Within 10 ps after excitation, most singlet excitons undergo the state mixing process and are transformed into the intermediate state exciton. The intermediate state is a superposition of the singlet exciton and correlated pair of triplet excitons, giving it both singlet and triplet character simultaneously. Because it has singlet character, the intermediate state may radiatively decay to contribute to the photoluminescence of the system; however, if the correlated pair of triplet excitons dissociates first, then no photoluminescence is emitted by those excitons unless they can recreate the intermediate state through triplet fusion. We assign the 4.3 ns decay to the intermediate state exciton's lifetime determined by triplet-pair dissociation.To test our assignment of the 4.3 ns exponential decay to the intermediate state, we use different types of rubrene samples, spectrally filter the emitted PL, apply a magnetic field while observing the exponential decay.

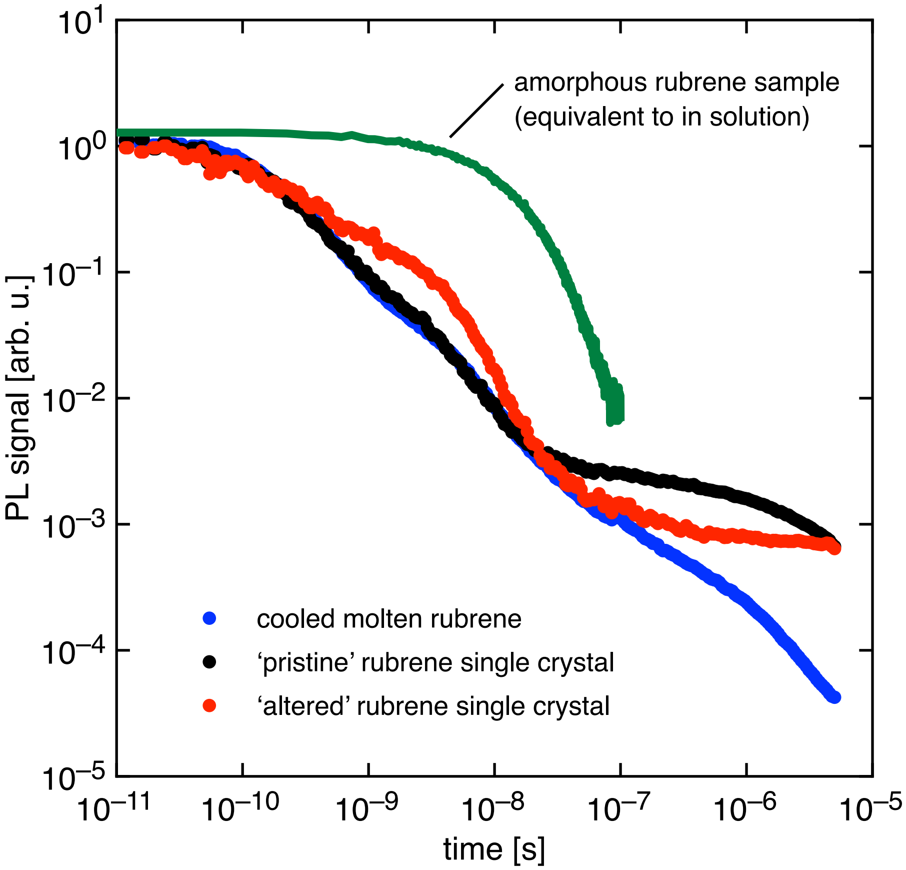

Figure 4.5: Time-dynamics measurement of photoluminescence from four types of rubrene. The 'altered' type of rubrene shows the 4.3 ns decay very clearly, while the 'pristine' and molten rubrene samples show only slight hints of it. All curves are normalized to initial PL, and the 'pristine' and 'altered' curves meeting at 10^{-5} was not forced by data manipulation.

Types of Rubrene

We examined 4 types of rubrene: molecular-beam deposited amorphous film, molten film, 'pristine' single crystal, and 'altered' single crystal. The PL time dynamics of these samples are shown in Fig. 4.5. We used the same excitation powers of 10^{18} excitations cm^{-3} for the molten film, 'pristine', and 'altered' rubrene samples. Each curve is normalized to the peak PL emission to make comparisons easier. A detailed analysis of the amorphous rubrene film is presented at the end of this chapter on page 92, but for now we simply present it as a film with minimal intermolecular interactions; singlet fission is essentially turned off, and the time dynamics show the singlet exciton's radiative decay.

The molten sample was created by melting rubrene between two glass microscope slides, then allowing it to cool (details of this process are discussed at the end of chapter 2). This sample has three nucleation sites from which molecules have approximately arranged themselves with their molecular L axis oriented radially. This was determined by placing the sample over a light source in-between crossed polarizers to see absorption effects of the radial orientation of rubrene molecules around the nucleation sites with centimeter-scale domains. The molecular ordering in this sample means that singlet fission can occur, as confirmed by the time dynamics which overlaps that of the 'pristine' single crystal PL dynamics, including a slight 4.3 ns decay, up to 10 ns. After that time, the PL continues to decrease and may approach a power law regime of triplet fusion with with a power-law exponent of 1. We interpret this measurement as identifying a sample that allows for singlet fission and triplet fusion (which is required to see PL after the singlet lifetime), but the triplets are likely confined by the irregular arrangement of molecules. Without triplet diffusion, triplet fusion is not dependent on the square of the triplet population density. These trapped triplets are likely to undergo triplet fusion only with their sibling triplet excited in the same nanocrystal. Because of the similarity of triplet exciton effects in the PL time dynamics data, we propose that our molten sample as similar to the evaporative spin-coated film created by Piland et al. [12], except we have much larger crystalline domains.

The 'altered' rubrene crystal is characterized by a strong 1.9 eV emission band, as seen by comparing the emission band in Fig. 4.3 for the 'altered' and 'pristine' samples where the curves are normalized to the 2.0 eV signal height. The origin of the enhanced 1.9 eV emission band in 'altered' rubrene single crystals is still debated in the literature. Many sources assign it to the oxidation of rubrene molecules [42, 43], though changes in the crystal lattice of rubrene have also been proposed [41] as the cause. Regardless of which is correct, both of these explanations suggest g a distribution of defect sites throughout the crystal.

The black and red curves in Fig. 4.5 represent the time dynamics of ‘pristine’ and ‘altered’ rubrene single crystals, respectively. There is a large enhancement of PL through the nanosecond timescale for the ‘altered’ rubrene measurement, which increases the contrast of the 4.3 ns exponential decay with respect to the ‘pristine’ crystal’s PL. At time scales approaching 1 μs, the delayed PL emission from triplet fusion is diminished in ‘altered’ rubrene and doesn’t yet show the power-law decay. This is indicative of a lower triplet exciton population in the ‘altered’ rubrene sample, possibly because the increase in PL at 4.3 ns decreased the concentration of available excitons.

The 1.9 eV band can dominate the emission spectrum of ‘altered’ crystals, and can be in many cases even stronger than the intrinsic rubrene emission in some crystals. It has been argued [31] that diffusing triplet excitons can interact with defect states, undergoing fusion at a defect site with lower excitation energy. As the triplets at defect sites radiatively recombine, they emit 1.9 eV photons [31, 51]. In this way, even a low concentration of defect states can make a dominant contribution to the PL in rubrene because the sites harvest the energy from the dominant triplet population created by fission.

References [31, 51] propose a model for triplet exciton diffusion where the triplet state excitons diffuse through the crystal and interact with defect sites. Applying that idea to our measurements in altered rubrene, the 1.9 eV emission then may correspond to radiation of excitons with an altered singlet component. Our experiments on triplet exciton diffusion have verified that triplets diffuse up to 4 μm in their lifetime, allowing them to interact with over 10,000 molecular sites. With a defect density of less than 1%, the altered PL would be extremely visible since only 1 in more than 10,000 molecules would need to be a defect. A triplet exciton would have to become trapped at a defect site until another occupies a neighboring molecule and the pair undergoes triplet fusion to recreate the intermediate state. The energy of the intermediate state is slightly altered by the trapped triplet exciton’s energy state at the defect site, so it radiates PL at 1.9 eV instead of its first electronic transition at 2.2 eV. However, this mechanism involving independent triplet excitons

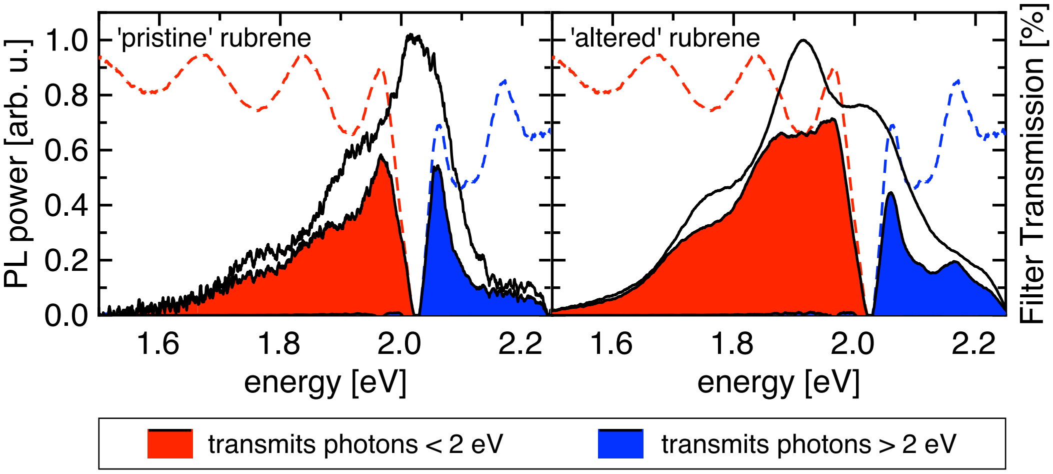

Figure 4.6: Plots showing the light transmitted through each of the filters for measurements in 'altered' and 'pristine' rubrene. Dashed lines show filter transmissions. Each of these graphs is normalized to the peak of its unfiltered emission spectrum (black spectrum). A comparison of the relative heights of bands between 'altered' and 'pristine' rubrene is seen in Fig. 4.3.

being trapped at a defect site, while it can explain the dominance of the 1.9 eV PL band, cannot explain the 4.3 ns decay we observed. This is because triplet excitons live a long time and would keep getting trapped at defect sites throughout their lifetime.

Next, we spectrally filter the PL of rubrene to isolate the effects of the 1.9 eV emission band.

In the absence of a streak camera or other fast spectroscopy methods, we used dichroic filters in our time dynamics setup to extract information about the time dynamics of the 1.9 eV emission band. To do this, we use a filter that either transmits the 1.9 eV band, or blocks it. It's important to remember that transmitting the 1.9 eV band also transmits a significant portion of the intrinsic rubrene PL, especially in the 'pristine' rubrene sample. Figure 4.6 shows the transmitted light that is measured by our photodetector using each of our dichroic filters (filter transmissions are shown by the dashed lines). The red spectral regions are observed using a filter which transmits PL with energies lower than 2.0 eV, including the 1.9 eV band. The

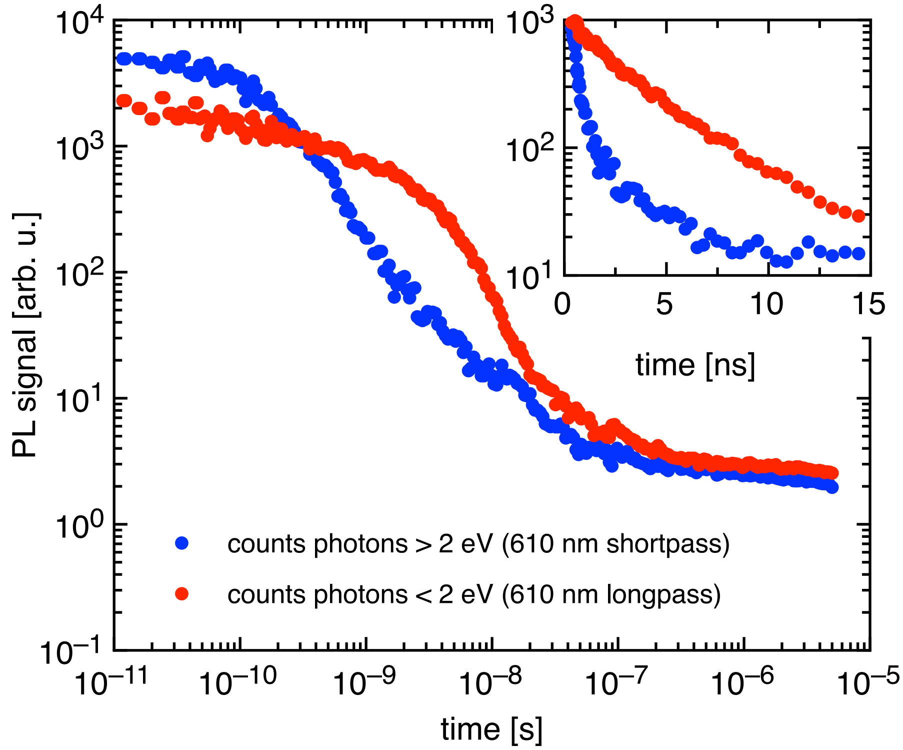

Figure 4.7: PL time-dynamics measurement of 'altered' rubrene single crystal with spectral filters inserted before PL detection. The 4.3 ns decay is enhanced with the inclusion of the 1.9 eV emission band. The inset shows the same data on a log-linear scale to highlight the exponential nature of the decay associated with the 1.9 eV emission band.

spectral regions in blue use a filter that transmits PL with energies higher than 2.0 eV, blocking the 1.9 eV band. We use these filtered spectra to learn about the evolution of the 1.9 eV band.

Figure 4.7 shows how spectral filtering of the PL from an 'altered' rubrene crystal creates two different time dynamics. The blue plot, representing counted photons with energies greater than 2.0 eV corresponds to the intrinsic PL spectrum of rubrene; it includes no effects of the 1.9 eV emission band. However, the red curve, corresponding to energies smaller than 2.03 eV, includes photoluminescence from both the pristine rubrene spectrum and the 1.9 eV emission band. These plots were

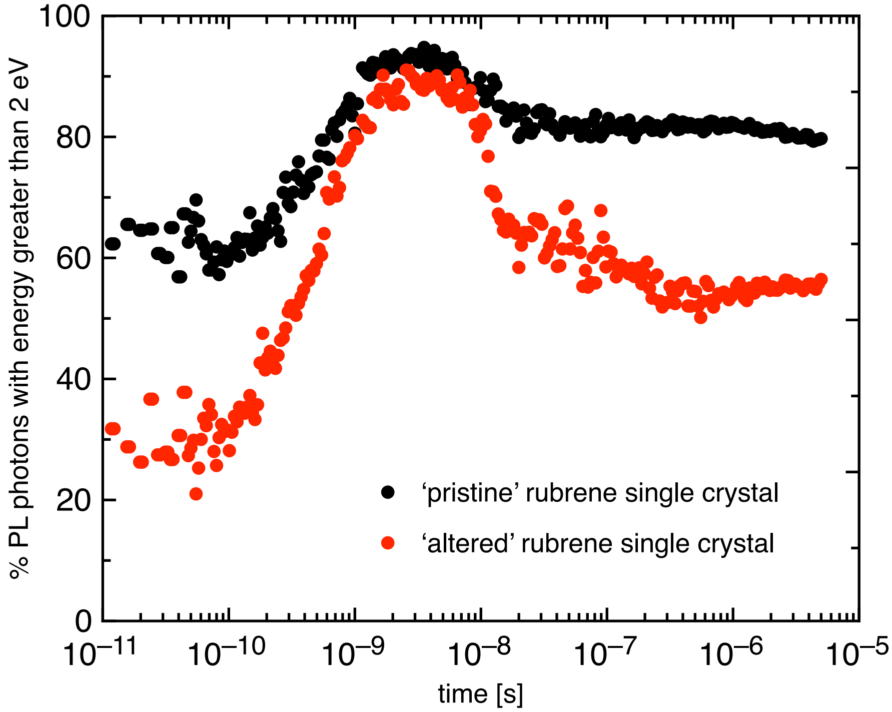

Figure 4.8: Percentage of light transmitted by the spectral filter (that includes the 1.9 eV band emission) compared to the total PL emitted at each time.

created by scaling each spectral filter's transmission to the PL spectrum we measured in a steady-state PL experiment; because of this, the relative scaling between the two curves is directly comparable.

In Figure 4.7, we see that the intrinsic PL is initially the dominant source of PL. Its time dynamics show no exponential decay in the nanosecond scale until the triplet exciton population come to an equilibrium state at longer time scales (around 1 μs). The emission containing the 1.9 eV band, on the other hand, is weaker initially, but then comes to dominate the decay with a clear 4.3 ns exponential component. We see this same pattern, where the 4.3 ns decay is enhanced when measuring only the lower energy photons, in the PL time dynamics of 'pristine' rubrene crystals, however, the contrast of the 4.3 ns decay in 'pristine' rubene is not as large as in 'altered' rubrene.

The data in Fig. 4.7, and similar data measured in an 'intrinsic' crystal, imply that the 1.9 eV band increases with time relative to the intrinsic rubrene spectrum after the initial excitation. Fig. 4.8 shows the percentage of total light detected from photons with energies less than 1.9 eV at each time:

$$\% = \frac{\text{PL counts(spectrum including 1.9 eV band)}}{\text{PL counts(total)}}$$

for both 'intrinsic' and an 'altered' single crystals. If all the spectral bands emitted by these rubrene samples had the same time dynamics, both curves in this plot would show a constant value for all times. The 'intrinsic' rubrene plot only shows a 20% change in the ratio with maximum centered at 4.3 ns, while the 'altered' rubrene plot shows a much larger change in the ratio. Because much of 'altered' rubrene's PL comes from the 1.9 eV band, we see a maximum at 4.3 ns. Additionally, both percentages of low photon energy from 'intrinsic' and of 'altered' rubrene are larger after the 4.3 ns decay than they were initially (seen by comparing PL at 10^{-7} vs. 10^{-10}). From these facts, we draw the conclusion that the emissive state responsible for the 1.9 eV band is not directly excited by the laser pulse. This is consistent with a triplet exciton diffusion model where the excitons require time to reach the impurities that cause the 1.9 eV emission.

Since triplet excitons are responsible for most diffusion effects, we worked to learn more about the excitation process responsible for the 4.3 ns decay's excitation mechanism by measuring changes in the PL it emits with the application of a magnetic field.

We measure the PL time dynamics with an applied magnetic field at both high and low excitation powers; knowing that magnetic field effects are small we chose to use an 'altered rubrene single crystal here to maximize the changes from the 4.3 ns exponential decay's PL. We measured the PL time dynamics with the magnetic field parallel to each of the a, b, and c crystal axis and note no significant change in the magnetic field effect between crystallographic orientations on the nanosecond time-scale. The top graph of Fig. 4.9 shows our measurement of the PL dynamics with and without a magnetic field of a few hundred mT parallel to the b axis. It shows a clear enhancement with magnetic field of the PL decay we attribute to the

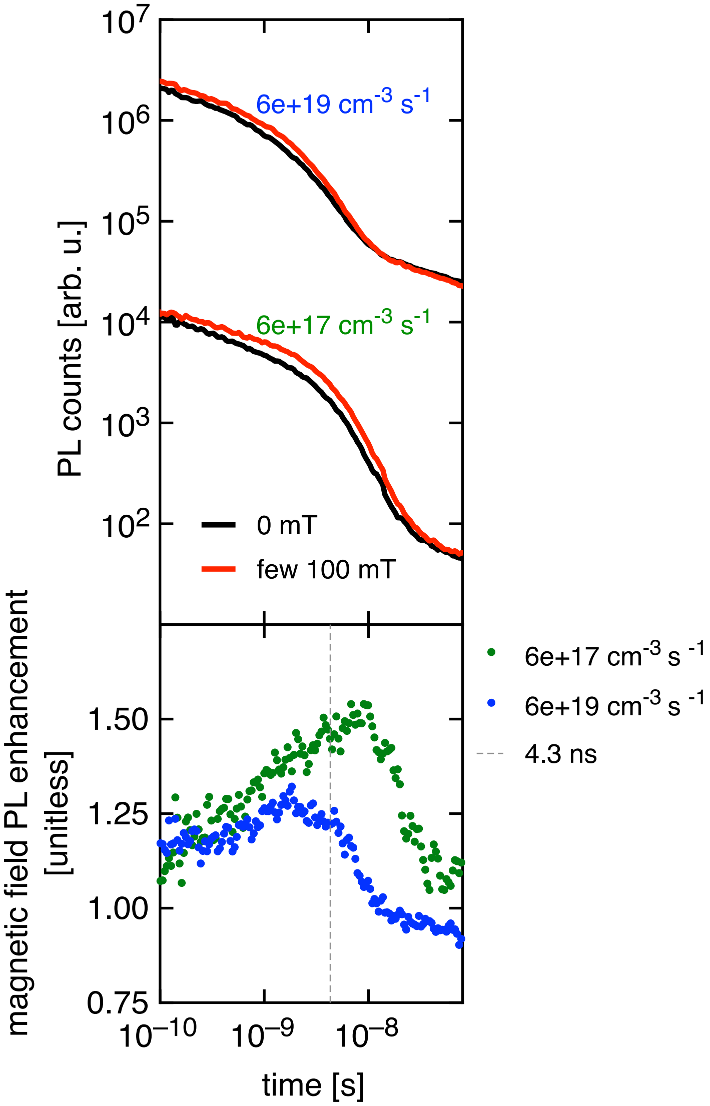

Figure 4.9: top: Measurement of time-correlated single photon counting of rubrene single crystal photoluminescence with and without magnetic field applied along *a* crystal axis, bottom: time dynamics of magnetic field enhancement factor (color online)

1.9 eV emission band. We analyzed these decays and found that the decay constant does not change with the applied magnetic field; only the amplitude of the emission changes, indicating an increase in PL contributions from the intermediate state excitons with the application of a magnetic field. This experiment shows that the 4.3 ns decay must somehow interact with an exciton of triplet character.

Discussion

Above we argued that the intensity of the 1.9 eV emission band requires that the defects interact with excitons, which is consistent with the observation that the relative importance of the 1.9 eV band grows with time. Our conclusion that the source of the 1.9 eV emission band cannot be from an impurity state directly excited by the laser that then decays away with a lifetime of 4.3 ns is very important. The later increase of the 1.9 eV band means that the defect states responsible for emitting the 1.9 eV photons is able to do so only after the initial excitation of excitons intrinsic to rubrene is transferred to the defects responsible for the lower energy emission. This transfer of energy could happen thanks to the large diffusion length of triplet excitons, which allows them to interact with even a relatively small density of defect states.

However, we know that diffusing excitons exist for a long time after photoexcitation, which implies that they interact with impurities all the time. The consistent interactions means that the impurity emission would be stimulated equally as long as the density of triplet excitons remains approximately the same. If independent triplets are created by fission in less than 100 ps, then the resulting triplet exciton density would interact with defect states at all times after excitation, which would make it impossible that a 4.3 ns exponential decay would emerge because of this.

On the other hand, we know that the initial pure singlets created by the laser pulse rapidly undergo state mixing into the intermediate quantum superposition state. It is therefore possible that the 4.3 ns exponential component that we have observed in the PL dynamics may be a direct observation of the intermediate exciton state's lifetime. We see it as a sharp decrease, rather than a washed out continuous process, because most of the population of intermediate state excitons (from singlet excitons created by the laser pulse) dissociate after 4.3 ns into independent triplet excitons.

However, it is also possible that the 4.3 ns exponential decay we are seeing is only related to the 1.9 eV band, and corresponds to an impurity lifetime, as argued in Ref [30] describing similar work where the authors found a shorter exponential decay of 1.8 ns. But in this work we have shown that the impurities must be excited via interactions with the intermediate state. In this case, the intermediate state lifetime needs to be very short and to match the rise time of the 1.9 eV band as seen in Fig. 4.8.

To summarize this section, we tentatively assign the 4.3 ns decay time that we have observed to the lifetime of the intermediate state. During its lifetime, the intermediate state can radiate a photon, causing an exponential decay of PL in the time dynamics measurements. In addition to this, we assume that the intermediate state can also diffuse and interact with defect states. When this happens, the radiative recombination happens at a defect site, and a lower energy photon is emitted. If we assume that photon emission from a defect occurs on a faster timescale than the intermediate state lifetime, it then follows that in 'altered' crystals there will be an enhanced emission at 1.9 eV as long as the intermediate state is still around to populate it. After 4.3 nanoseconds the intermediate state dissociates into independent triplet excitons, which can still interact with the defect states. Therefore the capture of two triplet states by the defect states would still lead to 1.9 eV emission. This would occur at lower probability and lower efficiency than when there is still a very large density of intermediate states during the first 4.3 ns after excitation. In this description, the additional defect states in the 'altered' crystals only serves as a sensitizer (observation mechanism) for the intermediate quantum superposition state.

4.2.2 Model

The PL time dynamics of rubrene tell a complicated story of exciton transformations. Our assignment in the last section of the 4.3 ns exponential decay to the intermediate state's triplet-pair dissociation lifetime adds a specific nonlinear step to the processes of singlet fission and triplet fusion. In this section, we add the intermediate state to a rate equation model of singlet and triplet populations, and analyze how the time dynamics are affected by it, we hope to better model experimental data by adding intermediate state.

Literature sources on excitonic singlet and triplet dynamics through fission and fusion have used a two-state model to consider the interaction of singlet and triplet excitons. Generally, these sources use limiting cases to understand triplet diffusion [37] or exciton species populations [12, 31]. Biaggio et al. [45] and Lyu et al. [72] present more-complete modeling on the time dynamics of the two-state system using rate equations for the singlet and triplet state populations to show how the triplet population is affected by singlet fission, triplet fusion, and triplet decay. We use the equations of Refs. [45, 72] as a starting point, and include the intermediate state exciton to create a more complete model of rubrene's time dynamics. Piland et al. [12] and Burdett et al. [24] perform a detailed study using a rate equation model to describe how magnetic fields perturb the number of triplet pair product states with singlet character and how this affects the singlet state kinetics. The conversion processes of the singlet, intermediate, and triplet excitonic states can be described using quantum theory as is done by Piland et al. and Bardeen et al.. Here, we only consider that these species conversions occur and do not go into the complex theory behind how such transitions happen.

Figure 4.10 describes our model exciton system by showing the energy levels for each state along the vertical energy axis. The left side of the graph considers a single excitonic state in the dimer picture (over two molecules simultaneously), while the right side of the figure uses the crystal model (excitations are localized to a single molecule). This is done to more accurately represent the quantum mechanical nature of the singlet and intermediate states, with an excitation which extends over two

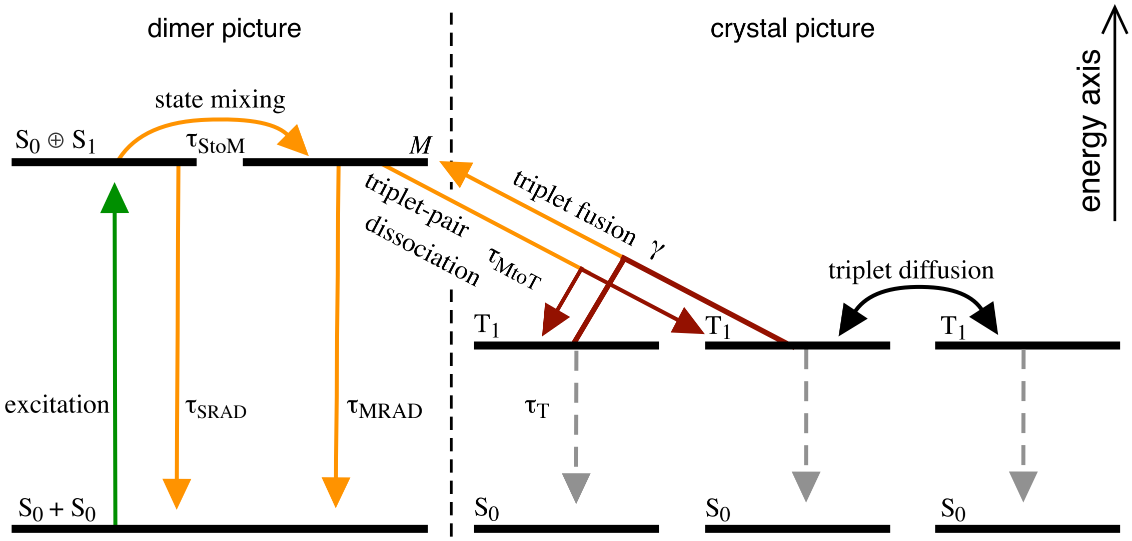

Figure 4.10: Energy level diagram showing excitonic fission and fusion processes with inclusion of an intermediate exciton state

molecules simultaneously, and the triplet states which may involve many molecules during triplet diffusion through the crystal.

Our model begins with excitation of the singlet exciton (S_0+S_1). This state may either radiatively decay with a lifetime τ_{Srad}, or undergo the state mixing process with a lifetime τ_{StoM} to become an intermediate state exciton. The intermediate state may either radiatively decay with a lifetime τ_{Mrad}, or undergo triplet-pair dissociation with a lifetime τ_{MtoT} to create two independent triplet excitons. As discussed in the background chapter on exciton fusion, the singlet character in the quantum superposition of the intermediate state is an excited singlet state, so the intermediate and singlet states must have the same energy. This means that, in our model, an exciton in the intermediate state is functionally equivalent to an exciton in the singlet state. For this reason, our model does not include a mechanism back to the initially excited singlet state from the intermediate state. Any photoluminescence that would be modeled from singlets recovered from the intermediate state is equally-well modeled as being emitted by the intermediate state.

Independent triplet excitons can decay non-radiatively with a lifetime τ_T, diffuse through the system to neighboring ground state molecules, or interact with another independent triplet exciton to recreate the intermediate state through triplet fusion. The bimolecular recombination rate, γ, accounts for the triplet fusion time, triplet density considerations, and the requirement that triplet excitons have opposite spin to undergo triplet fusion as measured in experiment.

Taking into account all the effects mentioned above, we obtain three coupled rate equations; one each for the singlet (S), intermediate (M), and triplet (T) state populations. A fourth equation is used to evaluate the excitons lost to photoluminescence (PL). These equations are:

$$\frac{dS}{dt} = -\frac{S}{\tau_{SRad}} - \frac{S}{\tau_{StoM}} \tag{4.2}$$

$$\frac{dM}{dt} = -\frac{M}{\tau_{MRad}} - \frac{M}{\tau_{MtoT}} + \frac{S}{\tau_{StoM}} + \frac{1}{2} f_{TtoM} \gamma T^2 \tag{4.3}$$

$$\frac{dT}{dt} = -\frac{T}{\tau_T} + 2\frac{M}{\tau_{MtoT}} - \gamma T^2 \tag{4.4}$$

$$PL = \frac{S}{\tau_{SRad}} + \frac{M}{\tau_{MRad}} \tag{4.5}$$

where S, M, and T are the populations of singlets, intermediate state, and independent triplets, τ_X is the decay lifetime of the process X, f_{TtoM} is the probability that the triplet fusion process is successful, and γ is the bimolecular recombination rate. f_{TtoM} accounts for T exciton interactions that do not contribute to the creation of M excitons.

We describe each of these equations term by term to relate it to the energy-levels diagram in Fig. 4.10. Equation 4.2 describes the the rate of change of singlet population by accounting for losses of singlets through both radiative emission and state mixing (respectively). Equation 4.3 accounts for changes in the intermediate state population with losses due to radiative decay and triplet-pair dissociation, and gains from state mixing and triplet fusion. The third equation, 4.4, accounts for changes in the triplet population through losses from its non-radiative decay, gains from triplet-pair dissociation, and losses from triplet fusion. The last equation, 4.5, counts excitons that undergo radiative decay from the singlet and intermediate states to simulate the photoluminescence emitted by the system.

4.2.3 Simulation of Time Dynamics

Equations 4.2 - 4.5 were numerically solved in Mathematica using the numerical differential equation solver NDsolve. This function can use several different solving algorithms in an evaluation and will change algorithms based on equation linearity, initial conditions, and point stiffness in order to provide the most accurate numerical solution possible.

The parameters we used in this model were chosen mostly from values found in the literature. The radiative singlet lifetime τ_{Srad} was determined to be 16 ns by lifetime fluorescence measurements on rubrene dissolved in solution [45, 46, 73]. The state mixing time, τ_{StoM}, was determined to be 10 ps through pump and probe measurements [30, 48, 49]. The triplet lifetime, τ_T, is $100 \mu s$ as determined in Ref. [47]. The bimolecular recombination rate γ is on the order of 1×10^{-12} Hz as determined by pump-and-probe measurements [48, 49, 74–76]. The triplet-pair dissociation time, τ_{MtoT}, is 4.3 ns from PL time dynamics measurements described earlier in this chapter [me!]. The last lifetime required, τ_{Mrad}, represents the intermediate state radiative lifetime, which has never been measured. We deduce its lifetime from the fact that at least 95% of the PL emitted from the system can be emitted via triplet fusion [31, 47]; this was used, in conjunction with all the other constants, in Equations 4.2 - 4.5 to solve for a calculated intermediate state radiative lifetime of $\sim$ 40 ns. Table 4.1 summarizes the input parameters and initial conditions used to obtain the simulated time dynamics of excitonic populations for the three exciton species.

Simulations presented here use the same conditions as our time-dynamics measurements in the last section, with a 190 fs laser pulsed at a 200 kHz repetition rate. We assume all incident photons create singlet excitations; and, each pulse is fully absorbed by the crystal (appendix A shows how S can be calculated from experimental measurements of power and excitation beam FWHM). Intermediate and triplet state excitons are not excited directly by the laser, so the M and T states begin with no population for the first laser pulse. However, the laser has only 5 μs between pulses which is significantly shorter than the triplet decay time in rubrene

Table 4.1: Summary of parameter inputs and initial conditions used for numerical simulations of exciton populations. Variable n in the initial condition S_0 runs from 0 to 29 to create the initial singlet population dependence seen in figure 4.12. Variable m represents the pulse number, so that S_0, M_0, and T_0 at pulse $m-1$ account for the exciton population at the end of the previous pulse.

S_0	$2^n \times 10^{15} + S_{m-1}(5\mu s)$	τ_{Srad}	$1 \times 10^{-12}\,\mathrm{s}$	τ_{StoM}	$15 \times 10^{-9}\,\mathrm{s}$
M_0	$M_{m-1}(5\mu s)$	τ_{Mrad}	$\sim 40 \times 10^{-9}\,\mathrm{s}$	τ_{MtoT}	$4.3 \times 10^{-9}\,\mathrm{s}$
T_0	$T_{m-1}(5\mu s)$	τ_T	$100 \times 10^{-6}\,\mathrm{s}$	f_{TtoM}	0.98
f_{laser}	200 kHz	γ	$1 \times 10^{-12}\,\mathrm{s}^{-1}$		

of 100 μs [47]; triplet excitons haven't finished decaying away by the next laser pulse. This means that the M and T populations at 5 μs following one pulse are used as initial conditions for evaluation of populations during the next pulse cycle. In our experiments, the crystal experienced millions of laser pulses for each measurement. Therefore the time dynamics of photoluminescence reached an equilibrium between pulses and the exciton dynamics between each pulse was identical. We 'pulsed' our simulation 150 times, which was sufficient to ensure that changes in excitonic population was less than 0.001% between pulses.

We evaluate our simulation of the time dynamics of rubrene's PL through a range of excitation powers as shown in Fig 4.11. The scaling of the y-axis does not represent the excitation S_0 population. Instead, the y axis is an unscaled emission axis that represents the PL emitted by the S and M states as given by Eq. 4.5. The initial singlet excitations used in our experimental simulations are listed in Fig 4.11 and are identical to what was used in our PL time dynamics experiments. This full time dynamics can be seen with the more-complete power dependent curves of Fig. 4.12, which extrapolates past the next laser pulse at 5 μs to the triplet decay. The initial singlet excitations in Fig 4.12 range from $1.0 \times 10^{17} - 3.5 \times 10^{24}$ and are spaced by factors of 2.

We identify features of our experiment that are captured well by our simulation through comparison of our experimental simulation in Fig. 4.11 with measured data

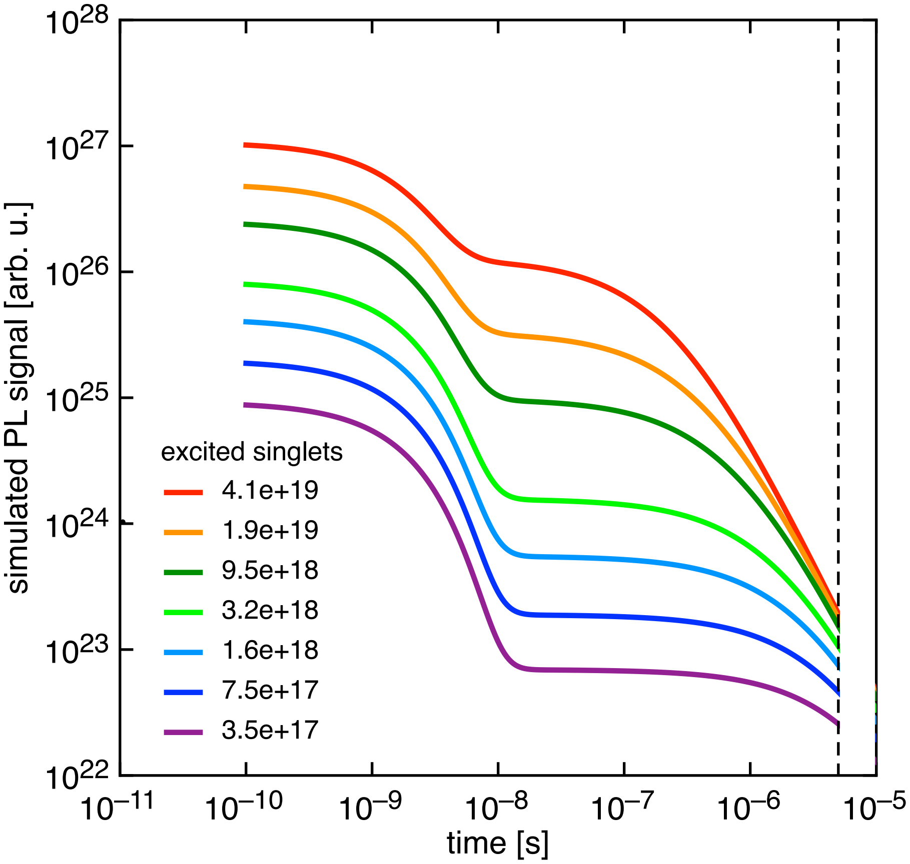

Figure 4.11: Simulation of time dynamics of singlet exciton state population using the parameters given in table 4.1 and laser powers used in experiments of Fig 4.2.

of from rubrene single crystals in Fig. 4.2 on page 68. First, the downward bending of the plots around 10^{-6} s shows strong bimolecular recombination for the highest excitation power measurements with a much weaker effect at the lower excitation powers. Second, and more importantly, the simulations show the disappearance of the exponential decay due to the intermediate state for higher excitation powers. This can be seen by comparing the simulated PL signal amplitude at 10^{-9} s to 10^{-7} s; the 4.1 e+19 singlets curve decays by one order of magnitude, while the 3.5 e+17 singlets curve decays by two orders of magnitude in that time range. We have identified this difference to be due to a large population of triplet excitons at

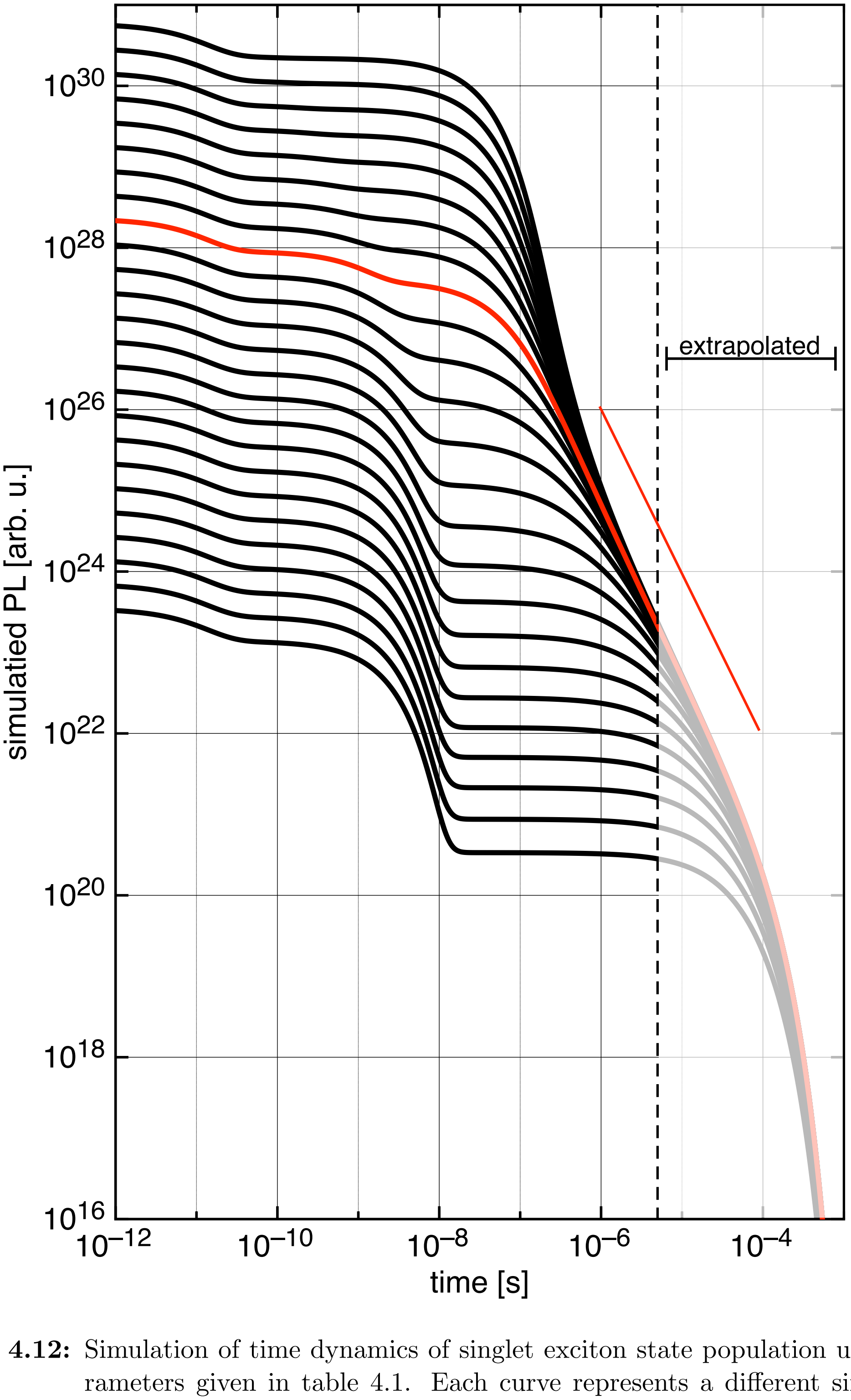

Figure 4.12: Simulation of time dynamics of singlet exciton state population using parameters given in table 4.1. Each curve represents a different simulated laser power. Red trace and line are guides to show power-law exponent of 2 in log-log scaling.

high initial singlet excitations. Triplet excitons have a nonradiative lifetime 20× longer than the period between pulses of our laser. This means that only 5% of triplets can decay before the next pulse and the remaining 95% carry into the next pulse cycle. At low singlet excitations, the triplet population undergoes triplet fusion at a sufficiently low rate to not effect the PL very much when compared to the radiative decay of singlet and intermediate exciton states. However, for higher singlet excitation the high triplet population undergoes a large amount of triplet fusion, which creates PL comparable to the PL from newly excited singlets and intermediate states that undergo radiative decay. We attribute the disappearance of the 4.3 ns intermediate state's triplet-pair dissociation lifetime from the PL time dynamics to an equilibrium, at high excitation densities, reached between the intermediate states dissociating into triplet excitons and triplet excitons recreating the intermediate state.

This full transition can be seen with the more-complete power dependent curves of Fig. 4.12, where the 4.3 ns decay completely disappears at high singlet excitation values. Also in that plot, a red line highlights that the solution to the time dynamics (the red solution curve) becomes a power-law with exponent of 2 from triplet fusion at later times, which is observed in experiment.

4.2.4 Single Crystal Conclusions

To summarize this chapter's results on rubrene single crystals, we reported the observation of an exponential decay of 4.3 ± 0.5 ns in the PL time dynamics of rubrene single crystals. We find this decay is present in 'pristine', 'altered' and a polycrystalline 'molten' samples. We used spectral filters to identify that this decay is strongly present in the 1.9 eV emission band we associate with an 'altered' rubrene spectrum. Spectral filtering of the time dynamics allowed us to show that this emission band appears after the initial laser excitation pulse. The state responsible for this decay must be associated with an exciton of singlet-character, since triplet-state excitons do not hold enough energy to radiate at 1.9 eV, the magnetic field enhancement of PL shows that this emission is effected by an interaction involving

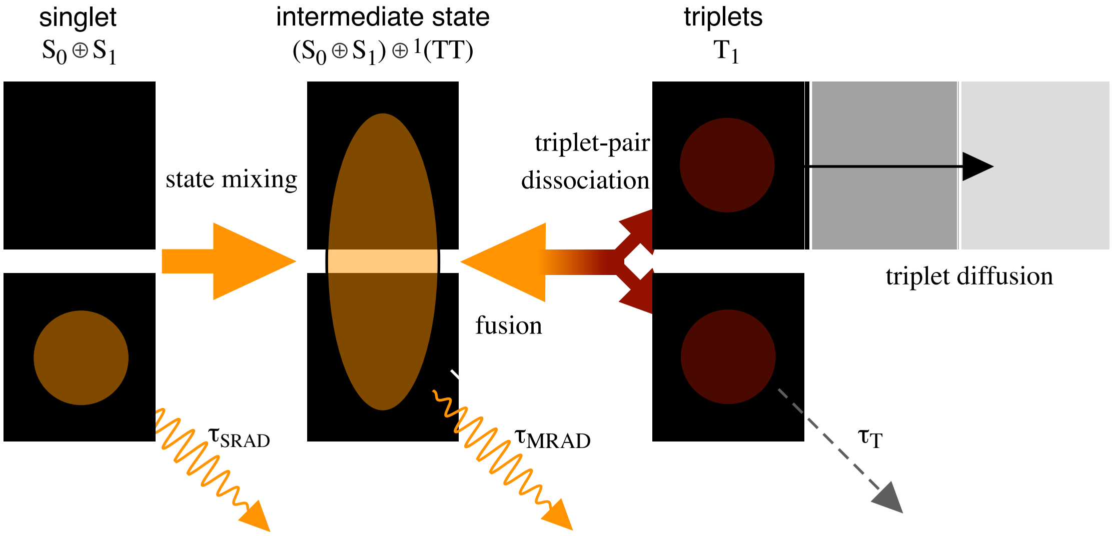

Figure 4.13: Spatial view of excitonic conversion processes.

a state with triplet character. So clearly, the state we're observing must have both singlet and triplet characters. We used these observations to assign the exponential decay of 4.3 ± 0.5 ns to the decay of the intermediate exciton state.

With this assignment, we created a three-state model of exciton dynamics in rubrene single crystals that helps describe our power-dependent PL time dynamics experiment. This model is summarized again in Fig. 4.13 with a spatial, molecular view. We created the model that used rate equations to simulate the PL emitted by our sample. This model is able to predict our experiment's proportional offset of PL time dynamics for times shorter than 10^{-8} s, can model triplet fusion effects after 10^{-7} s, and supports the disappearance of the intermediate state's contributions to PL time dynamics.

Our work using PL time dynamics measurements fills in several gaps in the literature. First, previous PL time dynamics measurements used either a 'polycrystalline' or 'altered' rubrene sample; we present the only full-scale time dynamics measurement in 'pristine' rubrene single crystals. Further, our detailed measurements can be represented on a log-log scale to provide more information, and allows for consideration of all parts of the system simultaneously. We assign our 4.3 ns decay to the triplet-pair dissociation rate of the intermediate state by using the 1.9 eV emission band as a sensitizer, which confirms a similar observation by Ma et al. [30], though they measure a decay time of 1.8 ns. We build upon our assignment by showing that the appearance of this decay is dependent on triplet exciton population and is less visible at the high excitation powers.

Finally, many experiments described in the literature use rubrene samples that the authors call amorphous but still exhibit signatures of exciton fission. In the next section we present the first time-dynamics study on an amorphous film proving that singlet fission has been minimized to exhibit a PL decay equivalent to preparations in solution.

4.3 Amorphous Rubrene Studies

So far, this dissertation has focused on rubrene single crystals for their efficient singlet fission. We now shift our efforts to learning about the singlet exciton state by stopping singlet fission completely in a solid-state amorphous sample of rubrene. In general, long-range molecular order should be absent in an amorphous molecular solid sample [77]. For rubrene, breaking the molecular ordering found in crystals should eliminate the possibility that singlet excitons can undergo fission [3, 78]. Elimination of singlet fission can clearly also be obtained by dissolving rubrene powder in a solvent to separate the rubrene molecules. Solid-state preparations of rubrene, from methods such as spin-coating and vapor deposition, have been used in Refs [12, 24, 30, 71] to study the time dynamics of photoluminescence from an amorphous sample, although some of those preparations may create polycrystalline rubrene instead. In general, a polycrystalline sample is similar to an amorphous sample but contains clusters of nanocrystals with random shapes, grain sizes, and orientational packing [77]. This may include a small crystal or dimer-like arrangement of molecules which can restore excitonic fission. The small region of molecular order could confine the resulting triplet excitons, which may affect the fusion process considerably. In the present work we prepared vapor-deposited thin films of rubrene that are stable under ambient conditions, and which exhibit time dynamics very similar to preparations in solution.

We learn about singlet fission in amorphous samples by measuring the time dynamics of photoluminescence. The time dynamics of rubrene without the ultra-fast fission process should show only the initially-excited singlet exciton's exponential decay lifetime of 16 ns [45, 46]. Some groups working on rubrene have found a 10 ns exponential decay lifetime for the singlet lifetime. We point out that this is the decay lifetime of rubrene when dissolved in a polar solvent, like alcohol or chloroform [46, 73]. The molecules that make up a polar solvent have a net dipole moment, which is able to interact with the excited states of rubrene and can shorten the relaxation lifetime of excited molecules [79]. Changes in the dynamics of photoluminescence from this monoexponential decay, such as a steeper initial decay of PL or delayed photoluminescence emission, indicate that singlet fission and triplet fusion may still be occur in the sample.

We have found that previous works that claimed to have carried out measurements in amorphous rubrene, such as those in Refs [12, 24], must have actually been carried out in samples consisting of assemblies of randomly oriented nanocrystals; the PL decay dynamics reported in those samples still show signatures of fission and fusion. Piland et al. [12] and Burdett et al. [24] use a spin coating evaporative method to create a sample they declared amorphous based on its emission spectrum and absence of x-ray diffraction peaks. The PL time dynamics they reported have time-dependences that points to fission and fusion effects, similar to our results in section 4.2. They report three exponential time constants: one that is sub-nanosecond, one that is 2.2 ns, and a third that is 50 ns. Piland et al. [12] and Burdett et al. [24] note that creating a reproducible spin-coated amorphous sample is challenging, and that optical inspection of their early samples showed micro-crystal domains. In response, they developed a method to create optically defect-free samples, but still reason that their method may produce nanometer-sized domains below the optical resolution of their system. Piecing together the complex PL time dynamics with the possibility of nano-sized domains we conclude their spin-coated samples are likely polycrystalline, where singlets may undergo fission, rather than amorphous.

Jankus et al. thermally evaporated rubrene onto a sapphire substrate and also report no crystal structure using x-ray diffraction [74]. The PL time dynamics of Jankus et al's sample exhibit an initial exponential decay of photoluminescence (which they call prompt fluorescence), with a time constant of 2 ns at 295 K that is dependent on temperature, which they attribute to a temperature dependence of singlet fission. Additionally, their data shows a power-law decay of PL after 100 ns (they call it delayed fluorescence) which can be attributed to bimolecular recombination of triplet excitons [47, 74]. Similar to the work of Piland et al., Jankus et al's sample exhibits complicated PL time dynamics which clearly shows signatures of singlet exciton fission.

Gieseking et al. [71] present work that shows a vapor-deposited sample of amorphous rubrene, but are unable to follow their PL time dynamics measurement into the nanosecond time scale due to a limited measurement window. The possible beginning of a mono exponential shows that their film may effectively limit singlet fission.

Physical vapor deposition is also used in work described in other publications to create amorphous rubrene, similar to the samples of Jankus et al. and Gieseking et al., although those studies are more interested in understanding the processes that allow for crystallization of the amorphous material than exciton dynamics [80–83]. One of those publications, by Park et al., presents AFM and optical measurements that show that immediately after deposition, most of their rubrene sample can be classified as amorphous [80]. They then focus on the processes that allow amorphous rubrene to slowly form crystalline regions, which they call spherulitic disks. These disks are a type of polymer-link crystal, with radially-oriented long chains of aligned molecules called llamelae [84]. The coexistence of the two sample regions, amorphous and spherulitic disks, present an interesting sample for our PL time dynamics studies.

We successfully prepared thermally vapor-deposited amorphous films that are stable at room conditions, and characterized them by studying signatures of fission using time correlated single photon counting methods.

We created our amorphous rubrene films via molecular beam deposition, where rubrene molecules were sublimated at 150°C in high vacuum (10^{-5} Torr). The substrate was washed using ultrasound baths in alcohol and acetone, then heated to 100 °C in the vacuum chamber at 10^{-5} Torr to remove water molecules from the surface. The substrate was then allowed to cool to room temperature. Next, a small amount of Acros Organics 99% Rubrene was heated in a glass crucible to 150 °C with a shutter covering the substrate where the film was to be deposited to prevent volatile impurities from depositing onto the substrate while the powder was heated. Once the powder reached 150 °C, we waited 15 minutes before moving the shutter out of the way of the substrate to allow molecular deposition to begin. We deposited for 8 hours at 0.05–0.2 Å/s, with which we created a 600 nm film for our thick sample and less than 150 nm film for our thin sample, as measured using optical interference and absorption techniques. We varied the thicknesses of our final films by adjusting the amount of initial rubrene powder in the glass crucible; 2 mg of rubrene powder was used for the thin amorphous film and 10 mg for the thick film.

Macroscopically, the films appear to have a very uniform orange-pink color, which are slightly different for the two film thicknesses and show no visible anisotropic behavior when viewed between crossed polarizers. After exposure to ambient conditions for a few days, the sample's color had faded slightly; however, no changes in the shape of the photoluminescence spectrum, absorption spectrum, or time dynamics were found between measurements just after initial exposure to air and after a period of 72 hours of atmospheric and ambient light conditions. These results are consistent with those reported in Ref. [41]. The most noticeable change in the amorphous regions of our samples was a photobleaching effect left by a 450 nm (3.1 eV) continuous wave excitation beam. We saw no changes in spectral shape of photoluminescence during photobleaching, except at very high excitation intensities that burned the molecular film and created a broad-band PL spectrum that was void of any known rubrene peaks (see the burn trail in Fig. 4.14). Without burning, photobleaching attenuated the strength of emitted PL by more than a factor of two within a few seconds for both film thicknesses at high-excitation powers ($>10^{18}$ excitations $\mathrm{s}^{-1}\mathrm{cm}^{-2}$), and the color of the rubrene changed from reddish-orange to transparent at the excitation site. The rate of this bleaching effect slowed at lower excitation rates. For this reason, we collected PL measurements immediately after translating the amorphous film to a new spot to maximize signal and avoid measurements at photobleached rubrene.

The intensity dependence of the photobleaching effect may be explained by an oxidation of the rubrene molecules [85]. Interestingly, the appearance of the 1.9 eV emission band from 'altered' rubrene's photoluminescence is linked to an oxidation of rubrene, but isn't observed in these samples.

Our vapor-deposited samples are very similar to those reported by Park et al. [80], with large regions of amorphous rubrene and spherulitic disks. However, our samples have smaller spherulitic disks (an example can be seen in Fig. 4.14) which are stable under atmospheric conditions; we found no single disk larger than $\sim 200\,\mu$m in diameter. We hypothesize that this is because we used a much higher deposition temperature than Park et al.. Our deposition was carried out at a higher temperature than even their annealing process. The micro-crystal domains are rare on our thin amorphous film, but are quite common on the thick film and can grow in large quantities as part of a colony of domains where edges of the domains touch. For our measurements testing amorphous regions, we avoided these spherulitic disks by imaging the sample first to select an amorphous sample site.

Figure 4.14 shows the photoluminescence and absorption spectra of rubrene in three different forms: our amorphous film, rubrene dissolved in a hexane solvent, and a rubrene single crystal (for reference).

First, we note the amorphous film's absorption spectrum displays many of the same absorption bands as the single crystal, though in different relative amplitudes. Our think film measurements agree well with measurements made by Park et al. [80] in their samples without annealing, and with the prediction from the molecular absorption and emission properties derived from the analysis of rubrene single crystals.

Comparing the photoluminescence emitted by the thin amorphous film to rubrene in hexane shows a practically identical PL spectrum except for the extra bump at 2.45 eV in the thin film spectrum which we cannot explain. The photoluminescence

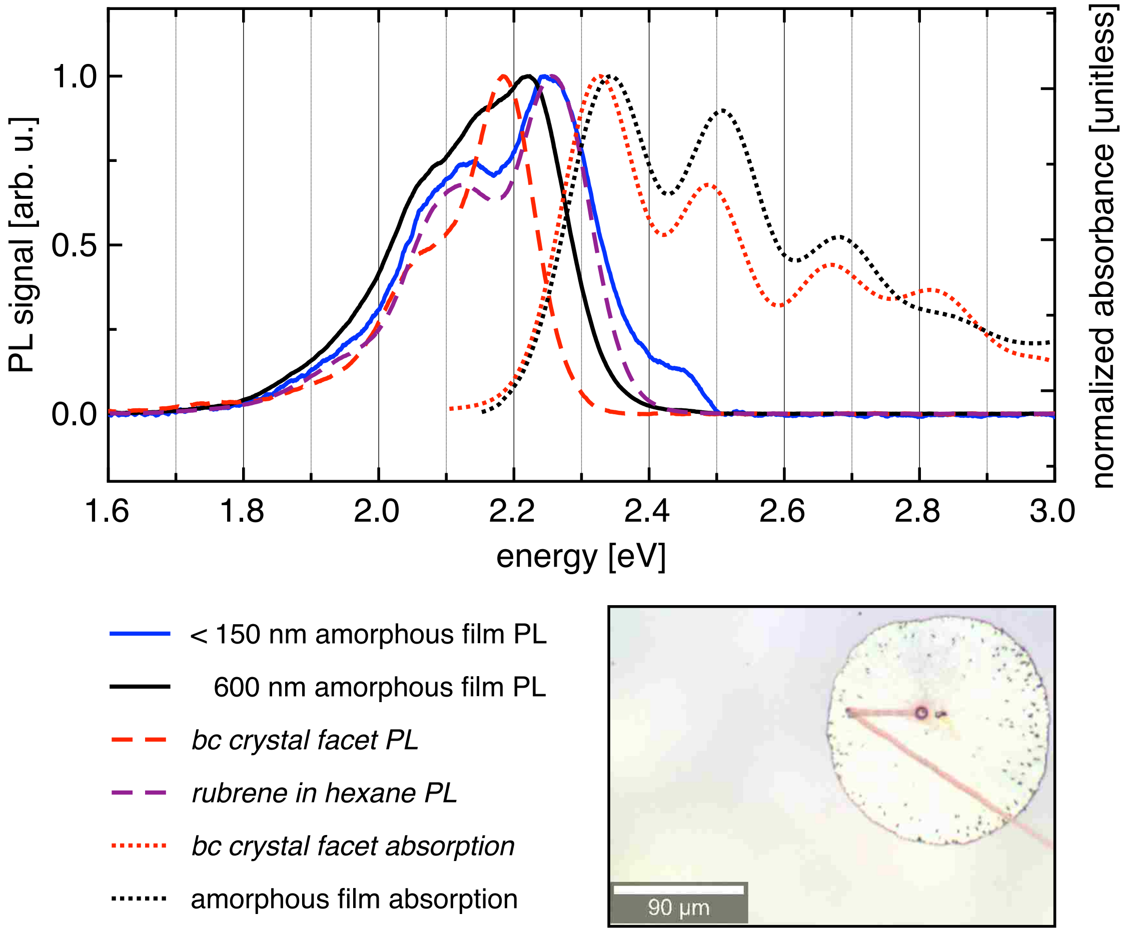

Figure 4.14: Normalized photoluminescence spectra for the thick and thin amorphous films and a *bc* facet of rubrene single crystals (top). Image of a microcrystal domain on thick amorphous crystal (bottom). Red photobleached/burned line made with translation of sample under high-power laser illumination.

of the thick amorphous film (solid black curve) is shifted towards longer wavelengths compared to the PL spectrum of the thin amorphous film. This can explained by a greater amount of reabsorption of PL by the thicker sample, which gives the appearance of shifting the emission bands that overlap the absorption curve to lower energies, similar to reabsorption found in the photoluminescence of single crystals [38]. The double peak shape of the thin film and hexane solution is hidden by an extra peak at 2.14 eV for the thick film; unfortunately, we do not know what causes

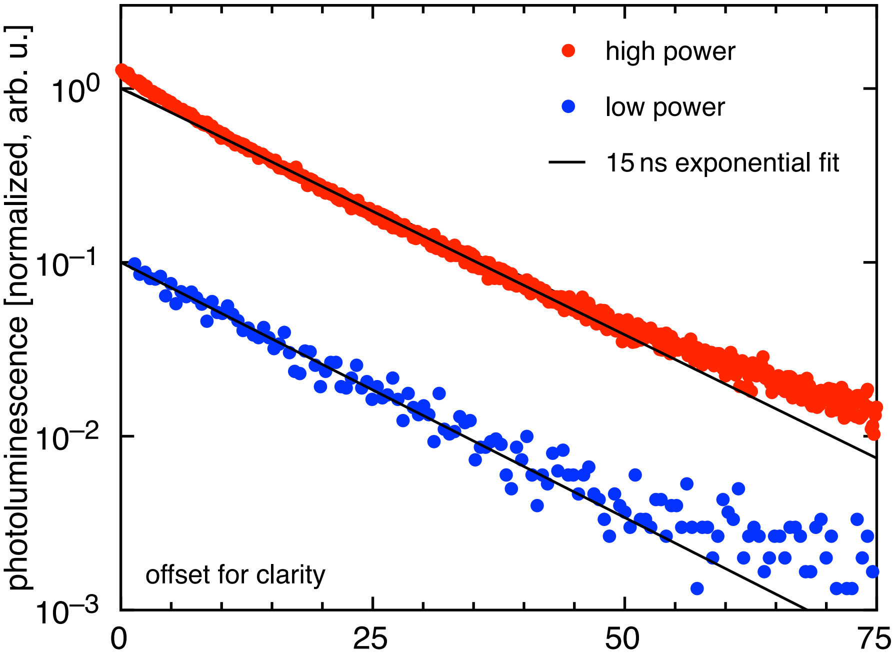

Figure 4.15: PL time dynamics for an amorphous rubrene film showing an exponential decay of 15 ± 1 ns, equivalent to the singlet exciton lifetime found in nonpolar solutions. Curves normalized to y-intercept from fit of exponential decay of 15 ns; offset by factors of 10 for clarity.

this extra band in the PL of the thick film.

Figure 4.15 shows that the exponential decay of PL from our amorphous thin films has a lifetime of 15 ± 1 ns. This decay lifetime is slightly shorter than the known fluorescence lifetime of 16.5 ns for rubrene in a nonpolar solvent [45, 46]. However, we still assign this as an observation of the singlet exciton's radiative lifetime. This experiment was performed with excitation light that avoided the spherulitic disks. We measured the decay at both high and low excitation powers and saw no change in the singlet exciton lifetime, as shown in Fig. 4.15. We do find a small deviation of the PL time dynamics from an exponential decay at times shorter than 10 ns in our high excitation power measurements which can be attributed to a small amount of singlet fission. Because molecules in the amorphous film are randomly oriented, it is probable that there are some regions with ordered molecules, allowing

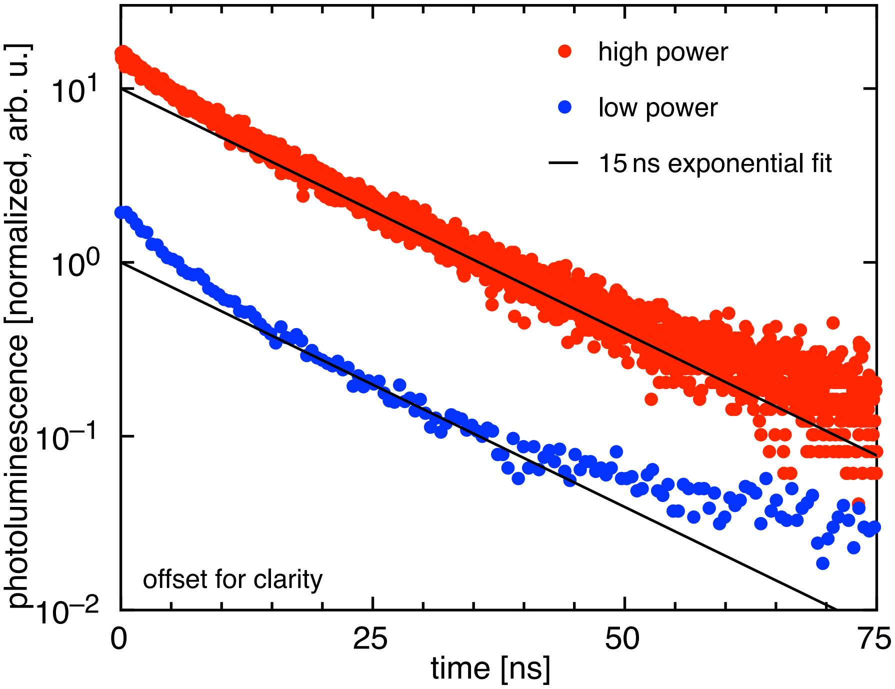

Figure 4.16: PL time dynamics using an excitation beam which includes some spherulitic disks on the rubrene thin film showing an exponential decay of 15 ns, equivalent to the singlet exciton lifetime found in non-polar solution, as well as an enhanced initial decay for times less than 10 ns. Curves normalized to y-intercept from fit of exponential decay of 15 ns; offset by factors of 10 for clarity.

for singlet fission and triplet fusion. This presents us with an understanding of how an amorphous rubrene film is different than rubrene in solution; in an amorphous film rubrene molecules are isolated by other rubrene molecules, whereas in solution, rubrene molecules are isolated by solvent molecules. Rubrene molecules surrounded by other rubrene molecules are able to create the geometry required to allow for singlet fission. However, we reason that the geometry that allows for singlet fission is in a minority of molecular arrangements among molecules which explains the relatively small amplitude of the initial non-exponential decay. We also observed that the randomly-oriented film does not show any significant diffusion length for triplet excitons. This means that any triplets created have to recombine with their sibling triplet exciton and contribute to delayed florescence, although this PL would be relatively weak.

In summary, we have shown the amorphous character of our samples by showing that their PL time dynamics exhibit rubrene's intrinsic singlet lifetime, with a small amount of fission as predicted for an amorphous rubrene film.

Figure 4.16 shows similar PL time dynamics measurements of our film, but for these data the excitation region includes spherulitic disks in addition to regions of amorphous film. These data show an initial decrease of photoluminescence for times less than 10 ns that is much larger than what was seen for the amorphous region alone. We also see contributions to PL from triplet excitons undergoing triplet fusion at timescales approaching 75 ns. The early time decay in PL and the long-time scale increase in PL show that these spherulitic disks allow for singlet fission and triplet fusion, which confirms that they contain some molecular ordering and could be used to make a polycrystalline sample. The fission/fusion contributions we see here are also evident in the time dynamics of the spin-coated sample created by Piland, Burdett et al [12, 24], from which we conclude that their sample is better described as polycrystalline than as amorphous.

In conclusion, we've created a vapor-deposited thin film and show that it enables us to determine a lower limit to the exciton fission rate in solid-state rubrene samples. The amorphous regions of the film show a 15 ± 1 ns exponential decay of PL which we attribute to the singlet exciton's radiative decay lifetime. Inclusion of spherulitic disks in our time dynamics measurements proved that singlet fission and triplet fusion occur in those disks, although a more accurate measurement of the fast and slow components of the PL time dynamics could lead to more insights.

Chapter 5

Conclusions and Outlook

We combined steady-state photoluminescence (PL) with PL time-dynamic measurements to tell the story of singlet, intermediate, and triplet state excitons. This was possible through use of detail-oriented measurement techniques and an understanding of how to isolate the phenomena that we measure which allowed us to reliably determine even relatively weak effects.

We have contributed to the understanding of singlet fission by identifying how environmental factors can change the rate at which singlet fission occurs. We saw no changes in the PL spectrum when applying magnetic fields with strengths up to 1 T, nor when changing the sample's temperature between 295 K and well below 50 K. Our experiments showed that a 1 T magnetic field applied to rubrene enhances the PL yield by 20% at low excitation rates which we attribute to a reduction in the singlet fission rate of up to 20%. The increase in PL with a 1 T field was only 5% at high excitation rates, because the contributions to PL from triplet fusion mask the effects of the 20% lower singlet fission rate.

More generally, our temperature-dependent experiments showed an enhancement of PL by up to a factor of 9 between room temperature and temperatures on the order of 150 K. This change in the fission efficiency while changing temperature is due to the removal of thermal energy from the sample which was able to reduce the probability of fission and/or fusion.

For the first time in rubrene we were also able to identify a 4.3 ± 0.5 ns exponential decay in the PL time dynamics and assign it to the intermediate state exciton's dissociation into two independent triplet excitons. We hypothesize that this was made more clearly visible by using defect sites linked to the 1.9 eV emission band as sensitizers which efficiently interact with the intermediate state to emit lower energy photons that we spectrally isolated. Spectral filtering of the PL time dynamics showed that the species emitting lower energy photons must be excited after the laser pulse, and are caused by the later interaction of photoinduced excitons with defect states. With an understanding of the intermediate state lifetime, we were able to model the time dynamics of singlet and triplet excitons in a three-state system. From that, we extracted the equilibrium condition between triplet-pair dissociation and triplet fusion as a mechanism that can, at higher excitation densities, wash-out the intermediate state effects from the PL time dynamics measurements. We also gathered more information about the PL enhancement caused by an applied magnetic field using PL time dynamics measurements in 'altered' rubrene in which we measured an enhancement of the exponential transient related to the intermediate exciton state.

Through careful experiment design and data collection, we were able to observe effects of the triplet state in many of our experiments; even though it is effectively a 'dark' state that cannot radiatively decay. Most notably, we observed a 25% increase in the triplet exciton's diffusion length, from $4 \pm 0.4\mu$m to $5.4 \pm 0.4\mu$m, with the application of a 1 T magnetic field.

Finally, we used PL time dynamics methods to measure a mono-exponential decay of PL with lifetime 15 ± 1 ns in a film of rubrene that we synthesized, showing that it was consistent with material that is amorphous at a molecular level.

An important point we stressed throughout this dissertation is that these experiments require a very high level of attention to details, which allowed us to identify and control artifacts that have affected previous results in the literature. This ended up playing a key role in leading us to collect the data and preform the analysis presented here. We note that this is still an evolving field and that most changes we observed are relatively small. The conclusions we draw here are based on our best evaluations of current literature sources and our own work.

Future work on the excitonic states of rubrene should build on this work's conclusions to design new experiments to determine the properties of the intermediate state. The most obvious next experiment in line with this work would be a temperature-dependence of the PL time dynamics in both 'intrinsic' and 'altered' rubrene single crystals. We also note that a temperature-dependence measurement of PL diffusion may be possible with better control of optical reflections from cryostat windows. Combining these two experimental setups, precise control over spatially-resolved collection methods could allow for time-dependent diffusion measurements; despite the long triplet lifetime in rubrene. That experiment would require the use of low repetition rate to allow time for triplet excitons to relax between pulses which would make it difficult to accumulate a signal with a good signal to noise ratio.

Appendix A

Derivation of Excitation Density

In order to compare results in experiments which include singlet exciton recovery from triplet excitons (fusion), it's necessary to know the excitation density during each measurement. This appendix provides an explicit derivation of the singlet excitation density per laser pulse at the surface of a material, S_{1pulse}, which is based on parameters of the the excitation source and the crystal. In each experiment, the average laser power, P_L of the beam is measured, along with the full width at half maximum (FWHM.) The absorption length in the crystal is known from other experiments.

The two dimensional spatial distribution of the beam intensity is modeled with a gaussian profile, symmetric in θ, as

$$I(r,\theta) = I_0 e^{-\frac{2r^2}{w^2}} \tag{A.1}$$

where w describes the gaussian beam waist and I_0 is the average excitation intensity. w is related to the FWHM by FWHM $= \sqrt{2\ln(2)}w$.

Optical absorption through a uniform material can be described by the Beer-Lambert law, where the intensity of an excitation beam decreases as it propagates through the depth of the sample along z,

$$I(z) = I_0 e^{-\frac{z}{d}},. \tag{A.2}$$

Here z is the distance from the medium interface, and d is the optical absorption length (often represented with λ, or in terms of the absorption coefficient $\alpha = \frac{1}{d}$).

The intensity of the excitation beam in the the bulk of the crystal is then given by

$$I(r,\theta,z) = I_0 e^{-\frac{2r^2}{w^2}} e^{-\frac{z}{d}}. \tag{A.3}$$

We relate the laser power to the laser intensity parameters using $P = IA$ by integrating the laser intensity over polar coordinates r and θ:

$$\begin{aligned}
P_L =& \int_0^{2\pi} \int_0^{\infty} I(r,\theta) r dr d\theta \qquad \text{(A.4)}\\
P_L =& \int_0^{2\pi} \int_0^{\infty} I_0 e^{\frac{-2r^2}{w^2}} r dr d\theta\\
P_L =& 2\pi I_0 \int_0^{\infty} e^{\frac{-2r^2}{w^2}} r dr\\
\text{substituting:} \quad & u = r^2 \rightarrow du = 2rdr\\
P_L =& \pi I_0 \int_0^{\infty} e^{\frac{-2u}{w^2}} du\\
P_L =& -\pi I_0 \frac{w^2}{2} e^{\frac{-2u}{w^2}} \Big|_0^{\infty}\\
P_L =& -\pi I_0 \frac{w^2}{2} [0-1]\\
P_L =& \pi I_0 \frac{w^2}{2}. \qquad \text{(A.5)}
\end{aligned}$$

$$\text{We then recall that: } \text{FWHM} = w\sqrt{2\ln(2)} \rightarrow w^2 = \frac{\text{FWHM}^2}{2\ln(2)}$$

$$\begin{aligned}
P_L =& \pi I_0 \frac{1}{2}\left(\frac{\text{FWHM}^2}{2\ln(2)}\right)\\
P_L =& \pi I_0 \frac{\text{FWHM}^2}{4\ln(2)}\\
P_L =& I_0 (\pi \text{FWHM}^2) \left(\frac{1}{4\ln(2)}\right) \qquad \text{(A.6)}
\end{aligned}$$

Equation A.6 is shown as being grouped into terms that present the peak intensity I_0 of the laser, the circular beam area, and a geometric factor that spreads the intensity as a gaussian function. Recall that P_L and FWHM are directly measured in each experiment. Solving for the peak beam intensity:

$$I_0 = P_L \frac{4\ln(2)}{(\pi \text{FWHM}^2)}. \tag{A.7}$$

Each layer deeper into the crystal is reached by a different excitation beam intensity reach it because of absorption in layers closer to the surface; this is described by Eq. A.2. The change in beam intensity due to absorption for one layer is described by:

$$\frac{I(z+dz)-I(z)}{dz}=\frac{dI}{dz}$$

$$I(z+dz)-I(z)=dz\frac{dI}{dz}$$

Using this result with the Beer Lambert law in Eq. A.2 yields,

$$\frac{dI}{dz}=-\frac{I_0}{d}e^{-\frac{z}{d}}. \tag{A.8}$$

Excitation density is calculated directly from equation A.8 with the identification that excitations are created from a change in beam intensity. In rubrene, each photon from the laser beam creates one excitation. To convert the intensity to a flux of photons, we divide both sides of the equation by the energy of one photon, $E=\frac{hc}{\lambda}$. This yields:

$$\frac{dI}{dz}\frac{\lambda}{hc}=-\frac{I_0}{d}\frac{\lambda}{hc}e^{-\frac{z}{d}},$$

where λ describes the wavelength of the incident photons and h and c are the fundamental constants. We are interested in the excitation density at the surface of the crystal, which is the limit of small layer thickness ($z \to 0$) where the exponential term approaches 1, leaving

$$\frac{dI}{dz}\frac{\lambda}{hc}=-\frac{I_0}{d}\frac{\lambda}{hc}.$$

The left hand side of this equation is the number of photons the beam loses per unit volume to create singlet excitations in the crystal per unit time. The singlet excitation density rate at the surface of the crystal, S_0, has the opposite sign to account for the gain of excitations by the crystal:

$$S_0=-\frac{dI}{dz}\frac{\lambda}{hc}$$

$$S_0=\frac{I_0}{d}\frac{\lambda}{hc}.$$

Plugging in I_0 from Eq. A.7 results in an excitation density rate in terms of measurable quantities,

$$S_0 = P_L \frac{4\ln(2)}{\pi \mathrm{FWHM}^2 d} \left(\frac{\lambda}{hc}\right). \tag{A.9}$$

Equation A.9 gives the excitation density in a crystal created by a continuous beam laser. To get the number of singlet excitations in one pulse of a pulsed laser, the frequency f is used to cancel time components in P_L and S_0, leaving:

$$S_{1Pulse} = \frac{S_0}{f} = P_L \frac{\lambda}{hc} \left(\frac{4\ln(2)}{\pi \mathrm{FWHM}^2 d}\right) \frac{1}{f}. \tag{A.10}$$

Appendix B

Derivation of Triplet Population Density Spatial Distribution

As part of a bonus round on triplet diffusion, we introduce work we have done on modeling the diffusion profile using rate equations to describe the three exciton species. As described earlier, the 1-D diffusion model above is based on the large-diffusion lengths solution to a two-state exciton system [37]. Chapter 4 of this thesis introduces evidence of an intermediate exciton state, which we include in the exciton system by modifying the two-state rate equations in our model presented in that chapter.

This is a derivation of a second-order nonlinear differential equation that can describe the spatial diffusion of triplets in equilibrium with any source function $G(x)$ to describe the spatial distribution of excitations added to the system. Beginning with our model for singlets, triplets, and the intermediate state as described in Ch 4, we account for exciton diffusion terms and obtain:

$$\frac{dS(x,t)}{dt} = -\frac{S(x,t)}{\tau_{SRad}} - \frac{S(x,t)}{\tau_{StoM}} - \frac{S(x,t)}{\tau_{SnonRad}} + D_S \frac{d^2}{dx^2} S(x,t) + G(x,t) \tag{B.1}$$

$$\frac{dM(x,t)}{dt} = -\frac{M(x,t)}{\tau_{MRad}} - \frac{M(x,t)}{\tau_{MtoT}} + \frac{S(x,t)}{\tau_{StoM}} + \frac{1}{2} f_{TtoM} \gamma T^2(x,t) + D_M \frac{d^2}{dx^2} M(x,t) \tag{B.2}$$

$$\frac{dT(x,t)}{dt} = -\frac{T(x,t)}{\tau_T} + 2\frac{M(x,t)}{\tau_{MtoT}} - \gamma T^2(x,t) + D_T \frac{d^2}{dx^2} T(x,t) \tag{B.3}$$

$$PL(x,t) = \frac{S(x,t)}{\tau_{SRad}} + \frac{M(x,t)}{\tau_{MRad}} \tag{B.4}$$

Diffusion experiments are performed using a continuous source function, so $\frac{d}{dt} = 0$, and all time dependencies (x,t) reduce to only a spatial dependence (x). Also, for crystal rubrene, the lifetimes of the singlet and intermediate states are short, so no diffusion of those species occurs. This means D_S and $D_M = 0$ and our equations reduce to:

$$0 = -\frac{S(x)}{\tau_{SRad}} - \frac{S(x)}{\tau_{StoM}} - \frac{S(x)}{\tau_{SnonRad}} + G(x) \tag{B.5}$$

$$0 = -\frac{M(x)}{\tau_{MRad}} - \frac{M(x)}{\tau_{MtoT}} + \frac{S(x)}{\tau_{StoM}} + \frac{1}{2} f_{TtoM} \gamma T^2(x) \tag{B.6}$$

$$0 = -\frac{T(x)}{\tau_T} + 2\frac{M(x)}{\tau_{MtoT}} - \gamma T^2(x) + D_T \frac{d^2}{dx^2} T(x) \tag{B.7}$$

$$PL(x) = \frac{S(x)}{\tau_{SRad}} + \frac{M(x)}{\tau_{MRad}}. \tag{B.8}$$

The first equation can be solved to describe the singlet dynamics as

$$S(x) = \frac{G(x)}{\left(\frac{1}{\tau_{SRad}} + \frac{1}{\tau_{StoM}} + \frac{1}{\tau_{SnonRad}}\right)} \tag{B.9}$$

which can be plugged into Eq. B.6 that describes the intermediate state. Solving this equation for $M(x)$, we reach:

$$M(x) = \frac{\frac{S(x)}{\tau_{StoM}} + \frac{1}{2} f_{TtoM} \gamma T^2(x)}{\left(\frac{1}{\tau_{MRad}} + \frac{1}{\tau_{MtoT}}\right)} \tag{B.10}$$

which can be plugged into the triplet equation, this allows us to solve for the diffusion term,

$$D_T \frac{d^2}{dx^2} T(x) = \frac{T(x)}{\tau_T} - 2\frac{M(x)}{\tau_{MtoT}} + \gamma T^2(x) \tag{B.11}$$

Plugging in Eq. B.10 for $M(x)$ gives:

$$D_T \frac{d^2}{dx^2} T(x) = \frac{T(x)}{\tau_T} - 2\frac{\frac{S(x)}{\tau_{StoM}} + \frac{1}{2} f_{TtoM} \gamma T^2(x)}{\tau_{MtoT}\left(\frac{1}{\tau_{MRad}} + \frac{1}{\tau_{MtoT}}\right)} + \gamma T^2(x), \tag{B.12}$$

which can be simplified by collecting T^2 terms:

$$D_T \frac{d^2}{dx^2} T(x) = \frac{T(x)}{\tau_T} + \left(1 - \frac{f_{TtoM}}{\left(\frac{\tau_{MtoT}}{\tau_{MRad}} + 1\right)}\right) \gamma T^2(x) - \frac{2S(x)}{\tau_{StoM}\left(\frac{\tau_{MtoT}}{\tau_{MRad}} + 1\right)}. \tag{B.13}$$

Plugging in Eq. B.9 for $S(x)$, we reach:

$$D_T \frac{d^2}{dx^2} T(x) = \frac{T(x)}{\tau_T} + \left(1 - \frac{f_{TtoM}}{\frac{\tau_{MtoT}}{\tau_{MRad}} + 1}\right) \gamma T^2(x) - \frac{2G(x)}{\left(\frac{\tau_{StoM}}{\tau_{SRad}} + 1 + \frac{\tau_{StoM}}{\tau_{SnonRad}}\right)\left(\frac{\tau_{MtoT}}{\tau_{MRad}} + 1\right)}. \tag{B.14}$$

Finally, we use $D_T = L^2/\tau_T$ and $\tau_{SnonRad} = \infty$, leaving:

$$\frac{L^2}{\tau_T} \frac{d^2}{dx^2} T(x) = \frac{T(x)}{\tau_T} + \left(1 - \frac{f_{TtoM}}{\frac{\tau_{MtoT}}{\tau_{MRad}} + 1}\right) \gamma T^2(x) - \frac{2G(x)}{\left(\frac{\tau_{StoM}}{\tau_{SRad}} + 1\right)\left(\frac{\tau_{MtoT}}{\tau_{MRad}} + 1\right)}. \tag{B.15}$$

We give a term-by-term intuitive sense to what this equation means: in the steady state, the number of triplet excitons diffusing into a region of space is equal to the number of triplets that decay away plus the triplets that undergo fusion to the intermediate state minus the triplets that are created from the intermediate state by triplet-pair dissociation at that location.

This cannot be analytically solved for $T(x)$, but plugging in all constants for rubrene (given in chapter 4) we get an idea of the order of magnitude for each term:

$$(1.6 \times 10^{-7}) \frac{d^2}{dx^2} T(x) = (1 \times 10^{-4}) T(x) + (6.9 \times 10^{-14}) T^2(x) - (1.90) G(x).$$

We've attempted several numerical and analytical methods to use this equation to predict the profiles seen in our experiments, but have trouble solving the equation because of its second-order nonlinear character. This is an area of ongoing research.

Bibliography

[1] Gorman, R. M. Cooking up bigger brains. *Scientific American* **298**, 102–105 (2008).

[2] Bardeen, C. J. The structure and dynamics of molecular excitons. *Annual review of physical chemistry* **65**, 127–148 (2014).

[3] Smith, M. B. & Michl, J. Singlet fission. *Chemical Reviews* **110**, 6891–6936 (2010).

[4] Smith, M. B. & Michl, J. Recent advances in singlet fission. *Annual review of physical chemistry* **64**, 361–386 (2013).

[5] Bardeen, C. Solar & alternative energy using hybrid nanomaterials to increase solar energy conversion efficiencies. SPIE Newsroom.

[6] Hanna, M. & Nozik, A. Solar conversion efficiency of photovoltaic and photoelectrolysis cells with carrier multiplication absorbers. *Journal of Applied Physics* **100**, 074510 (2006).

[7] Shockley, W. & Queisser, H. J. Detailed balance limit of efficiency of p-n junction solar cells. *Journal of applied physics* **32**, 510–519 (1961).

[8] Kittel, C. *Introduction to Solid State Physics* (Wiley, 2004).

[9] Omar, M. *Elementary Solid State Physics.* Addison-Wesley series in solid state sciences (Pearson Education, 1975).

[10] Pope, M. & Swenberg, C. *Electronic Processes in Organic Crystals and Polymers*. Monographs on the physics and chemistry of materials (Oxford University Press, 1999).

[11] Monahan, N. & Zhu, X.-Y. Charge transfer-mediated singlet fission. *Annual review of physical chemistry* **66**, 601â618 (2015).

[12] Piland, G. B., Burdett, J. J., Kurunthu, D. & Bardeen, C. J. Magnetic field effects on singlet fission and fluorescence decay dynamics in amorphous rubrene. *The Journal of Physical Chemistry C* **117**, 1224–1236 (2013).

[13] Scholes, G. D. Correlated pair states formed by singlet fission and exciton–exciton annihilation. *The Journal of Physical Chemistry A* **119**, 12699–12705 (2015).

[14] McGlynn, S. P., Azumi, T., Kinoshita, M. *et al.* Molecular spectroscopy of the triplet state (1969).

[15] Eisberg, R. & Resnick, R. *Quantum physics* (John Wiley & Sons, 1985).

[16] Singh, S., Jones, W., Siebrand, W., Stoicheff, B. & Schneider, W. Laser generation of excitons and fluorescence in anthracene crystals. *The Journal of Chemical Physics* **42**, 330–342 (1965).

[17] Berkelbach, T. C., Hybertsen, M. S. & Reichman, D. R. Microscopic theory of singlet exciton fission. i. general formulation. *The Journal of chemical physics* **138**, 114102 (2013).

[18] Berkelbach, T. C., Hybertsen, M. S. & Reichman, D. R. Microscopic theory of singlet exciton fission. ii. application to pentacene dimers and the role of superexchange. *The Journal of chemical physics* **138**, 114103 (2013).

[19] Berkelbach, T. C., Hybertsen, M. S. & Reichman, D. R. Microscopic theory of singlet exciton fission. iii. crystalline pentacene. *The Journal of chemical physics* **141**, 074705 (2014).

[20] Chan, W.-L., Ligges, M. & Zhu, X. The energy barrier in singlet fission can be overcome through coherent coupling and entropic gain. *Nature chemistry* **4**, 840–845 (2012).

[21] Chan, W.-L., Berkelbach, T. C., Provorse, M. R., Monahan, N. R., Tritsch, J. R., Hybertsen, M. S., Reichman, D. R., Gao, J. & Zhu, X.-Y. The quantum coherent mechanism for singlet fission: Experiment and theory. *Accounts of chemical research* **46**, 1321–1329 (2013).

[22] Miyata, K., Tanaka, S., Sugimoto, T., Watanabe, K., Uemura, T., Takeya, J. & Matsumoto, Y. Coherent phonon dynamics in singlet fission of rubrene single crystal. In *Ultrafast Phenomena XIX*, 218–221 (Springer, 2015).

[23] Chabr, M., Wild, U., Fünfschilling, J. & Zschokke-Gränacher, I. Quantum beats of prompt fluorescence in tetracene crystals. *Chemical Physics* **57**, 425–430 (1981).

[24] Burdett, J. J., Piland, G. B. & Bardeen, C. J. Magnetic field effects and the role of spin states in singlet fission (2013). URL `http://www.sciencedirect.com/science/article/pii/S0009261413010464`.

[25] Braslavsky, S. E. Glossary of terms used in photochemistry, (iupac recommendations 2006). *Pure and Applied Chemistry* **79**, 293–465 (2007).

[26] Tao, S., Ohtani, N., Uchida, R., Miyamoto, T., Matsui, Y., Yada, H., Uemura, H., Matsuzaki, H., Uemura, T., Takeya, J. & Okamoto, H. Relaxation dynamics of photoexcited excitons in rubrene single crystals using femtosecond absorption spectroscopy. *Phys. Rev. Lett.* **109**, 097403 (2012).

[27] Anthony, J. E. Functionalized acenes and heteroacenes for organic electronics. *Chemical reviews* **106**, 5028–5048 (2006).

[28] Bendikov, M., Wudl, F. & Perepichka, D. F. Tetrathiafulvalenes, oligoacenenes, and their buckminsterfullerene derivatives: The brick and mortar of organic electronics. *Chemical reviews* **104**, 4891–4946 (2004).

[29] Pandey, A. K. Highly efficient spin-conversion effect leading to energy upconverted electroluminescence in singlet fission photovoltaics. *Scientific reports* **5** (2015).

[30] Ma, L., Zhang, K., Kloc, C., Sun, H., Soci, C., Michel-Beyerle, M. E. & Gurzadyan, G. G. Fluorescence from rubrene single crystals: Interplay of singlet fission and energy trapping. *Phys. Rev. B* **87**, 201203 (2013).

[31] Biaggio, I. & Irkhin, P. Extremely efficient exciton fission and fusion and its dominant contribution to the photoluminescence yield in rubrene single crystals. *Applied Physics Letters* **103** (2013).

[32] Ern, V., Saint-Clair, J., Schott, M. & Delacote, G. Effects of exciton interactions on the fluorescence yield of crystalline tetracene. *Chemical Physics Letters* **10**, 287 – 290 (1971).

[33] Hasegawa, T. & Takeya, J. Organic field-effect transistors using single crystals. *Science and Technology of Advanced Materials* (2009).

[34] Podzorov, V., Pudalov, V. & Gershenson, M. Field-effect transistors on rubrene single crystals with parylene gate insulator. *Applied physics letters* **82**, 1739–1741 (2003).

[35] Najafov, H., Biaggio, I., Podzorov, V., Calhoun, M. F. & Gershenson, M. E. Primary photoexcitations and the origin of the photocurrent in rubrene single crystals. *Physical review letters* **96**, 056604 (2006).

[36] Najafov, H., Lyu, B., Biaggio, I. & Podzorov, V. Investigating the origin of the high photoconductivity of rubrene single crystals. *Physical Review B* **77**, 125202 (2008).

[37] Irkhin, P. & Biaggio, I. Direct imaging of anisotropic exciton diffusion and triplet diffusion length in rubrene single crystals. *Phys. Rev. Lett.* **107**, 017402 (2011).

[38] Irkhin, P., Ryasnyanskiy, A., Koehler, M. & Biaggio, I. Absorption and photoluminescence spectroscopy of rubrene single crystals. *Phys. Rev. B* **86**, 085143 (2012).

[39] Kaminsky, W. *WinXMorph*: a computer program to draw crystal morphology, growth sectors and cross sections with export files in VRML V2.0 utf8-virtual reality format. *Journal of Applied Crystallography* **38**, 566–567 (2005).

[40] Jurchescu, O. D., Meetsma, A. & Palstra, T. T. Low-temperature structure of rubrene single crystals grown by vapor transport. *Acta Crystallographica Section B: Structural Science* **62**, 330–334 (2006).

[41] Chen, Y., Lee, B., Fu, D. & Podzorov, V. The origin of a 650 nm photoluminescence band in rubrene. *Advanced Materials* **23**, 5370–5375 (2011).

[42] Mitrofanov, O., Lang, D. V., Kloc, C., Wikberg, J. M., Siegrist, T., So, W.-Y., Sergent, M. & Ramirez, A. P. Oxygen-related band gap state in single crystal rubrene. *Physical review letters* **97**, 166601 (2006).

[43] Mitrofanov, O., Kloc, C., Siegrist, T., Lang, D. V., So, W.-Y. & Ramirez, A. P. Role of synthesis for oxygen defect incorporation in crystalline rubrene. *Applied Physics Letters* **91**, 212106 (2007).

[44] Wen, X., Yu, P., Yuan, C.-T., Ma, X. & Tang, J. Singlet and triplet carrier dynamics in rubrene single crystal. *The Journal of Physical Chemistry C* **117**, 17741–17747 (2013).

[45] Biaggo, I. Short-pulse induced photocurrent and photoluminescence in organic materials. *Handbook of Organic Materials for Optical and (Opto) Electronic Devices: Properties and Applications* 356 (2013).

[46] Murov, S., Carmichael, I. & Hug, G. *Handbook of Photochemistry, Second Edition* (Taylor & Francis, 1993).

[47] Ryasnyanskiy, A. & Biaggio, I. Triplet exciton dynamics in rubrene single crystals. *Phys. Rev. B* **84**, 193203 (2011).

[48] Ma, L., Zhang, K., Kloc, C., Sun, H., Michel-Beyerle, M. E. & Gurzadyan, G. G. Singlet fission in rubrene single crystal: direct observation by femtosecond pump-probe spectroscopy. *Phys. Chem. Chem. Phys.* **14**, 8307–8312 (2012).

[49] Furube, A., Katoh, R., Mitsuta, H., Miyadera, T. & Yoshida, Y. Picosecond multiple exciton generation from the excited singlet state in rubrene single crystal. In *Meeting Abstracts*, 38, 1831–1831 (The Electrochemical Society, 2011).

[50] Tao, S., Matsuzaki, H., Uemura, H., Yada, H., Uemura, T., Takeya, J., Hasegawa, T. & Okamoto, H. Optical pump-probe spectroscopy of photocarriers in rubrene single crystals. *Phys. Rev. B* **83**, 075204 (2011).

[51] Irkhin, P., Biaggio, I., Zimmerling, T., Döbeli, M. & Batlogg, B. Defect density dependent photoluminescence yield and triplet diffusion length in rubrene. *Applied Physics Letters* **108**, 063302 (2016).

[52] Aldrich, S. Rubrene powder product specification. Online. URL `http://www.sigmaaldrich.com/Graphics/COfAInfo/SigmaSAPQM/SPEC/R2/R2206/R2206-BULK________ALDRICH__.pdf`.

[53] Organics, A. Rubrene 99 percent. Online. URL `https://www.fishersci.com/shop/products/rubrene-99-acros-organics-2/p-191170#`.

[54] Erie scientific micro cover glasses,. Rectangular, No. 1 24X50-1.

[55] Montana Instruments. *Cryostation Heat Load Map* (2016). URL `http://resources.montanainstruments.com/help/article/link/heat-load`.

[56] Kazzaz, A. & Zahlan, A. Temperature dependence of crystalline tetracene fluorescence. *The Journal of Chemical Physics* **48**, 1242–1245 (1968).

[57] Petrenko, T., Krylova, O., Neese, F. & Sokolowski, M. Optical absorption and emission properties of rubrene: insight from a combined experimental and theoretical study. *New journal of physics* **11**, 015001 (2009).

[58] Ern, V. & Merrifield, R. Magnetic field effect on triplet exciton quenching in organic crystals. *Physical Review Letters* **21**, 609 (1968).

[59] Swenberg, C. & Stacy, W. Bimolecular radiationless transitions in crystalline tetracene. *Chemical Physics Letters* **2**, 327–328 (1968).

[60] Donnmi, J.-M. & Abetino, F. Flourescence of naphthacene. magnetic effect. *Computes Rendus de l'Académie des Sciences series B* **266B**, 1618–1621 (1968).

[61] Rumyantsev, B. M., Lesin, V. I. & Frankevich, E. L. Fluorescence of crystalline rubrene in a magnetic field. *Optics and Spectroscopy* **38**, 49–50 (1975).

[62] Johnson, R., Merrifield, R., Avakian, P. & Flippen, R. Effects of magnetic fields on the mutual annihilation of triplet excitons in molecular crystals. *Physical Review Letters* **19**, 285 (1967).

[63] Johnson, R. & Merrifield, R. Effects of magnetic fields on the mutual annihilation of triplet excitons in anthracene crystals. *Physical Review B* **1**, 896 (1970).

[64] Merrifield, R., Avakian, P. & Groff, R. Fission of singlet excitons into pairs of triplet excitons in tetracene crystals. *Chemical Physics Letters* **3**, 386–388 (1969).

[65] Groff, R., Avakian, P. & Merrifield, R. Coexistence of exciton fission and fusion in tetracene crystals. *Physical Review B* **1**, 815 (1970).

[66] Jortner, J., Choi, S.-i., Katz, J. L. & Rice, S. A. Triplet energy transfer and triplet-triplet interaction in aromatic crystals. *Physical Review Letters* **11**, 323 (1963).

[67] Akselrod, G. M., Deotare, P. B., Thompson, N. J., Lee, J., Tisdale, W. A., Baldo, M. A., Menon, V. M. & Bulović, V. Visualization of exciton transport in ordered and disordered molecular solids. *Nature communications* **5** (2014).

[68] Wan, Y., Guo, Z., Zhu, T., Yan, S., Johnson, J. & Huang, L. Cooperative singlet and triplet exciton transport in tetracene crystals visualized by ultrafast microscopy. *Nature chemistry* **7**, 785–792 (2015).

[69] da Silva Filho, D. A., Kim, E.-G. & Brédas, J.-L. Transport properties in the rubrene crystal: electronic coupling and vibrational reorganization energy. *Advanced Materials* **17**, 1072–1076 (2005).

[70] Wahl, M. *Time-Correlated Single-Photon Counting.* PicoQuant GmbH, Rudower Chausse 29, 12489 Berlin, Germany.

[71] Gieseking, B., Schmeiler, T., Müller, B., Deibel, C., Engels, B., Dyakonov, V. & Pflaum, J. Effects of characteristic length scales on the exciton dynamics in rubrene single crystals. *Physical Review B* **90**, 205305 (2014).

[72] Lyu, B. *Photocurrent, photoluminescence and exciton dynamics in rubrene molecular single crystals.* Ph.D. thesis, Lehigh University (2013).

[73] Boens, N., Qin, W., Basaric, N., Hofkens, J., Ameloot, M., Pouget, J., Lefèvre, J.-P., Valeur, B., Gratton, E., VandeVen, M. *et al.* Fluorescence lifetime standards for time and frequency domain fluorescence spectroscopy. *Analytical chemistry* **79**, 2137–2149 (2007).

[74] Jankus, V., Snedden, E. W., Bright, D. W., Arac, E., Dai, D. & Monkman, A. P. Competition between polaron pair formation and singlet fission observed in amorphous rubrene films. *Physical Review B* **87**, 224202 (2013).

[75] Ma, L., Galstyan, G., Zhang, K., Kloc, C., Sun, H., Soci, C., Michel-Beyerle, M. E. & Gurzadyan, G. G. Two-photon-induced singlet fission in rubrene single crystal. *The Journal of chemical physics* **138**, 184508 (2013).

[76] Ward, K. A., Richman, B. R. & Biaggio, I. Nanosecond pump and probe observation of bimolecular exciton effects in rubrene single crystals. *Applied Physics Letters* **106**, 223302 (2015).

[77] Kazmerski, L. *Polycrystalline and amorphous thin films and devices* (Elsevier, 2012).

[78] McGarry, K. A., Xie, W., Sutton, C., Risko, C., Wu, Y., Young Jr, V. G., Brédas, J.-L., Frisbie, C. D. & Douglas, C. J. Rubrene-based single-crystal organic semiconductors: synthesis, electronic structure, and charge-transport properties. *Chemistry of Materials* **25**, 2254–2263 (2013).

[79] Lakowicz, J. R. *Principles of fluorescence spectroscopy* (Springer Science & Business Media, 2013).

[80] Park, S.-W., Choi, J.-M., Lee, K. H., Yeom, H. W., Im, S. & Lee, Y. K. Amorphous-to-crystalline phase transformation of thin film rubrene. *The Journal of Physical Chemistry B* **114**, 5661–5665 (2010).

[81] Paez, B., Abd-Al-Baqi, S., Sosa, G., Andreev, A., Winder, C., Padinger, F., Simbrunner, C. & Sitter, H. Crystalline stages of rubrene films probed by raman spectroscopy. In *Interface Controlled Organic Thin Films*, 37–41 (Springer, 2009).

[82] Nothaft, M. & Pflaum, J. Thermally and seed-layer induced crystallization in rubrene thin films. *physica status solidi (b)* **245**, 788–792 (2008).

[83] Siyu Yang, A. K., Barry Rand. Factors influencing the crystallization of rubrene thin films (2016).

[84] Carraher, C. *Seymour/Carraher's Polymer Chemistry*. Undergraduate chemistry (CRC Press, 2003), 6 edn.

[85] Mastrogiovanni, D. D., Mayer, J., Wan, A. S., Vishnyakov, A., Neimark, A. V., Podzorov, V., Feldman, L. C. & Garfunkel, E. Oxygen incorporation in rubrene single crystals. *Scientific reports* **4** (2014).

Thank you to those who have helped me,
and those who trusted me to help them.

Dr. Ivan Biaggio

and his group of researchers (pirates):
Kebra, Drew, Michael, Jing, Ian, and Marten; REUs Liz, Hannah, and Michael.

My awesome friends: Natalie, Laura, Phil, Gaby

The Physics Department of Lehigh University
Dr. Stavola, Dr. Huennekens, Dr. Rotkin, Dr. Dierolf,
as well as Dr. Strandwitz from the Materials Science Department.

Adam, Vural, Kara, O.N.e, Keith, Andrew, Massooma, Josh and Holly, Ben.

The undergraduate students who made teaching fun and rewarding.

Carolina

My family

Lehigh University Graduate Life Office and Graduate Student Senate.

The Lehigh Valley swing dancing community.

Excitonic Processes, Energy Transport, and Excited States in Organic Materials

PhD thesis defense of V. Zoutenbier

- Do you like lasers?
- Do you want to learn about how we use lasers to investigate material processes?

If you said yes to either of these questions, then this is a thesis defense you won't want to miss!

In this thesis, we use lasers as an excitation mechanism to investigate the creation of singlet and triplet excitons in organic molecular crystals, how one species can convert into the others by excitonic fission and fusion, and how triplet excitons can travel comparatively long distances.

I show this in the context of how we measure photoluminescence from rubrene crystals using both continuous-wave lasers, for spectral and spatial measurements, and pulsed lasers, for time-dynamics measurements.

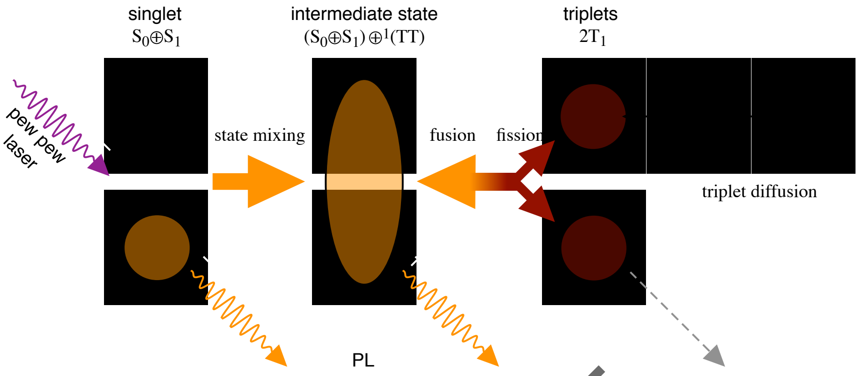

Monday, 18 July 2016
2:10 pm
Lewis Lab 316

Vita

Vincent Sean Zoutenbier completed an Associate degree in general studies at Valencia College before obtaining a Bachelor's degree in physics from the University of Florida in 2011. He then began his graduate studies at Lehigh University, where he was awarded a Master's degree in physics in January 2013, and his PhD in physics in August 2016.